UNIVERSITÀ DEGLI STUDI DI TRIESTE

XXVII CICLO DEL DOTTORATO DI RICERCA IN NANOTECNOLOGIE

NANOSTRUCTURED ELECTROCATALYSTS FOR ANION EXCHANGE MEMBRANE FUEL CELLS

Settore scientifico-disciplinare: CHIM/03

DOTTORANDO
LIANQIN WANG

COORDINATORE
PROF. LUCIA PASQUATO

SUPERVISORE DI TESI
PROF. PAOLO FORNASIERO

TUTORI DI TESI
DR. ALESSANDRO LAVACCHI

DR. FRANCESCO VIZZA

ANNO ACCADEMICO 2013 / 2014

Abstract

Amongst current societal challenges sustainability is certainly a priority. The possibility of building a sustainable future, while maintaining high standards in the quality of life and preserving environment and resources, strongly relies on the availability of methods for the green production of energy and chemicals. The production of chemicals together with the on-demand power generation can be achieved in Direct Liquid Fuel Cells (DLFCs), devices in which the chemical energy of a liquid fuel is converted into electrical energy. DLFCs usually employ Small Organic Molecules (SOMs), such as alcohols or formic acid, as fuels. These fuels can be obtained from biomass feedstock. Consequently their use generates a significantly lower atmospheric CO_2 with respect to the use of fossil fuels, resulting in a potential mitigation of the "greenhouse effect".

At the present stage, DLFCs rely on the use of the rare and costly platinum. This is for two reasons: i) platinum is a good catalyst for both SOMs oxidation and Oxygen Reduction Reaction (ORR); ii) platinum is stable in acidic environment. It is worth mentioning that most of DLFCs employ proton exchange membranes as electrolytes and need strongly acidic conditions for achieving low resistivity. In these systems also the water management can be a problem, as it is attracted to the cathode side for polarization and water is frequently introduced in the feed stream to the fuel cell. At present acidic DLFCs operate with a platinum content largely exceeding 1 mg cm^{-2}, a fact that severely hampers the diffusion of such devices.

In this investigation, thanks to a low resistivity Anion Exchange Membranes (AEM), the Tokuyama A-201, we have developed efficient alkaline direct liquid fuel cells (AEM-DLFCs). This has been done with the purpose of eliminating platinum from the devices. Indeed it is known that palladium effectively catalyzes SOMs oxidation in alkali; besides, oxygen reduction reaction can also be effectively achieved by using iron and cobalt phtalocyanines (Pc). Consequently the membrane electrode assembly (MEA) of a AEM-DLFC can be assembled using: i) a palladium based anode, ii) a Tokuyama A-201 membrane and iii) a cathode containing FePc-CoPc/C as electrocatalyst obtained from the high temperature pyrolysis of FePc-CoPc. An important fact is that FePc-CoPc/C is not active at all for the

oxidation of SOMs. This has the major implication that fuel crossover through the membrane does not result in significant potential (and so energy efficiency) drop in fuel cells.

The experimental part of this thesis starts with a chapter devoted to the analysis of the energy performance of *platinum-free* AEM-DLFCs fueled with ethanol (Chapter 3). This work is the first exhaustive analysis of the energy performance of such devices. Particularly we have determined the major parameters that characterize the fuel cell operations: i) maximum power density, ii) energy efficiency and iii) energy delivered per single fuel batch. All these parameters have been determined as a function of the fuel composition. We have discovered that the fuel concentration that maximizes one of the parameters can be detrimental to the others with the fundamental consequence that fuel composition must be selected according to the selected application. The effect of adding a promoting oxide, CeO_2, to the anode catalyst has also been investigated. In some cases efficiency can be improved up to the 100% by simply adding cerium oxide to the anode catalyst. We have also proved that DEFCs are suitable candidates for the µ-fuel cells technology as we have shown their ability to operate with no or little performance degradation for 3 months at low power density (< 1 mW cm^{-2}).

Chapter 4 is dedicated to the Direct Formate Fuel Cells (DFFCs). Nanostructured Pd/C and FePc-CoPc/C have been employed at the anode and cathode side respectively. A large open circuit voltage ($\geq$1.0 V) was obtained. This has been attributed to the larger (as compared with DEFCs) Nernst potential of the DFFCs and the use of FePc-CoPc/C as cathode electrocatalyst to restrain the reduction of cell voltage by fuel crossover. Our DFFCs have shown maximum power density larger than state of the art AEM-DLFCs and also Direct Formic Acid Fuel Cells (DFAFCs). AEM-DFFCs are also very effective in exploiting the energy content of the fuel. Indeed we have shown that DFFCs energy efficiency is four times the energy efficiency of analogous DEFCs. This point is very important to exploit the technology as the energy efficiency is the key issue for achieving sustainability and the major constraints for systems devoted to massive energy production. Again we have found that fuel composition is essential for the performance. The best power density was obtained by the cell fuelled with 2 M formate plus 2 M KOH, while best delivered energy, fuel utilization and energy efficiency were delivered by cell equipped with 4 M formate plus 4 M KOH.

To enhance the ability of palladium to catalyze SOMs oxidation in alkaline environment, we have developed an original electrochemical treatment (Chapter 5). The treatment consisted

of the application of a Square-Wave Potential (SWP) to the electrode and resulted in surface roughening and change in the distribution of the crystal surface terminations. Particularly we have found that after SWP an increase of the density of low coordination (Coordination Number < 8) Pd surface atoms occurs. We have found significant activity enhancement (from 4 to 5.6 times as compared to untreated surface) for the oxidation of all the investigated alcohols. Furthermore, FTIR spectra have shown that the reaction products distribution was also affected. Particularly we determined an increased tendency of the SWP treated Pd surface to cleave the C-C bond as compared to the untreated ones.

A tailored SWP treatment for enhancing the catalytic activity of platinum was also developed (Chapter 6). The essential reason behind the study is to provide a tool for reducing Pt content in fuel cells when it cannot be completely eliminated. For platinum, it has turned out that the period of the square wave is the most important parameter. The most active platinum surface for Ethanol Oxidation Reaction (EOR) in alkali has been produced with a square wave period of 120 min, while the maximum stability of the catalytic performance has been obtained with the sample produced with a period of 360 min. Via in situ FTIR we have also found that the treated samples limit C-C cleavage as compared to the untreated ones. This suggests that SWP on Pt could provide an effective strategy to minimize the formation of CO, a major poisoning agent for platinum based catalysts.

Chapter 7 is devoted to the investigation of the degradation mechanism of palladium electrocatalysts in platinum-free AEM-DLFCs. This is among the main issues still preventing the full exploitation of palladium in DLFCs. We have demonstrated that palladium oxide formation is the major cause for the catalytic performance degradation. We came to this conclusion by combining the information derived from electrochemical measurements and synchrotron light experiments (X-ray Absorption Spectroscopy). X-ray Absorption Near Edge Structure (XANES) spectra of the Pd Kα edge before and after DEFC run have shown that Pd is present in its metallic form in the pristine catalyst, while it is almost completely oxidized after work in an ethanol fed fuel cell. This has enabled us to conclude that to extend the service life of palladium electro-catalysts in alkali, the anode potential has not to exceed 0.7 V. In practice this can be achieved with a simple electronic control of the device.

Increasing the operating temperature of fuel cells is an alternative strategy to improve the performance of fuel cells fed with SOMs containing fuels. In chapter 8, palladium has been investigated as a catalyst for ethanol oxidation at intermediate temperatures (> 100 °C) in a

pressurized vessel. We have found that the increase of the temperature dramatically enhances the ability of catalyzing EOR in alkali. This fact has been ascribed to the improved adsorption of the hydroxyl species on the palladium surface. The same enhancement has not been observed in acidic environment. A few experiments on the use of tungsten carbide in a cobalt matrix (WC-Co) have also been performed. We have proved that WC-Co does not catalyze significantly the ethanol oxidation reaction in alkaline media, while it does in acidic electrolyte at medium temperature (~50 °C). At larger temperature the stability in acidic environment is not enough to allow a reliable assessment of the catalytic performance. Larger stability has been achieved in alkali where tungsten carbide is a potential candidate for supporting other active phases such as noble metals.

Scopo del lavoro

Lo sviluppo sostenibile è una sfida prioritaria per la nostra società. La possibilità di costruire un futuro sostenibile, mantenendo al contempo alti standard nella qualità della vita e preservando risorse e ambiente, dipende dalla disponibilità di metodi per la produzione *verde* di energía e prodotti chimici. La produzione simultanea di prodotti chimici ed energía può essere ottenuta nelle celle a combustibile che impiegano combustibili liquidi (Direct Liquid Fuel Cells – DLFC), dispositivi in cui l'energia chimica contenuta nelle molecole di combustibile è convertita direttamente in energía elettrica. Le DLFC impiegano solitamente combustibili a base di piccole molecole organiche quali ad esempio alcoli ed acido formico. Questi combustibili sono di particolare interesse, dal momento che possono essere ottenuti a partire da biomassa, con un impatto minore sulle emissioni di gas serra rispetto ai combustibili fossili.

Allo stato attuale le DLFC impiegano platino in quantità elevate. Questo per due ragioni: i) il platino è un buon catalizzatore sia per l'ossidazione di composti organici che per la riduzione dell'ossigeno e ii) il platino è stabile in ambiente acido. E' importante sottolineare che le attuali DLFC impiegano membrane a scambio protonico come elettroliti e dunque richiedono ambienti fortemente acidi per avere un'adeguata conducibilità. Le DLFC impiegano carichi di platino maggiori di 1 mg cm^{-2}, un fatto che ne limita molto la possibilità di diffusione commerciale.

In questo lavoro, grazie alla disponibilità di membrane a scambio anionico ad elevata conducibilità (Tokuyama A-201), abbiamo sviluppato delle DLFC alcaline (Anion Exchange Membrane Direct Liquid Fuel Cells – AEM-DLFC). Ciò e' stato fatto con l'obiettivo di eliminare il platino dai dispositivi. E' infatti noto che il palladio è un catalizzatore molto attivo per l'ossidazione delle piccole molecole organiche in ambiente alcalino e che la reazione di riduzione dell'ossigeno puo' essere catalizzata da composti di ferro e cobalto (es. ftalocianine). La tecnología qui riportatata si basa sull'impiego di anodi di palladio supportati da *carbon black* (Vulcan XC-72), membrane a scambio anionico e ftalocianine di ferro e cobalto subbortate da *carbon black* con maggiore area superficiale rispetto a quello impiegato all'anodo (Ketjen Black 600). Un fatto importante è che le ftalocianine di ferro e cobalto non sono attive per l'ossidazione di molecole organiche. Ciò è particolarmente rilevante per le *fuel*

cells perché il *cross-over* del combustibile attraverso la membrana non produce significative cadute di potenziale e quindi dell'efficienza energetica.

La parte sperimentale della tesi inizia con un capitolo in cui si decrivono le prestazioni di AEM-DLFC esenti da platino ed alimentate ad etanolo. Questa parte del lavoro è particolarmente rilevante dal momento che è la prima e completa caratterizzazione della *performance* energetica di questi dispositivi. In particolare si sono determinati i seguenti parametri: i) massima densità di potenza, ii) efficienza energetica e iii) l'energia prodotta per singolo batch di combustibile. Tutti questi parametri sono stati determinati in funzione della composizione del combustibile. Abbiamo scoperto che la composizione del combustibile che massimizza uno dei parametri sopra riportati generalmente ha effetti negativi sugli altri. E' dunque necesario definire la composizione del combustibile in funzione della particolare applicazione cui il dispositivo è destinato. Abbiamo inoltre studiato l'effetto dell'aggiunta di un ossido promotore, la ceria, al catalizatore anódico, mostrando che le prestazioni migliorano significativamente. In alcuni casi l'efficienza energetica può essere migliorata anche di più del 100% grazie alla semplice aggiunta di dell'ossido promotore.

Il capitolo successivo e' dedicato alle celle a combustile che impiegano combustibili a base di formiato (Direct Formate Fuel Cells – DFFC). In questo caso si sono impiegati catalizzatori nanostrutturati di Pd supportato da Vulcan XC-72 e ftalocianine di ferro e cobalto, rispettivamente all'anodo ed al catodo, ottenendo un potenziale di circuito aperto superiore ad 1 V. Le celle alcaline al formiato hanno prodotto una densità massima di potenza superiore alle celle alcaline che impiegano metanolo ed etanolo, ed anche alle celle acide che impiegano acido formico. In particolare l'efficienza energetica delle celle al formiato è stata superiore di un fattore 4 a quella delle migliori celle alcaline ad etanolo. Questo e' un punto cruciale per l'applicazione pratica della tecnología proposta. Infatti l'efficienza energetica e' uno dei cardini per il raggiungimento della sostenibilità e, senza dubbio, il vincolo principale per i sistemi che devono produrre grandi quantita' di energía, come la generazione stazionaria di energía elettrica. Anche nel caso delle celle al formiato, abbiamo osservato che la composizione del combustibile è essenziale nel definire la *performance* energetica. Abbiamo mostrato che la massima densità di potenza si ottiene con un combustibile che contiene formiato 2 M e KOH 2 M, mentre l'energia per singolo *batch* di combustibile, la migliore conversione del combustibile e l'efficienza energetica sono migliori per il formiato 4 M e KOH 4 M.

Al fine di migliorare la capacità del palladio di catalizzare l'ossidazione elettrochimica di composti organici rinnovabili, abbiamo sviluppato un metodo elettrochimico originale per il trattamento delle superfici degli elettrodi. Il trattamento consiste nell'applicazione di un potenziale ad onda quadra (Square Wave Potential – SWP) che produce un aumento della rugosità superficiale e una modifica della distribuzione delle terminazioni cristalline della superficie, incrementando la densità degli atomi di Pd superficiali a basso numero di coordinazione (< 8). Il trattamento si è rivelato efficace nel migliorare la cinetica di ossidaizione dell'etanolo, dell'etilen glicole e del glicerolo. I trattementi sviluppati hanno prodotto incrementi dell'attività fino ad un fattore 5.6. L'analisi FTIR dei processi di ossidazione ha dimostrato che anche la distribuzione dei prodotti di ossidazione e' affetta dal trattamento. In particolate abbiamo riscontrato un incremento nella capacità dei catalizzatori ottenuti per SWP di rompere il legame C-C.

Il trattamento elettrochimico con potenziale ad onda quadra è stato sviluppato anche per le superfici di platino, con l'obbiettivo di fornire uno strumento per ridurne il contenuto nelle fuel cells quando non sia possibile eliminarlo completamente. Nel caso del platino si è riscontrato che il parámetro piu' importante per l'efficienza del trattamento è il periodo dell'onda quadra. Le superfici più attive si sono ottenute con un periodo di trattamento di 120 minuti, mentre la stabilità massima si e' avuta per campioni trattati con onde quadre con periodo di 360 minuti. Tramite esperimenti FTIR si è inoltre concluso che nel caso del platino il trattamento inibisce la rottura del legame C-C. Questo fatto è importante perchè limita la formazione di frammenti CO che sono le principali specie che avvelenano gli elettrocatalizzatori a base di platino.

Il capitolo 7 è dedicato allo studio dei meccanismi di deattivazione dei catalizzatori di palladio per l'ossidazione elettrochimica in ambiente alcalino di alcoli. L'argomento è rilevante poichè la deattivazione è una delle principali cause che limita la diffusione di questi dispositivi. Abbiamo dimostrato che la formazione di ossidi è la causa che determina maggiormente la degradazione della *performance* catalítica. Siamo giunti a questa conclusione combinando le informazioni proveniente da indagini elettrochimiche ed esperimenti che impiegano la radiazione di sincrotrone. L'analisi degli spettri XANES (Near Edge X-ray Absorption Spectroscopy) ha mostrato che il palladio è presente nella sua forma metallica nei catalizzatori freschi, mentre è completamente ossidato dopo l'impiego in fuel cells. Nello studio si conclude che per allungare la vita degli anodi a base di palladio è

necesario che il catalizzatore anodico non sia esposto a potenziali superiori a 0.7 V. Ciò è possibile in pratica con una semplice elettronica di controllo da abbinare alla cella.

Al fine di aumentare la cinetica di ossidazione abbiamo provveduto ad effettuare esperimenti di ossidazione dell'etanolo a temperature intermedie (> 100 °C) in autoclave. Abbiamo osservato che l'incremento della temperatura aumenta in misura significativa la capacità dei catalizzatori di ossidare l'etanolo in ambiente alcalino. Questo fatto è stato ascritto prevalentemente al miglioramento della capacità di adsorbire specie idrossido alla superficie del palladio. Lo stesso miglioramento non è stato osservato per esperimenti condotti in ambiente acido. Si sono inoltre realizzati esperimenti di ossidazione dell'etanolo su superfici di carburo di tungsteno in matrice di cobalto. Si è provato che questo materiale non mostra un'attività significativa per l'ossidazione di etanolo in ambiente alcalino. In ogni caso si è osservato che il materiale è stabile in ambienti alcalini, in un range di temperatura compreso tra 100 e 200 °C. Questo fatto unitamente all'elevata conducibilità suggerisce che il carburo di tungsteno in matrice di cobalto possa essere impiegato come supporto per la fase attiva dei catalizzatori, quali appunto il palladio. Lo stesso materiale ha mostrato una debole attività nell'ossidazione dell'etanolo ad una temperatura di 50 °C in ambiente acido. La stabilità non era però suficiente per permettere la caratterizzatione delle proprietà catalitiche in soluzioni acide a temperature superiori.

Parole chiave: Nanomateriali; Elettrocatalisi; Celle a combustibile; Alimentatore portatile; Membrana a scambio anionico

Abbreviations

AEM	Anion Exchange Membrane
AFC	Alkaline Fuel Cell
CE	Counter Electrode
CL	Catalyst Layer
CV	Cyclic Voltammetry
DAFC	Direct Alcohol Fuel Cell
DEFC	Direct Ethanol Fuel Cell
DL	Diffusion Layer
DLFC	Direct Liquid Fuel Cell
DMFC	Direct Methanol Fuel cell
EASA	Electrochemically Active Surface Area
ECMF	Electro-Chemical Milling and Faceting
EOR	Ethanol Oxidation Reaction
EROEI	Energy Returned On Energy Invested
EXAFS	Extended X-ray Absorption Fine Structure
FEXRAV	Fixed Energy X-ray Absorption Voltammetry
FMSEM	Field Emission Scanning Electron Microscopy
FTIR	Fourier Transform Infrared
HOH	Hexoctahedra
HRTEM	High Resolution Transmission Electron Microscopy

ICP-AES	Inductively Coupled Plasma Atomic Emission Spectroscopy
LCA	Life Cycle Analysis
MCFC	Molten Carbonate Fuel Cell
MEA	Membrane Electrode Assembly
NMR	Nuclear Magnetic Resonance
OCV	Open Circuit Voltage
ORR	Oxygen Reduction Reaction
PAFC	Phosphoric Acid Fuel Cell
Pc	Phthalocyanines
PEM	Proton Exchange Membrane
PEMFC	Proton Exchange Membrane Fuel Cell
PGSTAT	Potentiostat/Galvanostat
RE	Reference Electrode
RHE	Reversible Hydrogen Electrode
SEM	Scanning Electron Microscopy
SOFC	Solid Oxide Fuel Cell
SOM	Small Organic Molecule
SWP	Square Wave Potential
TEM	Transmission Electron Microscopy
THH	Tetrahexahedra
TOH	Trisoctahedra
TPH	Trapezohedra
UPD	Under Potential Deposition

WE	Working Electrode
XANES	X-ray Absorption Near-Edge Structure
XAS	X-ray Absorption Spectroscopy
XRD	X-Ray Diffraction

Symbols

α	Transfer coefficient
α_a	Transfer coefficient for anodic reaction
α_c	Transfer coefficient for cathodic reaction
C	Concentration
d	Distance
E	Energy
E^0_{eq}	Standard electromotive force
F	Faraday constant
G	Gibbs free energy
H	Enthalpy
I	Current
j	Current density
j_0	Exchange current density
M	Molarity
N	Number of cells in a fuel cell or number of electrons in a reaction
R	Reflectance
V	Voltage or volume
Δ	Difference in…
ΔH^0	The enthalpy change of chemical reaction
ΔU_0	The equilibrium potential in the absence of a current flow

$\Delta U_{0,a}$	The equilibrium electrode potential of anode
$\Delta U_{0,c}$	The equilibrium electrode potential of cathode
η	Over-potential or efficiency
η_E	Energy efficiency
η_F	Faradic efficiency
λ	Wavelength
θ	Angle

Contents

1. Introduction

1.1 Current situation of energy resources

Fossil fuels, which take up more than 80% of the world energy resources (Figure 1-1 [1]), are formed by natural processes such as anaerobic decomposition of buried dead organisms. The transformation of organisms to their resulting fossil fuels takes millions of years, which makes fossil fuels as non-renewable resources since their viable reserves are being depleted much faster than new ones made. As shown in Figure 1-2, the production of utilizable fossil fuels will peak around 2025 and then begin to decrease [2]. As calculated by E. Topal [3], oil, coal and gas will be run out around 35, 107 and 37 years, respectively.
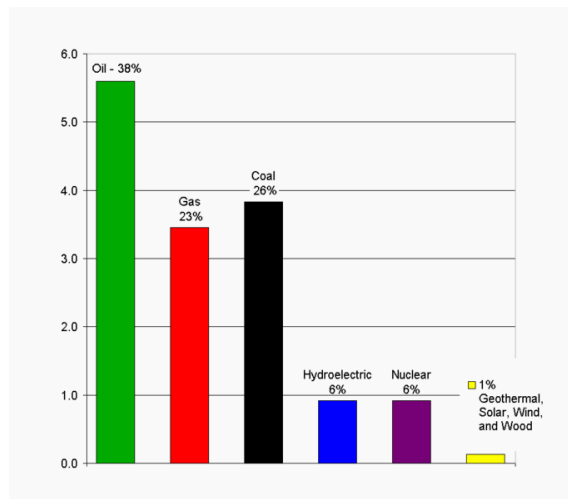
Figure 1-1. Worldwide energy resources.
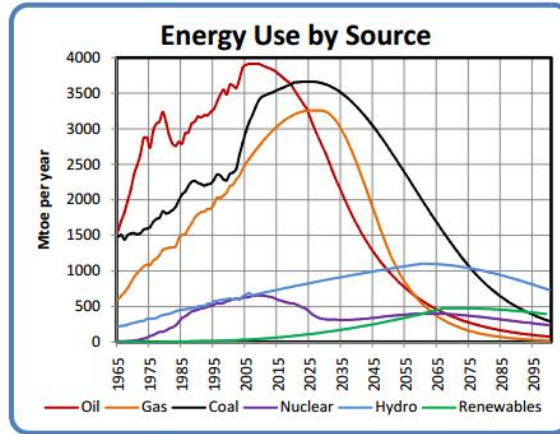
Figure 1-2. Fuel production data and projection, 1965 to 2100.

Fossil fuels are usually extracted from minerals. The extraction-rate was high early in the history. However the Energy Returned On Energy Invested (EROEI) of fossil fuels decreases and eventually goes to zero as the constantly consumption of relatively easily extractable minerals.

Besides the issue of depletion and the decrease of EROEI, the use of fossil fuels raises serious environmental concerns. The burning of fossil fuels produces around 21.3 billion tons of carbon dioxide per year. Carbon dioxide, one of the main greenhouse gases, boosts radiative forcing and contributes to global warming.

Seeking for a sustainable development is a priority. Developing renewable energy sources, such as wind, solar and biomass, meets the need to some extent. On the other hand, it might be wise to find a way to improve the efficiency of end-use equipment. At this point, combination energy sources with the fuel cell conversion system may be a beneficial option for future power generation. The main advantage of fuel cells in this respect are their higher efficiency compared to the internal combustion engines. Beyond all that ethanol converted from biomass can be directly used in direct ethanol fuel cells to generate electricity. Furthermore, fuel cell as green energy equipment emits zero contaminant as operating on pure hydrogen. Some stationary fuel cells use natural gas or hydrocarbons as a hydrogen feedstock. But even these systems produce far fewer emissions than conventional power plants.

1.2 Fuel cells
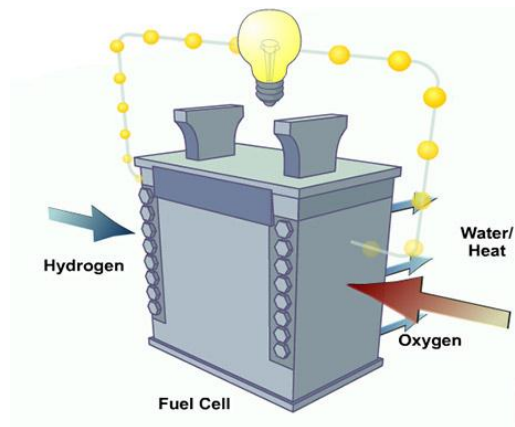
Figure 1-3. Schematic diagram of a fuel cell.

A fuel cell is a device that converts chemical energy directly into electricity through a chemical reaction (Figure 1-3). Typical reactants of fuel cells are hydrogen and oxygen; however, neither has to be in its pure form, except in rare cases. Hydrogen may be presented in a mixture with other gases. For greater efficiency, hydrocarbons, such as natural gas and alcohols, can be used directly. Ambient air containing enough oxygen may be used in the other side of fuel cells.

1.2.1 History

The first crude fuel cell, made by William Grove, is as far back to 1838. However, the technological development of fuel cells fell behind the more well-known steam engines and internal combustion engines. The real progress and development of fuel cells started after one century.

In 1939, Francis Thomas Bacon successfully developed a 5 kW stationary fuel cell. In 1955, W. Thomas Grubb, a chemist working for the General Electric Company (GE), further modified the original fuel cell design by using a sulphonated polystyrene ion-exchange membrane as the electrolyte. Three years later another GE chemist, Leonard Niedrach, devised a way of depositing platinum onto the membrane, which served as catalyst for the necessary hydrogen oxidation and oxygen reduction reactions. GE went on to develop this technology with NASA and McDonnell Aircraft, leading to its use in Project Gemini. This was the first commercial use of a fuel cell.

The successful use of alkaline fuel cell in space program was also the start of a new era for fuel cells. Many research groups started to focus on fuel cells development. Meanwhile, their applications extension from space system to portable power and vehicle began soon afterwards.

1.2.2 Thermodynamics

Fuel cells are galvanic cells, in which the free energy of a chemical reaction is converted into electrical energy. The Gibbs free energy change of a chemical reaction is related to the cell voltage:

$$\Delta G = -nF\Delta U_0 \tag{1-1}$$

Where

n is the number of electrons involved in the reaction;

F is the Faraday constant;

ΔU_0 is the cell voltage for thermodynamic equilibrium in the absence of a current flow.

The anode reaction in fuel cells is either the direct oxidation of hydrogen or the oxidation of alcohol. The cathode reaction in fuel cells is oxygen reduction.

While using H_2/O_2 as the fuel, the overall reaction is:

$$H_2 + \frac{1}{2}O_2 \rightarrow 2H_2O \quad with \; \Delta G = -237 \; kJ/mol \tag{1-2}$$
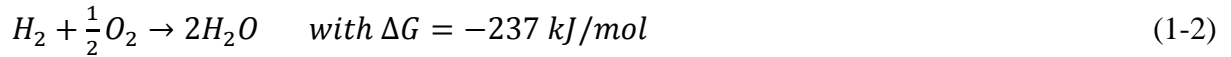
The thermodynamic equilibrium cell voltage ΔU_0 for standard conditions at 25 °C is as following:

$$\Delta U_0 = \frac{-\Delta G}{nF} = 1.23V \tag{1-3}$$

The equilibrium cell voltage is the difference of the equilibrium electrode potentials of cathode and anode which are determined by the electrochemical reaction taking place at the respective electrode:

$$\Delta U_0 = \Delta U_{0,c} - \Delta U_{0,a} \tag{1-4}$$

1.2.3 Reaction kinetics

Electrochemical reactions involve both a change in Gibbs energy and a transfer of electrical charge. The speed of an electrochemical reaction proceeding on the electrode surface is the

rate of the electrons released or consumed, which is the electrical current. Current density is the current per unit area of the surface.

For a redox reaction, the current density (j) is given by the Butler-Volmer equation:

$$j = j_0 \left\{ exp \left[\frac{\alpha_a nF\eta}{RT} \right] - exp \left[-\frac{\alpha_c nF\eta}{RT} \right] \right\} \qquad (1\text{-}5)$$

j_0 is the exchange current density at equilibrium where the net current is equal to zero. Exchange current density is a measure of an electrode's readiness to proceed with electrochemical reaction. If the exchange current density is high, the surface of the electrode is more active.

H is the overpotential, which is the deviation of actual potential from the equilibrium value.

$$\eta = U - U_0 \qquad (1\text{-}6)$$

1.2.4 Voltage losses

When a fuel cell is supplied with reactant but the electrical circuit is open, the cell potential is expected to be at the theoretical value. In fact, this potential, named as open circuit potential, is significantly lower than the theoretical potential. When the electrical circuit is closed, the potential will drop even further due to unavoidable losses. Theses voltage losses are mainly caused by the following factors:

First, activation polarization. Some voltage difference from equilibrium is needed to get the electrochemical reaction going. This is called activation polarization, and it is associated with sluggish electrode kinetics. The higher the exchange current density, the lower the activation polarization losses.

Second, crossover losses. Although the electrolyte is not electrically conductive and is practically impermeable to reactant, some small amount of hydrogen will diffuse from anode to cathode, and some electrons may also find a shortcut through the membranes. Each diffused hydrogen molecule, which reacts with oxygen on the cathode side, results in two fewer electrons in the generated current of electrons that travels through an external circuit.

Third, ohmic losses. Ohmic losses are caused from the resistance of the ions flow in the electrolyte and resistance of the electrons flow through the electrically conductive fuel cell components.

Fourth, concentration polarization. Concentration polarization occurs when a reactant is rapidly consumed at the electrode by the electrochemical reaction so that concentration gradients are established.

Figure 1-4 shows the proportions between three types of losses in the fuel cell. Activation loss is the largest loss at any current density. Figure 1-5 shows how the cell polarization curve is formed, by subtracting the activation polarization losses, ohmic losses, and concentration polarization losses from the equilibrium potential.
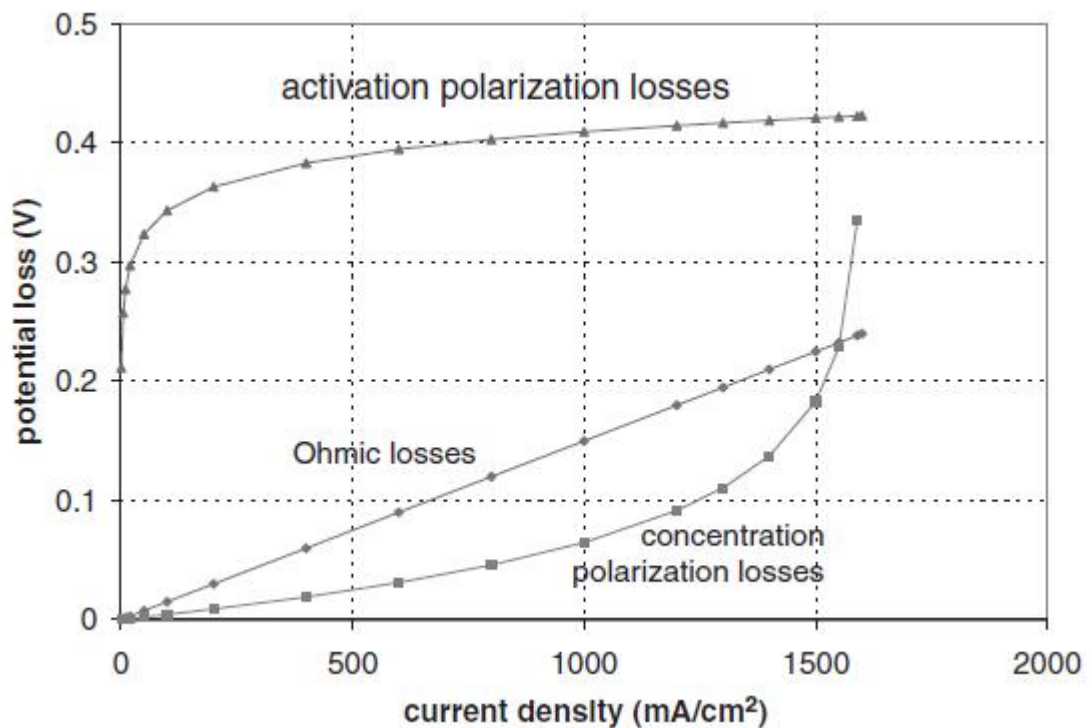
Figure 1-4. Voltage losses in a fuel cell [4].
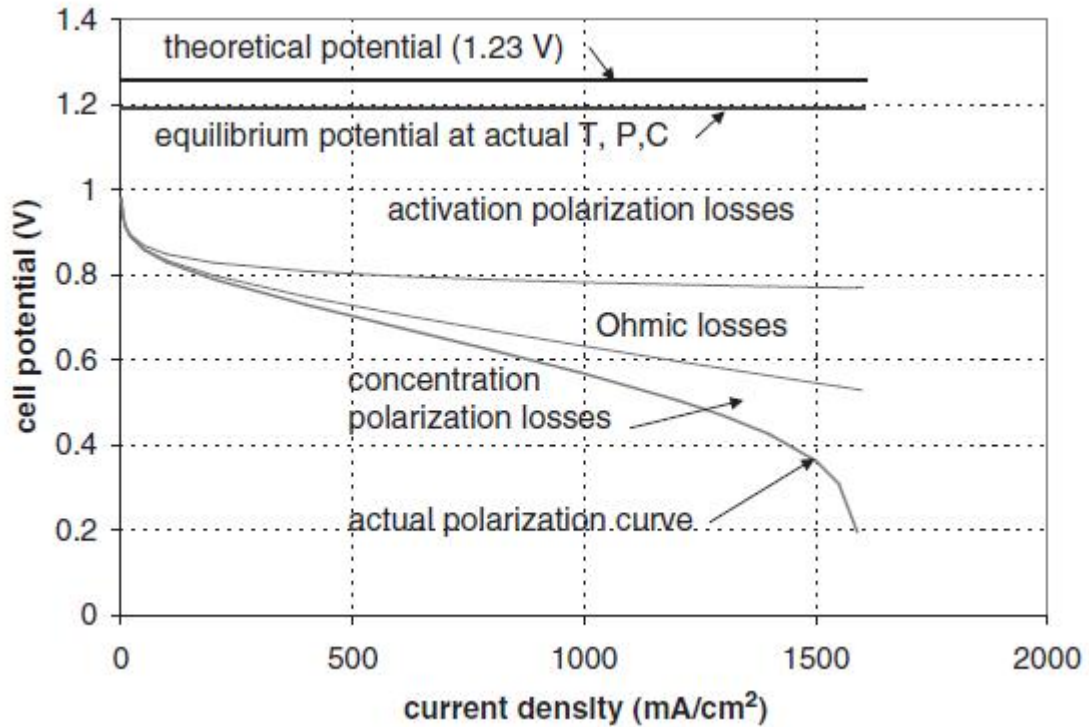
Figure 1-5. Polarization curve as the function of voltage losses [4].

1.2.5 Types of fuel cells

Fuel cells come in many varieties. One way is by the operating temperature, low and high temperature fuel cells. Low temperature fuel cells are the Direct Alcohol Fuel Cell (DAFC), the Proton Exchange Membrane Fuel Cell (PEMFC), the Alkaline Fuel Cell (AFC), and the Phosphoric Acid Fuel Cell (PAFC). The high temperature fuel cells are classed into two types, the Molten Carbonate Fuel Cell (MCFC) and the Solid Oxide Fuel Cell (SOFC). An overview of the fuel cell types is given in Figure 1-6.
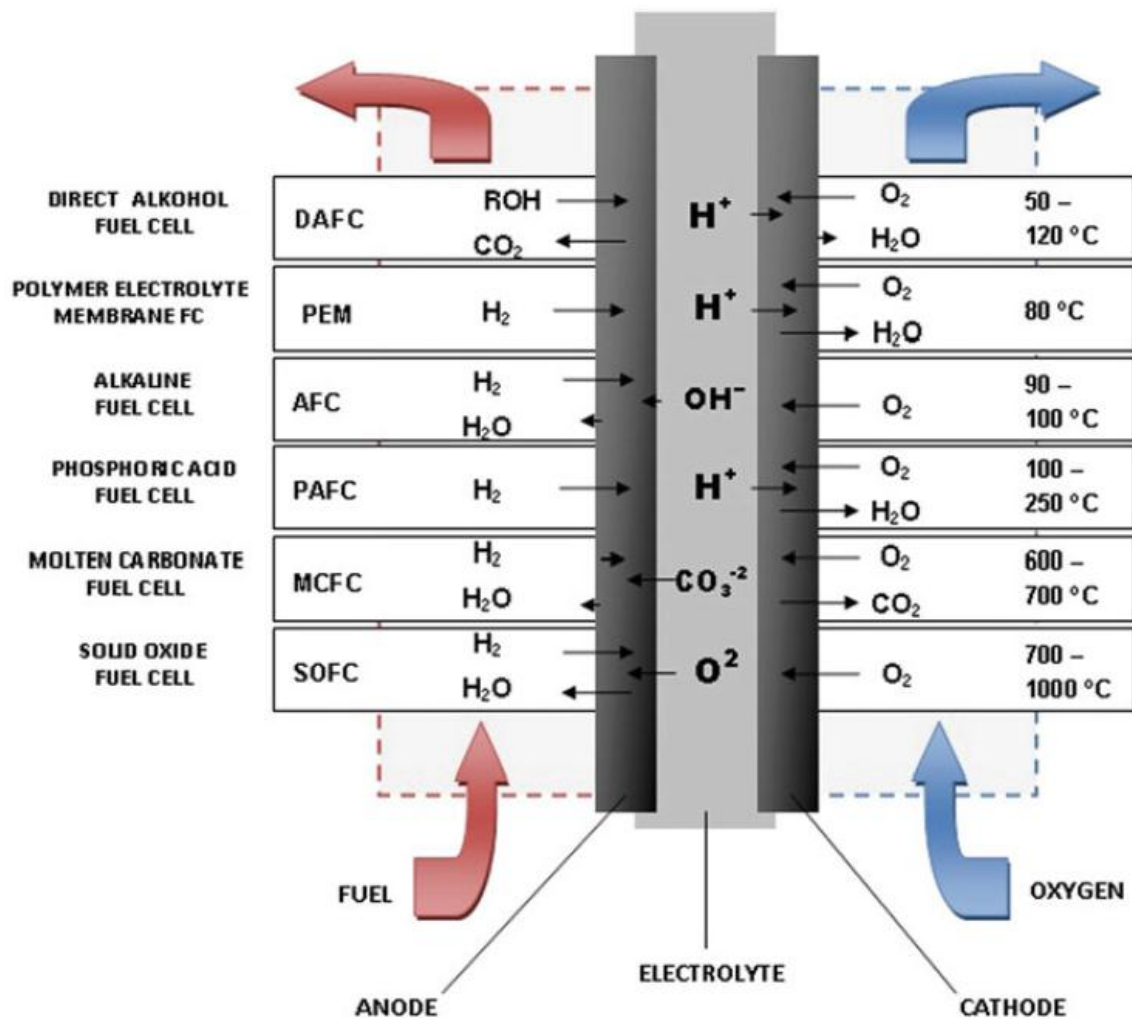
Figure 1-6. Types of Fuel Cells [5]. Anode and cathode reaction, charge carrier in the electrolyte, operating temperature are presented.

A number of these fuel cell types are commercially available today. Each fuel cell type has its own unique chemistry, such as different operating temperatures, catalysts, and electrolytes.

1.2.5.1 Direct Liquid Fuel Cell

The Direct Liquid Fuel Cell (DLFC) is a special form of low-temperature fuel cells based on PEM technology. In the DLFC, small organic molecules are directly fed into the fuel cell without the intermediate step of reforming the alcohol into hydrogen. The low operating temperature makes DMFCs attractive for miniature applications such as cell phones, laptops,

and battery chargers for consumer electronics, to mid-size applications powering electronics on RVs, boats, or camping cabins. The electrolyte used in DLFC is a solid polymer membrane. Cation and anion exchange membranes are used in acid and alkaline separately.

The detailed information of DLFC is described in 1.3.1.

1.2.5.2 Proton Exchange Membrane Fuel Cell

PEMFC uses a proton conductive polymer membrane as an electrolyte. It is a type of fuel cell being developed for portable applications as well as for stationary fuel cell applications. Their distinguishing features include lower temperature ranges (50 to 100 °C) and a special polymer electrolyte membrane.

In a very basic form it has only two catalyst layers and a proton exchange membrane. The proton conductivity of the membrane is a very important factor in PEM technology. Nafion®, a sulfonated tetrafluoroethylene based fluoropolymer-copolymer discovered in the late 1960s by Walther Grot of DuPont [6], is probably the most studied and employed electrolyte for PEMFC.

1.2.5.3 Alkaline Fuel Cell

The alkaline fuel cell is one of the most developed fuel cell technologies. NASA has used alkaline fuel cells since the mid-1960s, in Apollo-series missions and on the Space Shuttle. The oxygen reduction kinetics is much faster in alkaline electrolyte than in acid, which makes the AFC a more efficient system.

AFCs use an aqueous solution of potassium hydroxide as the electrolyte, with typical concentrations of 30-45%. The AFC has the highest electrical efficiencies of all fuel cells but it only works properly with very pure gases, which is considered a major drawback in most applications. In the presence of CO_2, carbonates form and precipitate:

$$CO_2 + 2OH^- \rightarrow CO_3^{2-} + H_2O \tag{1-7}$$

The carbonates can lead to potential blockage of the electrolyte pathways and electrode pores.

However, despite its early success and leadership role in fuel cell technology, AFCs have fallen out of favor with the research community and have been eclipsed by the rapid development of the PEMFC as the technology of choice for vehicular applications.

1.2.5.4 Phosphoric Acid Fuel Cell

Phosphoric acid fuel cells are a type of fuel cell that uses liquid phosphoric acid as an electrolyte. They were the first fuel cells to be commercialized. Since the 1970s, more than 500 PAFC power plants have been installed and tested around the world.

The operating temperature of the PAFC is typically between 150 and 200 °C [7]. The operating temperature is found to be a compromise between the electrolyte conductivity (that increases with temperature) and cell life (that decreases when the temperature is increased). At an operating range of 150 to 200 °C, waste heat from SOFC systems may be captured and reused, increasing the theoretical overall efficiency to as high as 80%. PAFCs are CO_2-tolerant which broadens the choice of fuels they can use.

Despite the excellent technical characteristics, the large diffusion of PAFC in the market has slowed down because of economic issues. A study survey shows that the number of power plant installations grew from 1990 to 2000, while, after 2000, more attention has been given to other fuel cell technologies, such as molten carbonate fuel cells, solid oxide fuel cells and proton exchange membrane fuel cells.

1.2.5.5 Molten Carbonate Fuel Cell

In 1960 G.H.J. Broers and J.A.A. Ketelaar reported a high temperature fuel cell [8] employing an electrolyte comprising a mixture of alkali metal carbonates constrained within a sintered disk of magnesium oxide. Cells of this type can be run continuously for several months, operating between 600 and 800 °C. Following the early work in Netherlands, development of MCFC was taken up by many groups. Materials of construction have become well established.

One advantage of the MCFC is its ability to internally reform methane due to the high operating temperatures. In addition to this, the waste heat can be used in combined cycle power plants. The high temperatures also increase the oxygen reduction kinetics dramatically, to eliminate the need for precious metal catalysts. MCFC can operate on a wide range of different fuels and are not prone to CO_2 or CO contamination.

The primary disadvantage of current MCFC technology is durability. The high temperatures and the corrosive electrolyte used accelerate component breakdown and corrosion, decreasing cell life.

1.2.5.6 Solid Oxide Fuel Cell

The solid oxide fuel cell was conceived following the discovery of solid oxide electrolytes in 1899 by Nernst [9]. Nernst reported that the conductivity of pure metal oxides rose only very slowly with temperature and remained only relatively low, whereas mixtures of metal oxides can possess dramatically higher conductivities.

SOFC, which employs a solid oxide material as electrolyte, are more stable than the MCFC because no leakage problems can occur. SOFC is a gas-solid system, so it has neither problem with water management nor flooding of the catalyst layer. SOFC operates at very high temperatures, typically between 500 and 1,000 °C. Therefore, it has the same advantages as MCFC, such as less internally reform, no CO_2 or CO contamination, less precious metal catalysts.

Up to the present, large scale SOFC units have been operated at around 1000 °C [10]. Technology of intermediate temperature SOFCs is still in a developmental stage and several technological challenges remain to be solved before this type of fuel cell can find practical applications. A SOFC that uses hydrocarbon or methanol and operates at < 500 °C may eventually become an attractive power source for electric vehicles [11].

1.2.6 Application of fuel cells

Overall fuel cell system shipments (excluding toys and education kits) in 2012 were 45,700 and annual megawatts shipped reaching a total of 166.7 MW [12]. Application of Fuel cell can be categorized into three broad areas, defined as follows: Stationary, Electric Vehicle and Portable (Table 1-1).

Table 1-1. Scheme of application type of fuel cells.

Application Type	Stationary	Electric Vehicle	Portable
Typical Power Range	0.5 kW ~ 400 kW	1 kW ~ 100 kW	5 W ~ 20 kW
Typical Technology	DAFC, PEMFC, MCFC, PAFC, SOFC, AFC	DAFC, PEMFC, AFC	DAFC, PEMFC

1.2.6.1 Stationary Power

Stationary fuel cells are used for commercial, industrial and residential primary and backup power generation. Fuel cells are very useful as power sources in remote locations, such as spacecraft, remote weather stations, large parks, communications centers, rural locations and military applications. A fuel cell system running on hydrogen can be compact and lightweight, and have no major moving parts.

Both low and high temperature fuel cells could be utilized for stationary applications. The low temperature fuel cells are advantageous in a quicker start-up time. The high temperature systems generate high grade heat, which can directly be used as in a heat cycle steam or indirectly by incorporating the fuel cell system into a combined cycle.

1.2.6.2 Electric Vehicle

Fuel cells in vehicles create electricity to power an electric motor, generally using oxygen from the air and hydrogen. A fuel cell vehicle that is fueled with hydrogen emits

only water and heat, but no tailpipe pollutants; therefore it is considered a Zero Emission Vehicle.

For vehicle applications, the available space is much more critical and fast response and start-up times are required. Thus, only the low temperature systems are applicable.

The controversial AFC has been proven to be a suitable system for hybrid vehicles as long as a circulating electrolyte is used and pure hydrogen is supplied to the fuel cell. Pure hydrogen distribution centers are not widely spread over the world and, thus, it is to be predicted that AFC vehicles will be limited to specified types (e.g., fleet buses and other centralized vehicles).

The PEMFC is regarded as ideally suited for transportation applications due to its high power density, high energy conversion efficiency, compactness, lightweight, and low-operating temperature (below 100 °C). However, among all applications for fuel cells the transportation application involves the most stringent requirements regarding volumetric and gravimetric power density, reliability, and costs.

1.2.6.3 Portable Power

For small power applications like laptops, camcorders, and mobile phones the requirements of the fuel cell systems are even more specific than for vehicle applications. Low temperatures are necessary and therefore PEM fuel cells are chosen. Possibilities for fuel cell systems are the combination of PEM with hydrogen evolution from hydrolysis of metal hydrides. Other fuel cells are, therefore, not suitable for this kind of applications.

1.2.7 Summary

Fuel cells will make a valuable contribution to future power generation facilities. They improve the flexibility and increase the options for many applications. Their main property is the high electrical efficiency compared to other energy conversion devices. Both the low-temperature and the high-temperature fuel cells have their advantages and disadvantages depending on the application. The best suited fuel cell depends on the requirements of the application. A certain type of fuel cell is superior for a certain application.

Fuel cell systems are commercial products in many areas, such as stationary application and some small power devices. The imminent commercialization of fuel cells in areas of high turnover, such as vehicle propulsion, battery replacement, and stationary power generation, has accelerated the research and development dynamics considerably.

1.3 Anion Exchange Membrane Direct Liquid Fuel cells

1.3.1 Direct Liquid Fuel Cells

Fuel cells, the energy converting devices with a high efficiency and low/zero emission, have been attracting more and more attention due to high-energy demands, fossil fuel depletions, and environmental pollution throughout the world. For hydrogen gas fed fuel cells at the current technological stage, hydrogen production, storage, and transportation are the major challenges in addition to cost, reliability and durability issues. The Direct Liquid Fuel Cell (DLFC) is a special form of low-temperature fuel cells based on PEM technology. In the DLFC, small organic molecules (SOMs) are directly fed into the fuel cell without the intermediate step of reforming the fuel into hydrogen. SOMs, the fuel used in DLFCs, have advantages compared to hydrogen as they can be easily handled, stored and transported using the present gasoline infrastructure with only slight modifications. Furthermore, their energy densities are higher, e.g. 16 MJ/L and 23 MJ/L for methanol and ethanol, than liquid hydrogen which is 9 MJ/L.
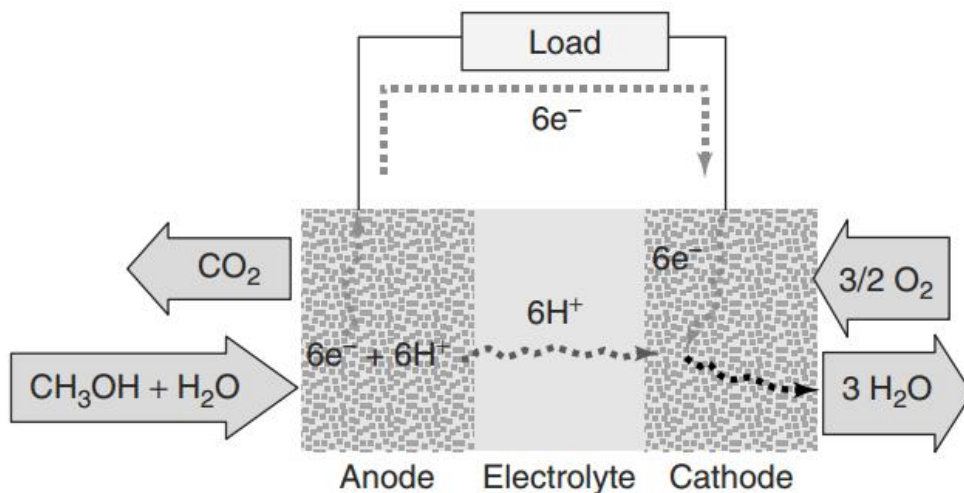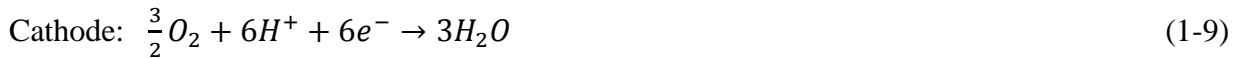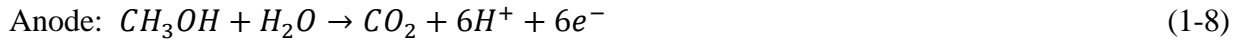

Figure 1-7. Schematic diagram of reactions and processes taking places inside DMFC [13].

During all those low molecular weight molecules (e.g. methanol, ethanol, ethylene glycerol, propanol and propanodiol, formic acid), methanol has been mostly investigated in depth. The basic operating principle of Direct Methanol Fuel Cell (DMFC) is shown in Fig. 1-7. The chemical reactions for the DMFC system can be expressed as follows:

Anode: $CH_3OH + H_2O \rightarrow CO_2 + 6H^+ + 6e^-$ (1-8)

Cathode: $\frac{3}{2}O_2 + 6H^+ + 6e^- \rightarrow 3H_2O$ (1-9)

Overall: $CH_3OH + \frac{3}{2}O_2 \rightarrow CO_2 + 6H_2O$ (1-10)

The common operating temperature of DMFC is in the range $50 - 120\ °C$, where high temperatures are usually pressurized.

Current DAFCs are limited in the power they can produce, but can still store high energy content in a small space. This means they can produce a small amount of power over a long period of time. This makes them ideal for smaller vehicles and portable devices.

1.3.2 Direct Ethanol Fuel Cells

There are several disadvantages of DMFCs. First, methanol is toxic for human beings and especially for optical nerve. Second, the sluggish anode kinetics and methanol crossover are still the main challenges to DMFC's commercialization despite that extensive efforts have been devoted. But most of all, the main source of methanol is fossil resources which is non-renewable. Therefore, finding the replacement of methanol is urgent. During the attempts to identify fuels for DAFC, ethanol is considered to be an attractive and promising one at least for the following reasons: (i) natural availability, (ii) renewability, (iii) higher power density, (iv) non-toxicity.

1.3.2.1 How ethanol is made?

Ethanol is produced both as a petrochemical, through the hydration of ethylene and, via biological processes, by fermenting sugars with yeast. Which process is more economical depends on prevailing prices of petroleum and grain feed stocks.

Ethylene hydration

About 5% of the ethanol produced in the world in 2003 was actually a petroleum product. Ethanol is made from petrochemical feed stocks, primarily by the acid-catalyzed hydration of ethylene, represented as following:

$$C_2H_4 + H_2O \rightarrow CH_3CH_2OH \tag{1-11}$$

The catalyst is most commonly phosphoric acid, adsorbed onto a porous support such as silica gel or diatomaceous earth.

Fermentation

The vast majority of ethanol for use as fuel is produced by fermentation of biomass (Figure 1-8). When certain species of yeast metabolize sugar in reduced-oxygen conditions they produce ethanol and carbon dioxide. The chemical equations below summarize the conversion:

$$C_6H_{12}O_6 \rightarrow 2CH_3CH_2OH + 2CO_2 \tag{1-12}$$

$$C_{12}H_{22}O_{11} + H_2O \rightarrow 4CH_3CH_2OH + 4CO_2 \tag{1-13}$$

Fermentation is the process of culturing yeast under favorable thermal conditions to produce alcohol. This process is carried out at around 35 – 40 °C.

To produce ethanol from starchy materials such as cereal grains, the starch must first be converted into sugars. For fuel ethanol, the hydrolysis of starch into glucose can be accomplished more rapidly by treatment with dilute sulfuric acid, fungal amylase production, or some combination of the two.

Cellulose

Cellulosic ethanol is produced from wood, grasses, or the inedible parts of plants. Production of ethanol from cellulosic materials has the advantage of abundant and diverse raw material compared to sources such as corn and cane sugars, but requires a greater amount of processing to make the sugar monomers available to the microorganisms typically used to produce ethanol by fermentation. The two ways of producing ethanol from cellulose are under development. The first type uses enzymes to break complex cellulose into simple sugars, followed by fermentation and distillation. The second way is called gasification which

transforms the cellulosic raw material into gaseous carbon monoxide and hydrogen. These gases can be converted to ethanol by fermentation or chemical catalysis.
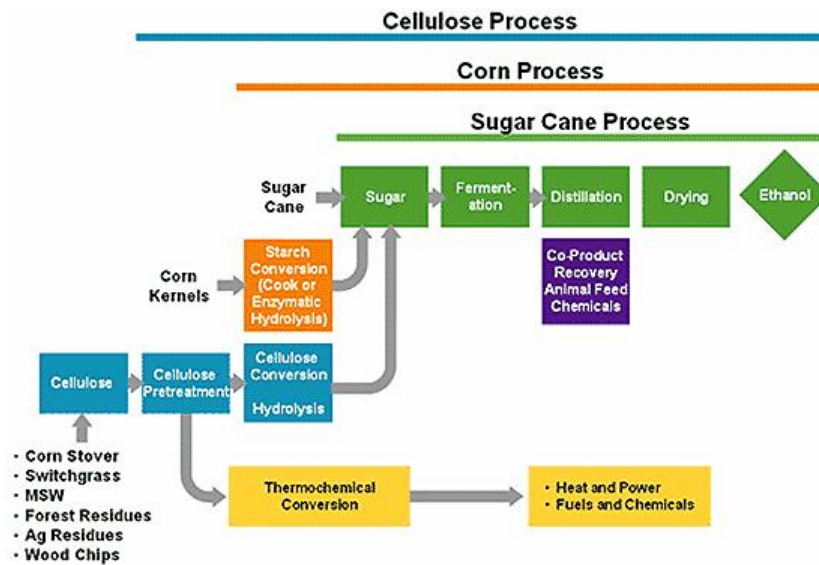
Figure 1-8. Production of ethanol from biomass [14].

1.3.2.2 The carbon cycle of direct ethanol fuel cells

As using biomass to produce ethanol, and the energy discharged from direct ethanol fuel cells can charge the vehicle or portable device releasing CO_2. Then the CO_2 can be absorbed by biomass. In the end, the whole carbon cycle is totally clean (Figure 1-9).

Hence, ethanol is a sustainable, carbon-neutral fuel source, and DEFC is clearly the best choice for producing sustainable energy in the future.
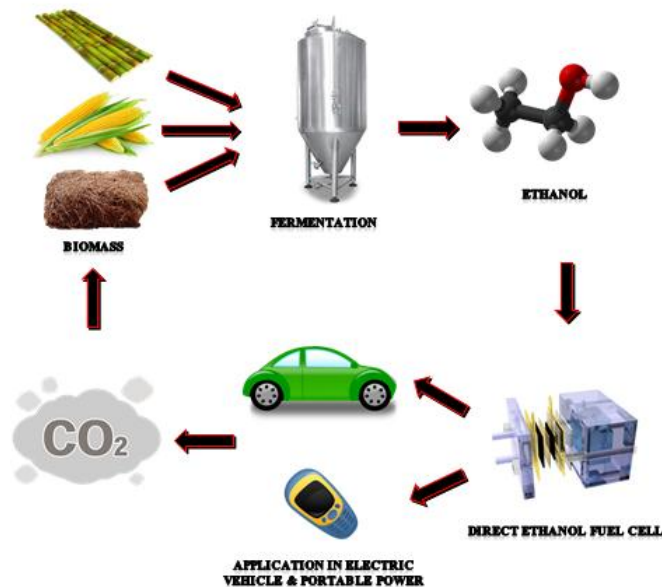
Figure 1-9. The schematic of carbon cycle of direct ethanol fuel cells.

1.3.2.3 Research status and current bottlenecks of DEFCs

Great attention has been paid the last decade to the DEFCs. Past research on the development of DEFC has focused mainly on the PEM-DEFCs that use PEM as the electrolyte. The advantage of PEM-DEFC is that the entire system setup and all the components can be the same as those in current DMFC technologies that also use PEMs. Lots of researches have been focused on the Ethanol Oxidation Reaction (EOR). Zhou et al. [15] showed that the sequence of catalytic activity for the EOR is PtSn>PtRu>PtW>PtPd>Pt, which is the state-of-the-art anode catalyst for DEFCs. Although tremendous efforts have been expended on developing EOR catalysts for PEM-DEFC, the performance of PEM-DEFC remains low even at relatively high operating temperature. The low performance of this type of fuel cell is mainly because the kinetics of the EOR in acid media is slow, leading to a large activation loss. Another critical obstacle that limits the wide application of PEM-DEFC is the cost of the system, not only because a considerable amount of Pt-based catalysts at both the anode and cathode is required but also because acid electrolyte membranes (typically Nafion®) are expensive.

1.3.3 State of the art—Anion Exchange Membrane Direct Ethanol Fuel cells

Unlike in acid media, the kinetics of both the EOR and ORR in alkaline media is much faster and allows the use of non-precious metal catalysts to reduce the cost of the fuel cell. Similar to the use of PEM in acid fuel cells, the use of an anion-exchange membrane instead of a caustic alkaline liquid electrolyte in an alkaline fuel cell can solve carbonation and other related problems, such as electrolyte leakage and precipitation of carbonate salts. AEM-DEFCs have recently attracted increasing attention due to the above reasons.

1.3.3.1 Principle
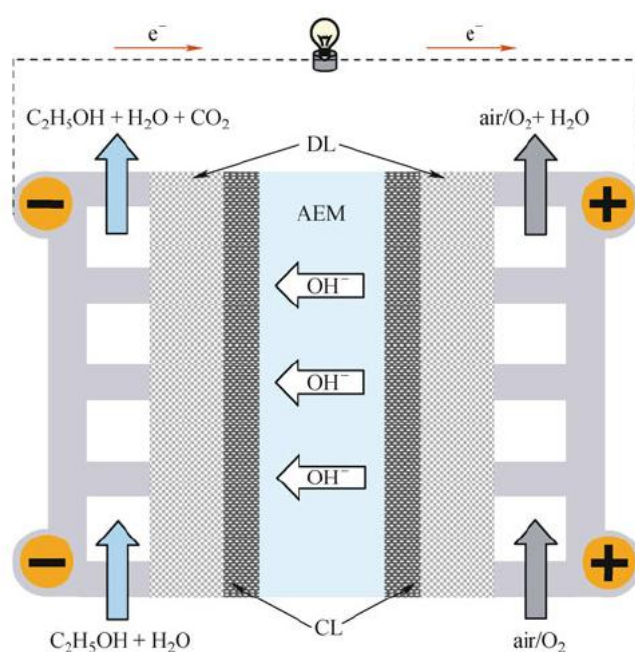
Figure 1-10. Schematic of alkaline direct ethanol fuel cell [16].

Figure 1-10 illustrates a typical alkaline DEFC setup which consists of a membrane electrode assembly (MEA) sandwiched by an anode and a cathode bipolar plate. The MEA, which is regarded as an integrated multi-layered structure, is composed of Diffusion Layer (DL), Catalyst Layer (CL) and an AEM. The function of the membrane is to conduct hydroxyl ions from the cathode to the anode and act as a separator between the anode and cathode electrodes.

At the anode side, ethanol is oxidized to generate electrons, water, and CO_2 according to:

$$CH_3CH_2OH + 12OH^- \rightarrow 2CO_2 + 9H_2O + 12e^- \tag{1-14}$$
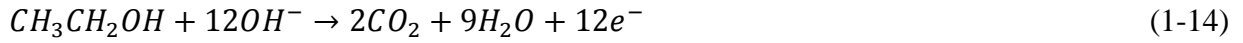
The water in ethanol solution, along with that produced from the EOR, diffuses through the membrane to the cathode CL, while the electrons travel through an external circuit to the cathode. On the cathode, the oxygen/air provided by the cathode flow field is transported through the cathode DL to the cathode CL, where the oxygen reacts with water from the anode to produce hydroxide ions according to:

$$3O_2 + 6H_2O + 12e^- \rightarrow 12OH^- \tag{1-15}$$

However, it should be noted that with the state-of-the-art anode catalysts, the complete oxidation of ethanol expressed by Eq. (1-14) is not achieved. The main product of the reaction is acetate rather than CO_2 as following:

$$CH_3CH_2OH + 5OH^- \rightarrow CH_3COO^- + 4H_2O + 4e^- \tag{1-16}$$

Hence, the actual overall reaction in the alkaline DEFC is:

$$CH_3CH_2OH + O_2 + OH^- \rightarrow 2CH_3COO^- + 2H_2O \tag{1-17}$$

1.3.3.2 Membrane

In terms of the ionic conduction mode within the polymer structure, anion-exchange membranes can be classified into two types: the polyelectrolyte membrane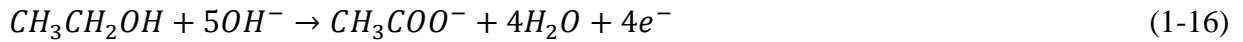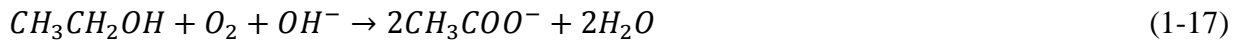 and the alkali-doped polymer membrane. The development of these two types of AEM, including its composition, ionic conductivity, ethanol permeability, and thermal and chemical stability, is described below.

The polyelectrolyte membrane is essentially an ionomer. The ionic function groups (typically quaternary ammonium) are grafted on the skeleton of the polymer backbone, and the mobile hydroxyl ions are associated to each ionic function groups to maintain membrane electro-neutrality. A typical commercial product of polyelectrolyte membranes is the A201 membranes by Tokuyama; it is composed of quaternary ammonium groups grafted on a hydrocarbon polymer backbone. To date, a number of polymer materials as the backbone have been investigated, including chitosan [17], poly(2,6-dimethyl-1,4-phenylene oxide) (PPO) [18], poly(vinylbenzyl chloride) (PVBCl) [19], poly(tetrafluoroetheneco-hexafluoropropylene)

(FEP) [20], and poly(ethylene-co-tetrafluoroethylene) (ETFE) [21]. The quaternary ammonium group-based AEMs have particularly low thermal and chemical stability. There are mainly two degradation mechanisms: direct nucleophilic displacement and Hoffmann elimination reaction.

The alkali-doped polymer membrane is composed of electronegative heteroatoms (typically nitrogen) that interact with the cations of alkali by a donoracceptor link. A typical sample for alkali-doped polymer membranes is the KOH-doped polybenzimidazole (PBI) membrane. Savadogo et al. [22] reported that the ionic conductivity of KOH-doped PBI membrane is in the range of $5*10^{-5} - 10^{-1}$ S/cm. In addition, the KOH-doped PVA membrane exhibited excellent thermal and chemical stability to high KOH concentration (10 M) at a high temperature of 120°C. The stability of the alkali-doped polymer membranes is superior to the polyelectrolyte membranes. Leykin et al. [23] showed that the ethanol permeability of KOH-doped PBI membrane first increased and then decreased with the increase in the KOH concentration. Ethanol permeability through KOH-doped PBI membrane was 6.5×10^{-7} cm^2/s, which is much lower than that of Nafion$^{®}$ membrane. The reason is that Nafion membranes swelled more significantly than KOH-doped PBI membranes.

In summary, the ionic conductivity and the thermal and chemical stability of both types of membranes are still low. Hence, significant work is required to improve membrane performance.

1.3.3.3 EOR electrocatalysts

Platinum is the best known material for the dissociative adsorption of small organic molecules at low temperatures. PtRu/C and PtSn/C have been widely accepted as the most effective catalysts for EOR in acid media [24-25]. However, Pt is scarce and expensive. Palladium has recently attracted attention as an alternative catalyst for the ethanol oxidation reaction. Unlike the Pt-based catalysts, the Pd-based catalysts show better tolerance to the CO-containing intermediates. Moreover, Pd is 50 times more abundant than Pt on earth. Above all, Pd shows higher catalytic activity for EOR than Pt in alkali. To further enhance the performance of Pd for the EOR in alkali, many efforts have been made. The crucial important parameters for Pd catalytic activity are the size, morphology, shape, dispersity and the nature of the support material.

There are continues efforts to improve the electrocatalytic performance of Pd towards EOR in alkali. Morphology-controlled Pd, such as spherical sponge-like Pd [26], nano-porous Pd [27], Pd nanowires [28], Tetrahexahedral Pd nanocrystals [29], have been synthesized and investigated. The other way to increase the activity is to deposit Pd in highly dispersed form on various supports, namely Ti [30], multi-walled carbon nanotube [31], graphene oxide [32], titanium nitride [33], titania nanotube array [34]. In addition, some effort has been devoted to employ Pd-alloys looking for a synergetic effect between Pd and the alloying element. So far, such an effect has been observed on Pd–Au [35-36], Pd–Ag [37-38], Pd–Ni [39-40]. Furthermore, Pd-based catalysts have been decorated with oxides (CeO_2 [41-42], NiO [41], MnO_2 [41], Co_3O_4 [41], TiO_2 [43], In_2O_3 [44]) to get significant promotion effect on the catalytic activity and stability for EOR.

Unlike the methanol oxidation reaction, EOR undergoes both parallel and consecutive oxidation reactions, resulting in more complicated adsorbed intermediates and byproducts. Most importantly, the complete oxidation of ethanol to CO_2 requires the cleavage of C–C bond, which is between two atoms with little electron affinity or ionization energy, making it difficult to break the C-C bond at low temperatures. Zhao et al. [45] studied the mechanism of EOR on the Pd catalyst using the cyclic voltammetry method and suggested that the dissociative adsorption of ethanol was rather quick and that the rate-determining step was the removal of adsorbed ethoxi species by the OH_{ads} groups on Pd. At higher potentials, the kinetics was affected by both the adsorption of OH_{ads} groups and the formation of the inactive oxide layer on Pd. The theoretical analysis using the first-principles method based on the density functional theory [46] showed that EOR on the Pd catalyst in acid media was difficult due to the lack of OH_{ads} groups; however, in alkaline media, both ethanol and sufficient OH_{ads} groups could adsorbed on the Pd catalyst, leading to continuous ethanol oxidation. In-situ Fourier transform infrared spectroscopy combined with cyclic voltammetry investigation shows that the main oxidation product was acetate when the OH^- concentration was higher than 0.5 M; CO_2 formation was observed only at a pH value equal or smaller than 13 [47]. The selectivity for ethanol oxidation to CO_2 was determined as low as 2.5% in the potential region of −0.60 to 0.0 V vs. SCE [48]. NMR spectroscopy was also used to observe anode exhaust and proved that ethanol was selectively oxidized to acetate on the Pd catalyst in alkali [31].

1.3.3.4 ORR electrocatalysts

Cathode performance in alkaline media is generally higher than that in acid media. The improved performance can be attributed to both the inherently faster kinetics of the ORR and the lower degree of the adsorbed ions from the supporting electrolyte onto the electrode surface in alkaline media [49].

Alkaline electrolytes present many opportunities for non-Pt catalysts for the ORR. Materials that have little or no measurable activity for the ORR in acid have substantial levels of activity in alkaline solution. Thus far, a variety of materials have been investigated for the ORR in alkaline media, including Ag [50], manganese oxide [51], Co_3O_4 [52]. Carbon has also been noted to show catalytic activity toward the ORR in alkaline media [53].

Metal complexes of organic compounds have received considerable attention recently as possible catalysts for the cathodic reduction of oxygen [54-55]. Metal phthalocyanines (Pc), in particular, are known to be electrochemically active for ORR. The electrocatalytic activity of metal Pc has been found to depend considerably on the nature of the central metal ion [56]. The order of decreasing electrocatalytic activity is: Fe > Co > Ni > Cu > H_2. The electrocatalytic activity also depends to some extent on the degree of polymerisation, on the substitution of the ligand, and on the nature of the support on which the catalyst is carried.

In summary, under alkaline conditions, the kinetics of both EOR and ORR become more facile than in acidic media, making it possible to use non-platinum catalysts.

1.3.3.5 Single cell design and performance

The ionic conductivity of anion-exchange membranes and the catalytic activity of anode catalysts are still low. The applications of the state-of-the-art membranes and catalysts to the alkaline DEFC setup still cannot result in a satisfactory performance. An effective approach to increase the kinetics of both EOR and ORR and enhance the ionic conductivity of the membrane is to add an alkali (typically the KOH) to the fuel solution. A number of works that used A201 membranes with added alkaline ethanol solutions have been reported [42, 57-58]. Fujiwara et al. [57] compared cell performance between acid- (using the Nafion-117 membrane) and alkaline-based (using A201 membrane) DEFCs with PtRu and Pt as the anode and cathode catalysts, respectively. The maximum power density of DEFCs significantly increased from 6 mWcm^{-2} to 58 mWcm^{-2} at room temperature and atmospheric pressure when the electrolyte membrane was changed from CEM to AEM. The anode and cathode polarization curves showed a decrease in the anode potential and an increase in the cathode

potential for AEM-type DEFCs compared to CEM-type. This suggests that AEM-type DEFCs have superior catalytic activity toward both ethanol oxidation and oxygen reduction in alkaline medium than in acidic medium. Using Pd as anode and non-noble metal as cathode instead of Pt, the performance is comparable and even better. Bianchini et al. [58] using the Pd-(Ni-Zn)/C anode catalyst and Fe–Co K-14 Hypermec™ as cathode, the passive alkaline DEFC at room temperature could yield a power density of as high as 55 mW/cm^2, whereas the active AEM DEFC delivered up to 160 mW/cm^2 with an oxygen flow rate of 200 sccm at 80 °C. Cell performance based on the alkali-doped PBI membrane has also been studied. Modestov et al. [59] reported the performance of the air-breading alkaline DEFC using RuV/C anode and TMPhP/C cathode, and the peak power density of was 100 mW/cm^2 at 80 °C.

To enhance cell performance further, significant research should also be conducted in the aspects of understanding species transport mechanisms and designing new electrode structures.

1.3.4 Summary

Ethanol is a sustainable, carbon-neutral transportation fuel source. It is an ideal fuel source for direct oxidation fuel cells for portable and mobile applications because it offers multiple advantages over hydrogen and methanol, including higher energy density and ease of transportation, storage, and handling. However, conventional DEFCs that use Nafion membranes and platinum-based catalysts exhibit extremely low performance. When going from acid to alkali, DEFC can use non-platinum catalysts both at anode and cathode showing considerable performance. This alkaline DEFC offers the advantage of low cost resulting from relatively cheaper membranes and non-platinum catalysts compared with those in acid DEFC. However, the power output of the alkaline DEFCs must be substantially improved before widespread commercialization is possible. Such improvement depends on finding solutions for many critical issues. The electrode design must be optimized, which critically depends on a clear understanding of mass/charge transport in nano-sized electrode structures. The following are some of the critical issues that need to be addressed in the future:

1) The cell performance, not only the power density but also the long time delivered energy and energy efficiency, of alkaline DEFCs should be better understood.

2) Cell design in connection with the KOH concentration and ethanol concentration should be investigated in order to optimize the cell performance of alkaline DEFCs.

3) Anode catalysts: Pd-based catalysts show appreciable performance toward the EOR in alkaline media. Nevertheless, both the activity and durability of Pd catalyst for the EOR in alkaline media need to be enhanced further, and the design of multi-metallic electro-catalysts is essential.

4) Cathode catalysts: A challenging issue in the cathode material is how to enhance the catalytic activity of non-Pt catalysts and make them comparable with that of Pt.

5) Membranes: The significant improvement is needed to upgrade OH^- conductivity and thermal stability of existing membranes.

2. Electrocatalyst Synthesis and Characterization

2.1 Electrocatalyst synthesis

2.1.1 Nanoparticle

2.1.1.1 Pd/C anode catalyst

Electrocatalysts with two different metal loading, 5 and 20 w.t.%, have been synthesized.

Pd (5 w.t. %)/C: 4.5 g of Vulcan XC-72 was suspended in 250 ml of ethylene glycol and sonicated for 20 min in a 500 ml three-neck round-bottomed flask. Then an aqueous solution of H_2O (50 ml) and ethylene glycol (50 ml) and 6 ml HCl (37%) with 445 mg of dissolved $PdCl_2$ were added drop by drop to the resulting solution under stirring in a N_2 stream. After adequately stirring, an alkaline solution of NaOH (5 g) in H_2O (10 ml) and ethylene glycol (35 ml) was introduced in the reactor which then was heated at 125 °C for 3 h again under a N_2 atmosphere. Then the mixture was cooled down to room temperature. The solid product was filtered off and washed with H_2O to neutral pH. The final product was dried in vacuum oven at 40 °C. An amount of 4.47 g of catalyst was obtained. This electrocatalyst was used in in the experiments presented in chapter 3 and 7. Pd content = 5.2 wt. % (ICP-AES).

Pd (20 w.t. %)/C: 6.0 g of Vulcan XC-72 was suspended in 250 ml of ethylene glycol and sonicated for 20 min in a 1 l three-neck round-bottomed flask. Then an aqueous solution of H_2O (50 ml) and ethylene glycol (50 ml) and 20 ml HCl (37%) with 2 g of dissolved $PdCl_2$ were added drop by drop to the resulting solution under stirring in a N_2 stream. After adequately stirring, an alkaline solution of NaOH (13.2 g) in H_2O (10 ml) and ethylene glycol (35 ml) was introduced in the reactor which then was heated at 140 °C for 3 h again under a N_2 atmosphere. Then the mixture was cooled down to room temperature. The solid product was filtered off and washed with H_2O to neutral pH. The final product was dried in vacuum oven at 40 °C. An amount of 7.79 g of catalyst was obtained. This electrocatalyst was used in the experiment presented in the chapter 4. Pd content = 20.3 wt. % (ICP-AES).

2.1.1.2 Pd-CeO$_2$/C anode catalyst

Vulcan XC-72 (4 g) was added to a solution of Ce(NO$_3$)$_3$.6H$_2$O (5.31g) in H$_2$O (250ml). The mixture was stirred for 30 min and then sonicated for 30 min at room temperature. After adjusting the pH to 12 with 1.5 M KOH, the resulting suspension was stirred for 2 h. The product was separated by filtration and washed with H$_2$O until neutral pH was obtained. The product was dried at 65 °C under vacuum oven to constant weight. After physical milling, the product was calcined in a tube furnace at 250 °C for 2 h and cooled down in Ar stream. The product is CeO$_2$/C with a ceria content of 35 w.t. % (yield: 6.02 g). Following from that CeO$_2$/C was suspended in water (500 mL), and the resulting slurry was sonicated for 10 min. And then a solution of K$_2$PdCl$_4$ (0.93 g, 2.84 mmol) in water (250 mL) was slowly added (ca. 3 h) to this mixture under vigorous stirring, followed by an aqueous solution of 1M KOH (14.5 mL). Next, ethanol (100 mL) was added to the resulting mixture and then refluxed for 30 min. The desired product Pd–CeO$_2$/C was filtered off and washed several times with distilled water to neutrality and finally dried under vacuum at 40 °C until constant weight (yield: 6.25 g). This electrocatalyst was used in the experiment presented in the chapter 3. Pd content = 4.6 wt. % (ICP-AES).

2.1.1.3 FePc–CoPc/C cathode catalyst

Ketjen Black (5 g) was added to an equimolar mixture of FePc (1.15 g) and CoPc (1.15 g) in THF (100 mL) that had previously stirred for 30 min at room temperature and further sonicated for 30 min. The solvent was then removed under reduced pressure and the solid residue of FePc–CoPc/C was dried under high vacuum and then weighed up as the yield of 7.2 g. FePc–CoPc/C (7.0 g) was introduced into to a quartz tube and heated at 600 °C (heated up as 20 °C/min from room temperature) under a flow of nitrogen (1 L/min) for 2 h. After cooling to room temperature under a nitrogen flow, the resulting black material of FePc–CoPc/C (600) (yield 6.8 g) was removed and stored under nitrogen. This electrocatalyst was used in the experiments presented in the chapter 3, 4 and 7.

2.1.2 Nanostructured foil

2.1.2.1 Nanostructured palladium foil

The Square-Wave Potential (SWP) treatment has been performed through potentiostatic oxidation and reduction cycles respectively at 4.55 V for oxidation (180 s) and -1.95 V (vs. RHE) for reduction (180 s) respectively (Fig. 2-1). The whole red-ox sequence has been repeated three times. This material was used in the experiment presented in the chapter 5.
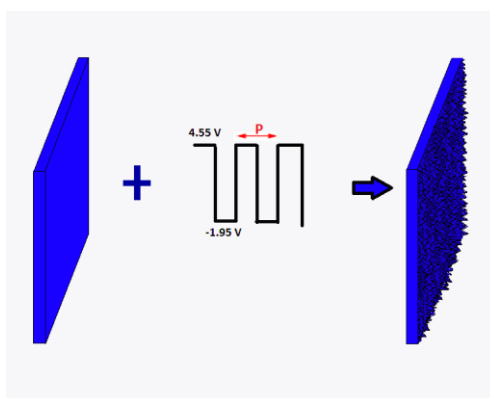
Figure 2-1. Schematics of the square wave potential treatment with three cycles. The period (P) of the square wave potential is 6 min.

2.1.2.2 Nanostructured platinum foil

The platinum activation by square wave potential treatment is performed according to the schematic in Figure 2-2. The treatment of the polycrystalline Pt foil was performed with a fixed duration of 360 minutes through a repetitive square wave potential bounded between 4.55 V and -1.95 V in 2 M KOH electrolyte. Wave periods of 6 min (60 full waves), 120 min (3 full waves), and 360 min (1 full wave) were selected for the synthesis of the samples. This material was used in the experiment presented in the chapter 6.
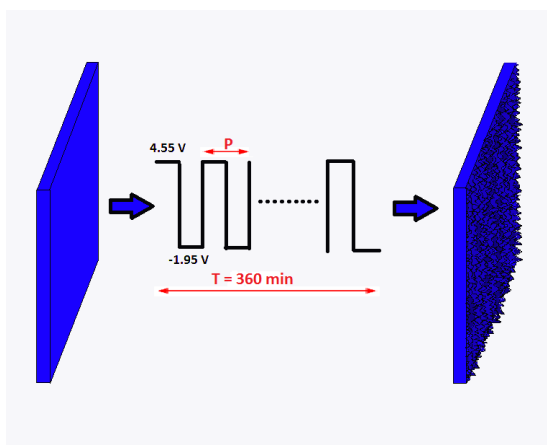
Figure 2-2. Schematic of the square wave potential treatment. Roughness is enhanced by the application of the square wave potential. All the treatments applied have duration of 360 min. The period (P) of the square wave is varied between 6 min and 360 min.

2.2 Morphology and structure of electrocatalyst

2.2.1 Electron microscopy

An electron microscope is a microscope that uses accelerated electrons as a source of illumination. Because the wavelength of an electron can be up to 100,000 times shorter than that of visible light photons, the electron microscope has a higher resolving power than a light microscope and can reveal the structure of smaller objects.

2.2.1.1 Transmission Electron Microscope (TEM)

The original form of electron microscope, the transmission electron microscope (TEM) uses a high voltage electron beam to create an image. The electron beam is produced by an electron gun, commonly fitted with a tungsten filament cathode as the electron source. The electron beam is accelerated by an anode typically at +100 keV with respect to the cathode, focused by electrostatic and electromagnetic lenses, and transmitted through the specimen that is in part transparent to electrons and in part scatters them out of the beam. When it passes through the specimen, the electron beam carries information about the structure of the specimen that is magnified by the objective lens system of the microscope.

We use TEM to characterize the morphology of our electrocatalysts. TEM was performed on a Philips CM12 microscope at an accelerating voltage of 100 kV. The microscope was equipped with an EDAX energy dispersive microanalysis system.

2.2.1.2 Scanning Electron Microscope (SEM)

Unlike the TEM, where electrons of the high voltage beam carry the image of the specimen, the electron beam of the scanning electron microscope (SEM) does not carry a complete image of the specimen. The SEM produces images by probing the specimen with a focused electron beam that is scanned across an area of the specimen. The electrons interact with atoms in the sample, producing various signals that can be detected and that contain information about the sample's surface topography and composition. Specimens can be observed in high vacuum, in low vacuum, in dry conditions (in environmental SEM), and at a wide range of cryogenic or elevated temperatures.

We use SEM to characterize the surface morphology of our electrocatalysts. SEM was performed by using a HITACHI S4800 microscope operating at 15 kV. Field Emission Scanning Electron Microscopy (FMSEM) was performed by using Zeiss Gemini 1530, capable of a spatial resolution 2.1 nm at 1.0 kV.

2.2.2 X-ray Diffraction (XRD)

X-ray diffraction (XRD) is a well-established analytical technique that reveals detailed information about the chemical composition and type of molecular bond of crystalline phase. It is an efficient technique to expose the crystallographic material structure.

Diffraction is a scattering phenomenon. When X-rays are incident on crystalline solids, they are scattered in all directions. In some of these directions, the scattered beams are completely in phase and reinforce one another to form the diffracted beams. The Bragg law describes the conditions under which this would occur. It is assumed that a perfectly parallel and monochromatic X-ray beam, of wavelength λ, is incident on a crystalline sample at an angle θ. The concept of x-ray diffraction can be described by the Bragg's Law.

$$n\lambda = 2d \sin \theta \qquad\qquad (2\text{-}1)$$

Where d is the interplanar spacing between atomic planes.

We use X-ray powder diffraction to characterize the chemical composition and crystalline structure of our electrocatalysts. XRD spectra was acquired at room temperature with a PANalytical X'PERT PRO diffractometer, employing CuK_a radiation (l=1.54187) and

31

a PW3088/60-graded multilayer parabolic X-ray mirror for Cu radiation. The spectra was acquired in the 2q range from 5.0 to 120.08, using a continuous scan mode with an acquisition step size of 2q=0.02638 and a counting time of 49.5 s.

2.2.3 X-ray Absorption Spectroscopy (XAS)

X-ray absorption spectroscopy (XAS) is a widely used technique for determining the local geometric and/or electronic structure of matter. The experiment is usually performed at synchrotron radiation sources, which provide intense and tunable X-ray beams.

X-ray Absorption Spectroscopy includes both Extended X-Ray Absorption Fine Structure (EXAFS) and X-ray Absorption Near Edge Structure (XANES). The normalized absorption spectra are often called XANES spectra. These spectra can be used to determine the average oxidation state of the element in the sample. The XANES spectra are also sensitive to the coordination environment of the absorbing atom in the sample. EXAFS spectra are displayed as graphs of the absorption coefficient of a given material versus energy, typically in a 500 – 1000 eV range beginning before an absorption edge of an element in the sample. XAS methodology can be broadly divided into four experimental categories that can give complementary results to each other: Metal K-edge, metal L-edge, ligand K-edge, and EXAFS.

We have investigated the palladium state in the Pd/C electrocatalyst by X-ray Absorption Spectroscopy (XAS), particularly by the analysis of the near edge structure (X - ray Near Edge Structure – XANES) in order to investigate the chemical state of the metal in the catalyst before and after having operated in a complete direct ethanol fuel cell. XAS data were collected at GILDA beamline (European Synchrotron Radiation Facility, ESRF, Grenoble [60] at the palladium-K edge (24350 eV). A Si (311) double crystal monochromator was used in dynamical focusing mode; the harmonic rejection was realized by a pair of Pt mirrors, having a cutoff energy of 32 keV. Data collection was carried out in fluorescence mode using an energy resolving (energy resolution about 300 eV) 13-elements Ge fluorescence detector.

2.2.4 Inductively coupled plasma atomic emission spectroscopy (ICP-AES)

Inductively coupled plasma atomic emission spectroscopy (ICP-AES) is an analytical technique used for the detection of trace metals. It is a type of emission spectroscopy that uses

the inductively coupled plasma to produce excited atoms and ions that emit electromagnetic radiation at wavelengths characteristic of a particular element. The intensity of this emission is indicative of the concentration of the element within the sample.

The metal content in all electrocatalysts was determined by ICP-AES by using an Intrepid Iris instrument (Thermo Elemental). The electrocatalyst (50 mg) was treated in a microwave-heated digestion bomb in sealed PTFE vessels with concentrated HNO_3 (2.0 mL) and 98% H_2SO_4 (2 mL). The heating program comprised preheating steps and a final 10 min digestion step at 220 °C. The resulting residual solutions were diluted with water to a constant volume. The solutions were then analyzed for the metal content.

2.3 Electrocatalytic properties

2.3.1 Half-cell (Three-Electrode Electrochemical Cell)
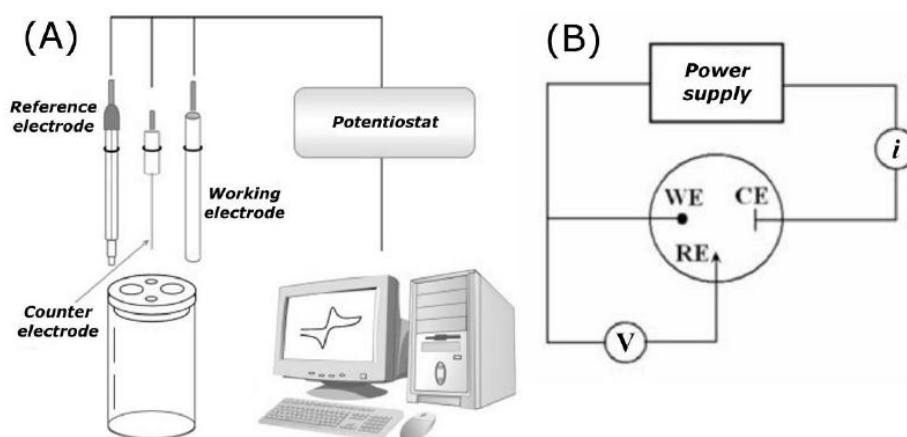
Figure 2-3. (A) Schematic representation of the typical three-electrode electrochemical cell and (B) the corresponding circuit connections.

A conventional three-electrode electrochemical cell was employed in our studies (Fig. 2-3). In potentiostatic mode, a potentiostat/galvanostat (PGSTAT) will accurately control the potential of the Counter Electrode (CE) against the Working Electrode (WE) so that the potential difference between the working electrode (WE) and the Reference Electrode (RE) is well defined, and correspond to the value specified by the user. In galvanostatic mode, the

current flow between the WE and the CE is controlled. The potential difference between the RE and WE and the current flowing between the CE and WE are continuously monitored. By using a PGSTAT, the value specified by the user (i.e. applied potential or current) is accurately controlled. The potentiostat used in this work is a Princeton 2273A Potentiostat/Galvanostat, equipped with Electrochemical PowerSuite software.

The counter electrode is used to close the current circuit in the electrochemical cell. It is usually made of an inert material (e.g. Pt, Au, graphite, glassy carbon) and usually it does not participate in the electrochemical reaction. Because the current is flowing between the WE and the CE, the total surface area of the CE (source/sink of electrons) must be higher than the area of the WE so that it will not be a limiting factor in the kinetics of the electrochemical process under investigation.

The reference electrode has a stable and well-known electrode potential and it is used as a point of reference in the electrochemical cell for the potential control and measurement. The high stability of the reference electrode potential is usually reached by employing a redox system with constant (buffered or saturated) concentrations of each participants of the redox reaction. Moreover, the current flow through the reference electrode is kept close to zero (ideally, zero) which is achieved by using the CE to close the current circuit in the cell together with a very high input impedance on the electrometer (> 100 GOhm).

During our experimental section, electrochemical Measurements with iR drop correction were performed with PARSTAT 2273 potentiostat/galvanostat (Princeton Applied Research) in a three electrode cell. There are two ways to prepare the working electrode. For the nanoparticle, glassy carbon (Sigradur G; 0.867 cm^2) covered by the electrocatalyst was loaded at the top end of the cylinder. The ink of catalyst was consisted of electrocatalyst (22 mg) and 2-propanol (2 g). The ink was sonicated for 120 min with a Branson 3200 bath. The metal loading on each electrode was determined by weighting the amount of ink deposited on the glassy carbon disk. For the nanostructure foil, the working electrode is a polycrystalline Pd/Pt disk embedded in a Teflon cylinder. Pd/Pt electrode surface has been mechanically polished with Metadi® polycrystalline diamond suspension from Buehler Company with size down to 1μm and then washed in a FALC sonic bath. An Ag/AgCl electrode was used as reference, while counter electrode was consisted of a platinum wire (0.5 mm diameter). All the solutions were purged with N_2 for 30 min before any electrochemical experiments.

The ink of cathode electrocatalyst was consisted of FePc-CoPc/C (24 mg) with 2.2 g of iso-propanol and 95 mg of a TokuyamaTM OH-type anion exchange resin in alcohol solution. The resulting suspension was sonicated for 2 h with a FALC sonic bath and then introduced into a 5mm (A = 0.1963 cm^2) teflon potted glassy-carbon rotating disk electrode tip (PINETM). Each electrode was dried for 30 min before it was mounted on the rotating disk electrode shaft and then immersed into the electrolyte. Linear sweep voltammetry of FePc-CoPc/C were carried out at an electrode rotating speed varied from 400 to 2600 rpm. The potential was swept from 1.164-0.064 V. A scan rate of 5 mV/s was applied, which is slow enough to ensure a steady state in each point of the curve.

2.2.1.1 Cyclic Voltammetry (CV)

Cyclic voltammetry is a type of potentiodynamic electrochemical measurement. In a cyclic voltammetry experiment the working electrode potential is ramped linearly versus time. After the set potential is reached in a CV experiment, the working electrode's potential is ramped in the opposite direction to return to the initial potential. These cycles of ramps in potential may be repeated as many times as desired. The current at the working electrode is plotted versus the applied voltage (i.e., the working electrode's potential) to give the cyclic voltammogram trace.

In cyclic voltammetry, the electrode potential ramps linearly versus time in cyclical phases as shown in Figure 2-4. The rate of voltage change over time is known as the experiment's scan rate (V/s). The potential is applied between the working electrode and the reference electrode while the current is measured between the working electrode and the counter electrode. These data are plotted as current (i) vs. applied potential.
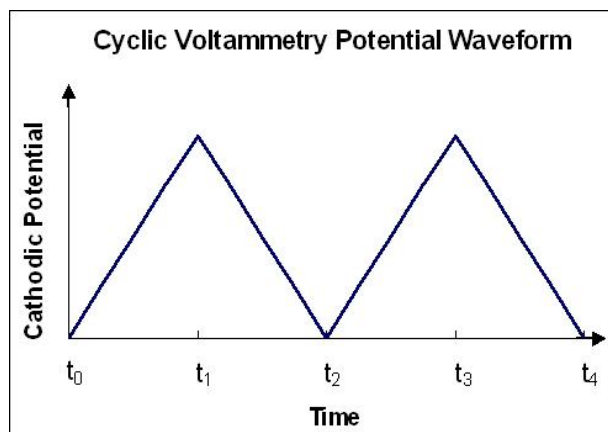
Figure 2-4. Cyclic voltammetry waveform.

2.2.1.2 Chronoamperometry

Chronoamperometry is an electrochemical technique in which the potential of the working electrode is stepped and the resulting current from faradaic processes occurring at the electrode (caused by the potential step) is monitored as a function of time. Limited information about the identity of the electrolyzed species can be obtained from the ratio of the peak oxidation current versus the peak reduction current. However, chronoamperometry generates high charging currents, which decay exponentially with time as any resistor–capacitor circuit. The Faradaic current--which is due to electron transfer events and is most often the current component of interest--decays as described in the Cottrell equation. In most electrochemical cells this decay is much slower than the charging decay--cells with no supporting electrolyte are notable exceptions. Most commonly investigated with a three electrode system. Since the current is integrated over relatively longer time intervals, chronoamperometry gives a better signal to noise ratio in comparison to other amperometric technique.
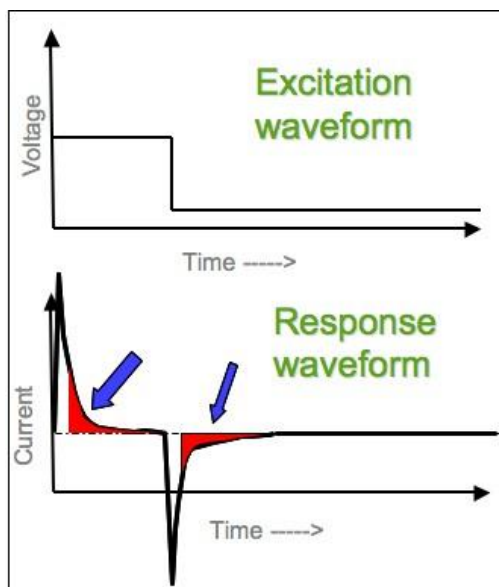
Figure 2-5. Double-pulsed chronoamperometry waveform showing integrated region for charge determination.

2.2.1.3 Chronopotentiometry

Chronopotentiometry is, as chronoamperometry, a voltammetry variant. The only difference is that, instead of time-controlled potential alteration, a constant current density is applied to a stationary working electrode and the change in potential is measured as a function of time. The chronopotentiometric curve is shown in Figure 2-6.

Figure 2-6. Potential-time curve for chronopotentiometry.

2.2.1.4 In situ Fourier Infrared spectroscopy (In situ FTIR)

Infrared spectroscopy (IR spectroscopy) is the spectroscopy that deals with the infrared region of the electromagnetic spectrum. It covers a range of te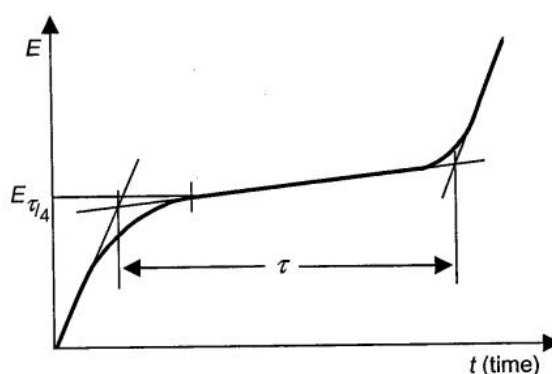chniques, mostly based on absorption spectroscopy. As with all spectroscopic techniques, it can be used to identify and study chemicals. For a given sample which may be solid, liquid, or gaseous, the method or technique of infrared spectroscopy uses an instrument called an infrared spectrometer to produce an infrared spectrum. A common laboratory instrument that uses this technique is a Fourier transform infrared (FTIR) spectrometer.

The reaction mechanisms of alcohol oxidation are complex involving several adsorbed intermediates and the formation of numerous products and by-products. The elucidation of the reaction mechanism, thus, needs to combine pure electrochemical method (cyclic voltammetry) with other physicochemical methods, such as "in situ" spectroscopic methods (infrared and UV–VIS reflectance spectroscopy) to monitor the adsorbed intermediates and "on line" chromatographic techniques to analyze quantitatively the reaction products and by-products. During all, infrared spectroelectrochemical techniques have been developed to observe surface energetic changes spectroscopically as a function of the reaction driving force.
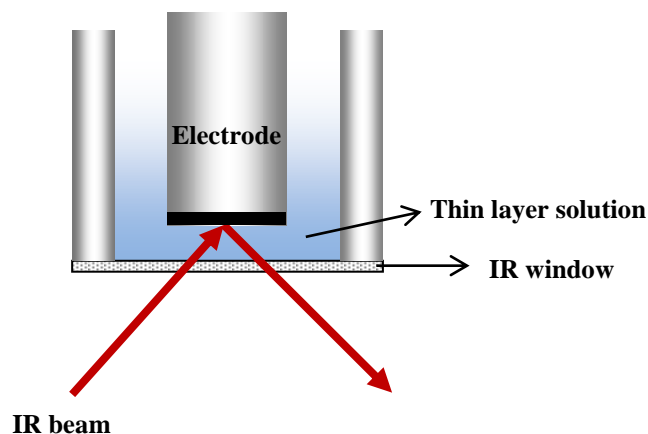

Figure 2-7. Reflectance arrangement for infrared spectroelectrochemistry employing a thin layer.

Infrared spectrometers are required for the detection of adsorbed and double or diffusion layer species. Two major problems affect the sensitivity of the measurements. The first is the large absorption of most of the radiation by the bulk solvent, especially water, which absorbs strongly throughout most of the mid and far-infrared regions. The second problem is that the number of molecules under study is usually very small, usually less than a monolayer. To overcome those problems, a special cell was designed and a special way was used to get spectra acquisition. The problem of solvent absorption is minimized by using a thin-layer cell (Figure 2-7). An infrared transparent window (calcium fluoride, silicon, zinc selenide) is mounted at the end of the cell. The working electrode is positioned close to the window to get a thin-layer solution.

The working electrode mounting procedure involves affixing a mirror disk of the electrode at the end of a PTFE holder, with the back side of the disk being electrically connected to a wire leading out of the cell (Fig. 2-8). A luggin reference probe is positioned about 1 mm from the edge of the working electrode. The counter electrode is typically a platinum wire or foil placed just next the working electrode to minimize solution resistance and provide a current distribution to the working electrode.

Figure 2-8. Three-electrode half-cell used in in-situ Fourier Transform Infrared (FTIR) spectroscopy.

The thin-layer cell arrangement still exhibits large solvent and electrolyte absorption. Signal-to-noise enhancement is accomplished through the signal-averaging techniques, which averaging several interferograms. The variation of reflectance with frequency is monitored at constant potential. Usually a few number of interferograms are obtained at two different

potentials. The two single-beam spectra are differenced and ratioed to the intensity at referenced potential to obtain the final normalized spectrum. The result is a difference spectrum with magnitude $\Delta R/R$, defined as following equation [61]:

$$\frac{\Delta R}{R} = \frac{R_d - R_{ref}}{R_{ref}} \qquad (2\text{-}2)$$

For small values of $\Delta R/R$, this quantity is proportional to absorbance. Both positive and negative bands may be observed. Positive bands are due to absorbance from species present at the referenced potential R_{ref}, while negative bands are due to absorbers prevalent at the detected potential R_d. The measured spectrum shows only changes in reflectance caused by changes in potential.

Electrochemical in-situ FTIR reflection spectroscopy has been performed on a Nicolet 6700 spectrometer equipped with a DTGS detector. During the *in-situ* FTIR spectroelectrochemical experiments, the electrode was pressed against the CaF_2 window to form a thin layer solution. Each infrared spectrum was recorded from averaging 128 interferograms at the resolution of 4 cm^{-1}. The reference spectrum was collected at 0 V vs. RHE. The working electrode potentials were increased by 0.1 V intervals from the reference potential up to 1.2 V. Each final spectrum was reported using Eq. 2-2.

2.2.1.5 Fixed energy X-ray absorption voltammetry

X-ray absorption spectroscopy (XAS) is a widely used technique for determining the local geometric and electronic structure of matter. The experiment is usually performed at synchrotron radiation sources, which provide intense and tunable X-ray beams.

For the need of synchrotron radiation, the main limit of XAS is the time needed for the recording of spectra and their interpretation. Besides, the need of quick XAS analysis is prompted by the kinetics of the reaction under study, such as potential change which is crucial for electrochemical investigations.

Fixed energy X-ray absorption voltammetry (FEXRAV) [62] is a novel rapid XAS technique applied to electrochemical systems for the in situ XAS study of electrode materials. The energy is chosen on the absorption edge in order to give the maximum contrast between

different oxidation states of a given element. It follows that any shift from the original oxidation state determines a variation of the absorption coefficient. This procedure requires the acquisition of XANES spectra of standard samples for the correct choice of the X-ray energy.

In our experiment, electrocatalyst was deposited onto a custom-made carbon disposable electrode (DRP-P-C11XX, Dropsens) as the working electrode. A PTFE cell that contains the electrolyte solution, a Pt foil counter electrode, and the reference electrode (AgCl/Ag in 0.1 M KCl). One side of the cell includes a hole that matches with the working electrode area. The working electrode is held between the PTFE cell and a polypropylene plate that also includes a hole for the X-ray beam. Fluorescence XAS data were collected at GILDA beamline (European Synchrotron Radiation Facility, ESRF, Grenoble) at the palladium edge (24370 eV and 24347 eV). A Si (311) double crystal monochromator was used; the harmonic rejection was realized by Pd mirrors, having a cutoff energy of 20 keV, and a 13-element Ge fluorescence detector. All the electrochemical measurements were carried out using a CHI potentiostat/galvanostat (model 633D) and a spectroelectrochemical cell. CV curves are recorded at 5 mV/s. All measurements were carried out at room temperature.

2.3.2 Full-cell

The heart of a fuel cell is a polymer, ion-conductive membrane. On both sides of the membrane there is a porous electrode. The electrodes must be porous because the reactant gases are fed from the back and must reach the interface between the electrodes and the membrane, where the electrochemical reactions take place in the so-called catalyst layers. The multilayer assembly of the membrane sandwiched between the two electrodes is called the Membrane Electrode Assembly (MEA). The MEA is then sandwiched between the collector-separator plates. At the same time, in multicell configuration they physically connect the cathode of one cell to the anode of the adjacent cells, and that is why they are also called the bipolar plates. They provide the pathways for flow of reactant gases and the cell structural rigidity. A schematic fuel cell component is shown in Fig. 2-9.
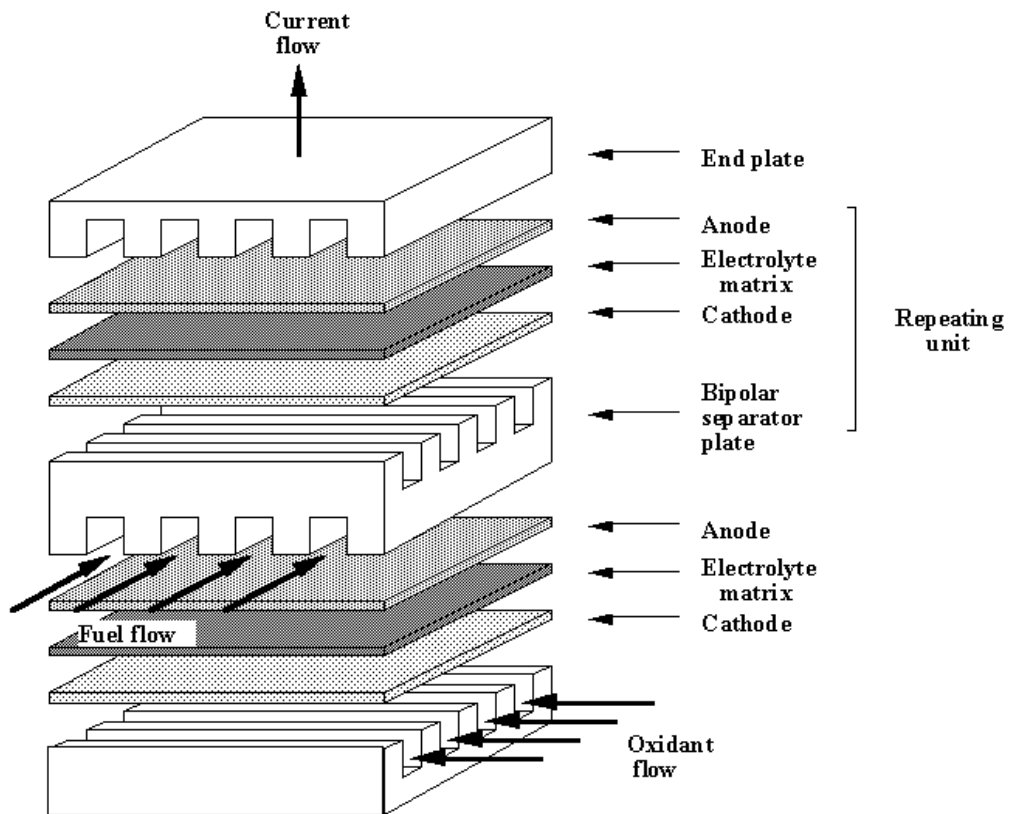
Figure 2-9. Main fuel cell components.

2.2.2.1 Polarization curve

Fuel cell performance is characterized by its polarization curve, which is a plot of cell potential vs. current density. Three distinct regions of a fuel cell polarization curve are noticeable (Figure 2-10):

- At low current densities, the cell potential drops sharply as a result of the activation polarization (slow reaction).
- At intermediate current densities, the cell potential drops linearly with current as a result of ohmic losses (cell resistance).
- At high current densities, the cell potential drop departs from linear relationship with current density as a result of more pronounced concentration polarization (slow mass diffusion).

Polarization curve is typically recorded by starting at the open circuit potential and then increasing current and taking measurements at prescribed potential or current intervals. The sweep may be done at different speeds.
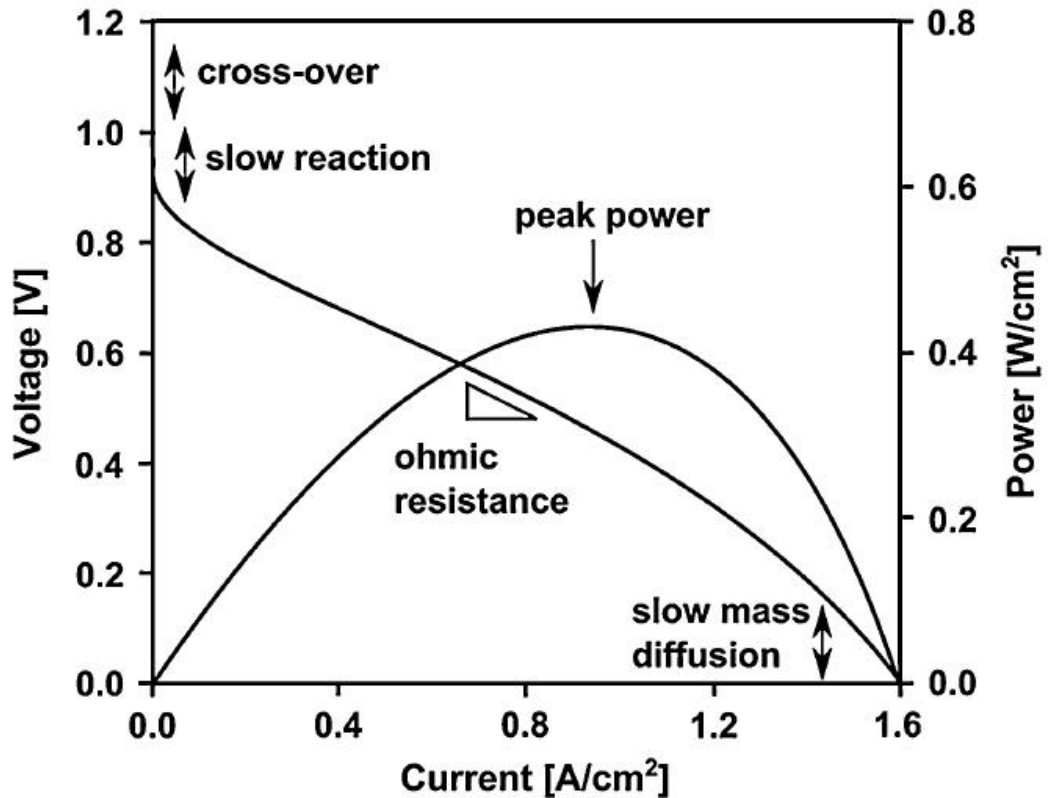
Figure 2-10. A fuel cell polarization curve and power performance curve.

2.2.2.2 Power performance curve

When a fuel cell is connected to a circuit it becomes the power source for the external load. The fuel cell is a dc power source, like a battery. To change the current through an external load, or power delivered to an external load requires changing the resistance, or impedance, of the external load, or changing the voltage of the power source. The power delivered to the external load (or useful power) is simply the product of the steady state current through the external load and voltage drop across the external load; the useful power is a function of the external load impedance. The data for the polarization curve can be simply re-plotted as power delivered to the external load as a function of the external load resistance.

2.2.2.3 Galvanostatic curve

There are good reasons for using current control in polarization curve measurements. These include the following:

1. Current control allows the superposition of multiple source and measurement instruments on a single cell or stack of cells.

2. Fuel cells are low impedance devices and can be measured with lower noise by sourcing current and measuring voltage rather than vice versa.

3. Current sources are more stable than voltage sources with the highly capacitive load of a fuel cell, resulting in precise interrupts and high frequency AC impedance information.

Low internal resistance argues against potentiostatic control in fuel cell testing. Fuel cells (especially large ones) have internal resistance in the $m\Omega$ to $\mu\Omega$ range when measured at high frequency (short interrupt).

Since potentiostatic control fixes the cell potential with respect to the voltage measure terminals, noise in the potential driving the cell will generate significant noise current through the cell's low impedance.

By contrast, under galvanostatic control, a relatively large current is forced through the cell, which is measured as a voltage across an instrument's internal current sensing resistor. Since this resistance is decades larger in value than a cell's internal resistance, noise in the measurement is a much smaller percentage of the signal. Similarly, a relatively large voltage signal can be accurately measured across the cell terminals.

Galvanostatic control allows the separation of the polarization current and the test current by taking advantage of high current source output impedance and applying superposition.
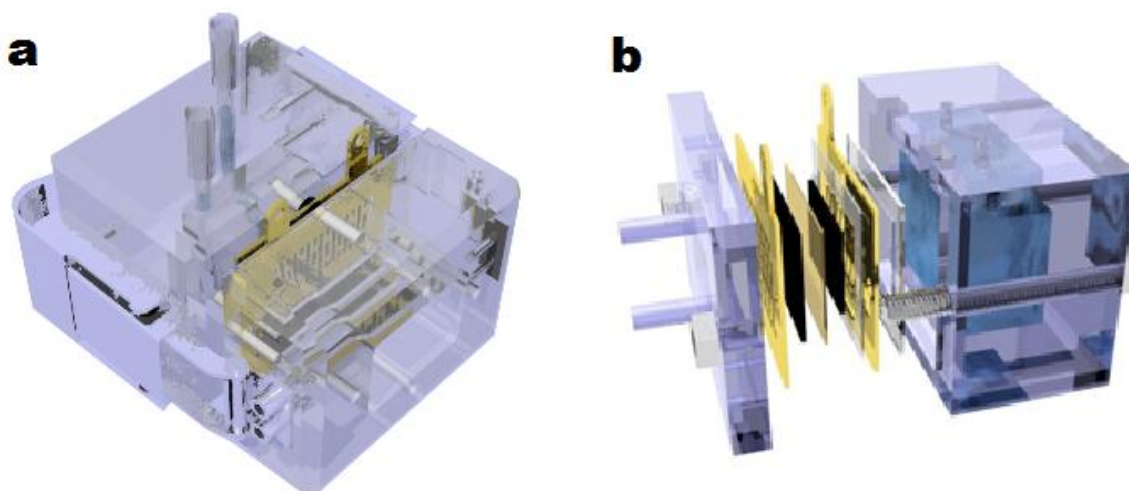
Figure 2-11. The home-made oxygen-breathing DEFC. (a) The pictorial diagram; (b) exploded view showing the MEA.

In our experiment, the home-made, oxygen-breathing fuel cell was used (Figure 2-11). The device is made of plexiglas and the electricity collectors are stainless steel plated with gold. The MEA was realized using a anode composed of electrocatalyst, a commercial Tokuyama A-201 anion exchange membrane and a cathode containing FePc-CoPc/C electro-catalyst. The membrane was conditioned in 1 M KOH solution for 1 min before assembling the MEA. The fuel loading of the anode compartment was 12 ml for each experiment. The anode catalytic ink was prepared mixing the electrocatalyst (100 mg) with water (400 mg) and a 5 w.t. % nafion solution. The resulting ink was spread onto a 5.13 cm^2 nickel foam plate to obtain a Pd loading of 1 mg cm^{-2}. The MEA was obtained by mechanically pressing anode, membrane and cathode. Silicone-rubber gaskets were employed to seal the system. Polarization and galvanostatic curves were determined on a ARBIN BT-2000 5A-4 channels potentiostat/galvanostat. All the experiments had been performed at room temperature. New MEAs were used for each experiment and then just changed the fuel on the same MEA to test the effort of aging.

3. Non-platinum Electrocatalysts for Anion Exchange Membrane Direct Ethanol Fuel Cells

3.1 Introduction

Direct alcohol fuel cells (DAFCs), especially direct methanol fuel cells (DMFCs), have been technologically exploited for both powering small portable electronics and even automotive engine. Concerns about the overall energy efficiency of DMFCs have also been recently raised [63-64]. However, the toxicity of methanol together with its flammability and high vapor pressure at room temperature severely hamper the full technological exploitation. Moreover its oxidation occurs via pathways involving the formation of adsorbed CO, causing electrocatalyst poisoning which ultimately resulting significant performance degradation.

For what reported above the substitution of methanol with ethanol has been proposed. Ethanol is far less toxic and volatile as compared to methanol and it can be easily obtained from biomass conversion with low energy processes. Bio-ethanol energy convenience has been recently supported by a variety of Life Cycle Analysis (LCA) that have shown energy return of the invested energy higher than 8 when sugarcane or cellulose are used as feedstock [65]. Furthermore the bio-ethanol industry is now continuously expanding with prediction that global ethanol supply will exceed 100 million tonnes in 2018 [66].

The development of efficient direct ethanol fuel cells appears to be an issue of outstanding importance. In the last few years the subject has experienced a continuously rising interest substantiated by the continuous growth of the published paper. Most of the studies on DEFCs reported up till now have concerned with the assessment of power density performances [42, 57-58] and the activity and stability accounting for the half-cell test of the anode electrocatalyst [26, 28-29, 33, 35-40]. The focus on the anode electrocatalyst is essential as the activation potential for ethanol oxidation is the largest contribution to the potential drop in DEFCs.

Maximum power density and stability in half-cell are parameters whose importance is fundamental. Nevertheless for a variety of applications energy efficiency as well as delivered

energy may be critical important as well. There are several reasons: i) highly efficient fuel cells minimize volume and weight through the reduction of the size of the storage systems [67] which is crucial for automotive and portable applications; ii) high fuel cell efficiency contributes to improve the energy efficiency of the whole systems thereby improving the sustainability of the technology; iii) the delivered energy in full-cell which directly show the performance of the cell and the cell life which is greatest important for the real application.

In the present investigation we aim at determining the energy performance of alkaline direct ethanol fuel cells based on platinum-free electrocatalysts. The possibility of avoiding the use of Pt is related to the alkaline environment where less expensive materials are even effective for both ethanol oxidation and oxygen reduction reaction. On the one hand, palladium has been demonstrated as one of the most effective metals for ethanol electro-oxidation and consequently has been selected as catalytically active phase for the anode [26-29, 32-34, 41, 43-48]. On the other hand, metal–N_4 macrocycles, such as Fe- and Co-macrocycles, are important non-noble catalysts which have attracted attention due to their reasonable activity and remarkable selectivity towards the ORR [68-69]. In addition, this class of electrocatalysts usually shows inertness to ethanol oxidation [68] and thereby restrains the reduction of cell voltage by the ethanol crossover. This can be explained as below: The overall cell voltage for DEFCs can be written as [70-72]:

$$V_{cell} = E_{eq}^0 - \eta_a - \eta_c - \eta_{ohmic} - \eta_{xover} \qquad (3\text{-}1)$$

Where:

E_{eq}^0 denotes the standard electromotive force, which is 1.145V for ethanol.

η_a and η_c are the anode and cathode overpotential, respectively.

η_{ohmic} is the overpotential due to ohmic drop in the system.

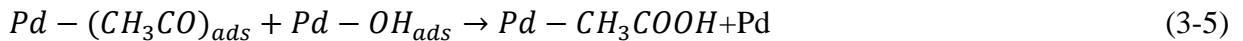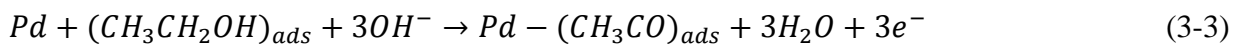η_{xover} is the overpotential due to ethanol crossover through membrane.

Without applying current, η_a, η_c and η_{ohmic} are not existing. Therefore, the open circuit voltage (OCV) can be defined as:

$$OCV = E_{eq}^0 - \eta_{xover} \qquad (3\text{-}2)$$

η_{ohmic} can be reduced dramatically when we use Fe- and Co-macrocycles as cathode catalyst instead of Pt/C or PtRu/C, as Fe- and Co-macrocycles are inert to ethanol oxidation. In consequence, the OCV is much higher. It is worth noting that this kind of catalyst has very low stability in acidic media.

Another important element in favor of the use of DEFCs operating in alkaline media is the fact that Pd oxidizes ethanol to acetate without C-C cleavage for pH higher than 13 [47]. At a first look this is an evident drawback. In fact having a complete oxidation would be beneficial with a better exploitation of the energy content of ethanol. Nevertheless the complete oxidation kinetic is usually very sluggish, ultimate resulting in high anodic over-potential. Partial oxidation of ethanol to acetate is much faster and occurs at high specific current densities even at reasonably low over-potentials [73]. Furthermore C-C cleavage elimination means that no CO is produced, even as an intermediate, avoiding a possible source of poisoning. The advantage of alkaline DEFCs of having together stability, fast kinetic and no potential drops due to ethanol crossover may override the advantages of having complete oxidation in acidic DEFCs.

Pd-based catalysts have been decorated with oxides (CeO_2 [41-42], NiO [41], MnO_2 [41], Co_3O_4 [41], TiO_2 [43], In_2O_3 [44]) to get significant promotion effect on the catalytic activity and stability for EOR. These oxides significantly lower the onset potential for the oxidation reaction with ceria being amongst the most promising ones. The reason for such an enhancement can be easily understood by the mechanisim of EOR on Pd represented as below [45]:

$$Pd + (CH_3CH_2OH)_{ads} + 3OH^- \rightarrow Pd - (CH_3CO)_{ads} + 3H_2O + 3e^- \qquad (3\text{-}3)$$

$$Pd + OH^- \rightarrow Pd - OH_{ads} + e^- \qquad (3\text{-}4)$$

$$Pd - (CH_3CO)_{ads} + Pd - OH_{ads} \rightarrow Pd - CH_3COOH + Pd \qquad (3\text{-}5)$$

Eq. 3-4 is also the rate determining step of ethanol oxidation in alkali [45]. The addition of an alternative oxide such as ceria to Pd promotes the formation of hydroxide on the Pd surface. In a previous investigation we have shown that adding ceria to Pd double the energy efficiency of alkaline DEFCs [42].

Here, we provide a detailed analysis of the energy performance of alkaline DEFCs. The analysis has been performed on DEFCs equipped with nanostructured palladium based anode electrocatalysts, Pd-CeO$_2$/C and Pd/C. At the cathode side, a proprietary FePc-CoPc/C has been employed. The analysis has been focused on the determination of the following three parameters:

1) Maximum power density

2) Delivered energy density

3) Energy efficiency

We believe that such an analysis deserves a special attention. As a matter of fact, the experimental conditions may maximize one of the parameters at the expense of the others. Such peculiarity is analyzed and discussed which provides the first detailed investigation of the energy performance of platinum free alkaline direct ethanol fuel cells.

3.2 Results and discussion

3.2.1 Anode electrocatalyst characterization

Table 3-1. Chemical composition of the investigated electrocatalysts.

Catalyst Element	Pd/C (w.t.%)	Pd-CeO$_2$/C (w.t.%)
C	94.8	62.0
Pd	5.2	4.6
CeO$_2$	-.-	33.4

Inductively coupled plasma atomic emission spectroscopy (ICP-AES) was used to test the chemical composition of Pd/C and Pd-CeO$_2$/C. The data are reported in Table 3-1.

The crystal structure of the Pd/C and Pd-CeO$_2$/C electro-catalysts were investigated by X-ray diffraction (XRD) technique (Figure 3-1). Graphite carbon and metallic palladium are identified in the XRD pattern of both catalysts. Cerium oxide is also observed in Pd-CeO$_2$/C. In addition, no characteristic peaks of palladium oxide are detected. Nevertheless the presence of small amount of amorphous oxides cannot be completely excluded, as generally the surface oxide and hydroxide is amorphous which prevents its identification from XRD. In the Pd-CeO$_2$/C sample the XRD pattern reveals that cerium is present prevalently in form of Ce(IV) oxide, which intensity is much larger as compared to those of carbon and palladium. This can be due to the crystallization of ceria.
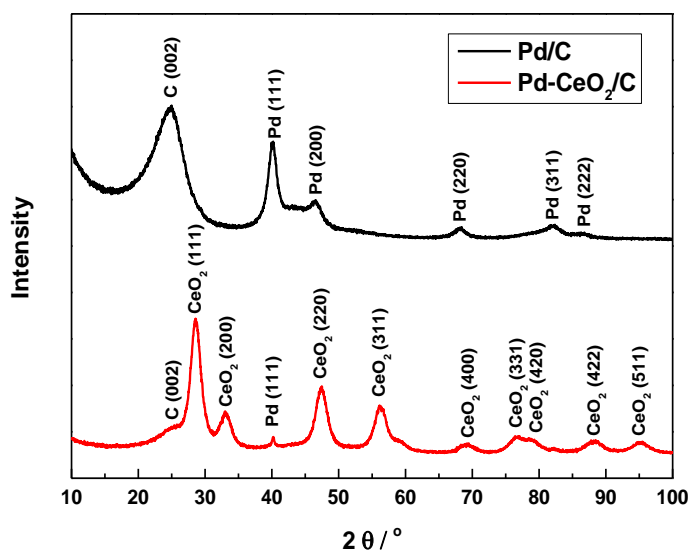

Figure 3-1. Electrocatalyst structure revelation. XRD diffraction patterns of Pd/C and Pd-CeO$_2$/C.

The morphology and structure of Pd/C and Pd-CeO$_2$/C has been demonstrated by TEM investigation. TEM micrographs of the Pd/C reveal palladium particle size ranging between 2 and 10 nm, as shown in Figure 3-2a and 3-2b. Figures 3-2c,d report the TEM image of the Pd-CeO$_2$/C catalyst. They appear that the contrast is not enough to distinguish between cerium oxide and Pd, preventing from a safe determination of the particle size.
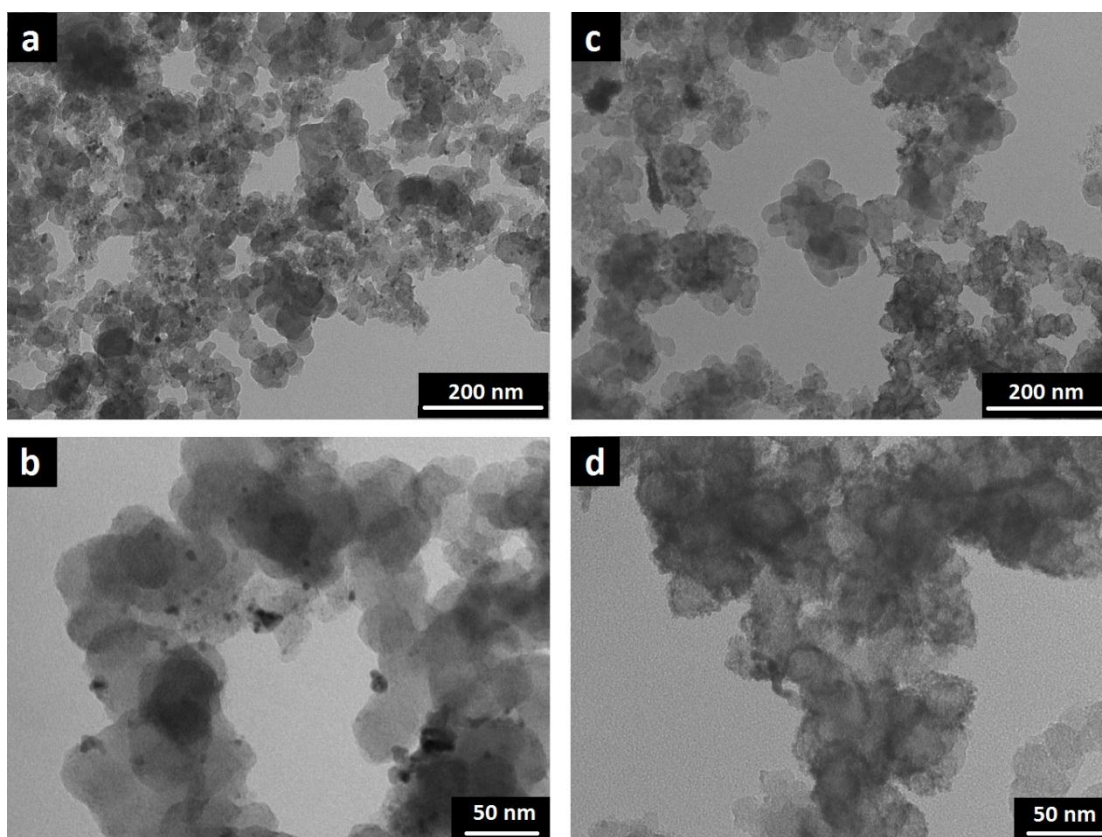
Figure 3-2. Electrocatalyst morphology. Low and high magnification TEM micrographs of a,b) Pd/C and c,d) Pd-CeO$_2$/C.

3.2.2 Half-cell characterization

Cyclic voltammetry studies (Figure 3-3) have been performed on two inks, containing Pd/C and Pd–CeO$_2$/C respectively, in accordance with the catalysts employed in the fuel cell characterization.

Figure 3-3a shows the CV of Pd/C in the 2M KOH electrolyte. At the beginning of positive-going scan, a broad anodic peak (A$_1$) due to oxidation of the adsorbed and absorbed hydrogen is observed. The oxidation of the palladium surface is accompanied with a gentle increase of the current density. At the reversed scan a well-defined cathodic peak C$_1$ at 0.69 V which is related to the reduction of Pd-O [74]. The cathodic peak C$_2$ at 0.20 V can be assigned to the adsorption and absorption of hydrogen. The CV of the Pd–CeO$_2$/C in 2 M KOH shows a

much more evident peak due to hydrogen desorption (A_1 and A_2), as shown in Figure 2-4b. At the reverse scan, the cathodic peak at 0.78 V (C_1) can be assigned to the reduction of Pd-O, whereas the broad cathodic region at 0.22 V (C_2) is attributable to the hydrogen uptake by both Pd and ceria.

The CV experiment performed on the Pd/C electrode in 2 M ethanol + 2 M KOH electrolyte (Figure 3-3c) shows the ethanol oxidation peak (A_1) at 0.78 V with an intensity controlled by the progressive coverage of the electrode surface by Pd-O. At potentials higher than 1 V, the anodic current was analogous to which observed in 2 M KOH alone (Figure 3-3a), indicating that only a negligible fraction of the catalyst sites remain active for ethanol oxidation. The reverse scan shows an anodic peak A_2 occurring at 0.65 V due to the oxidation of ethanol on the catalyst surface free from Pd oxide. The CV of the Pd–CeO_2/C (Figure 3-3d) shows an ethanol oxidation peak culminating at 0.82 V with a current density of 85.5 mA/cm^2 which is higher than that measured from the Pd/C electrode (59.9 mA/cm^2). And furthermore, a lower onset potential for ethanol oxidation can be observed at Pd–CeO_2/C than Pd/C. At a fixed potential of 0.5 V, current densities of 19.7 and 3.5 mA/cm^2 for Pd–CeO_2/C and Pd/C were measured, respectively. In the end, the better performance of the Pd–CeO_2/C catalyst has been assigned to the ability of ceria of promoting the formation of Pd-OH_{ads} species.
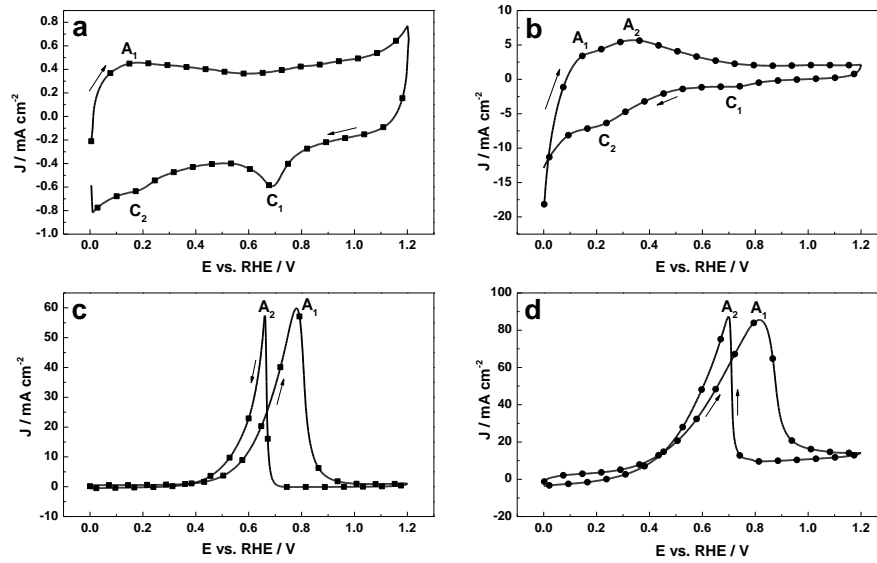
Figure 3-3. Cyclic voltammograms of Pd/C (■) and Pd-CeO$_2$/C (●) in a,b) 2 M KOH and c,d) 2 M Ethanol + 2 M KOH electrolytes.

3.2.3 Air-breathing Direct Ethanol Fuel Cells performance

Table 3-2. Anode electrolyte composition. KOH and Ethanol concentrations.

Ethanol	KOH
2 M	2 M
4 M	2 M
4 M	4 M
4 M	6 M
6 M	6 M

Fuel cell performance has been evaluated with the fuel compositions reported in Table 3-2. Each of the reported fuel compositions has been tested in two DEFCs equipped respectively with the Pd/C and the Pd-CeO$_2$. Performance evaluation has been performed on the basis of polarization and galvanostatic (20 mA cm^{-2}) curves. From polarization we have extracted the

maximum power density, while from galvanostatic data the energy delivered in a single fuel batch and the energy efficiency have been respectively obtained.

Particularly, the delivered energy has been evaluated using Eq. 3-6 which integrating the galvanostatic curve over the time up till a negligible cell potential (0.1 V) is reached.

$$E = I \int V(t)dt \qquad \qquad (3\text{-}6)$$

Where:

I = current flowing through the cell

$V(t)$ = time dependent cell potential

Energy efficiency determination has been done according to Eq. 3-7:

$$\eta_E = \frac{I \int_{t_0}^{t_f} Vdt}{\Delta H^0_{CO_3^{2-}}} \frac{1}{M^F_{TOT}} \qquad \qquad (3\text{-}7)$$

Where:

η_E is the energy efficiency for the ethanol complete oxidation to carbonate;

I is the constant current of the galvanostatic experiment (0.102 A);

$V(t)$ is the transient potential in the constant current discharge experiment;

$\Delta H^0_{CO_3^{2-}}$ represents the enthalpy for ethanol oxidation to carbonate (-1326 kJ/mol);

M^F_{TOT} is the total number moles of fuel in the cell.

It is worthwhile mentioning that such an energy efficiency definition is comprehensive as it accounts for the thermodynamic efficiency, the potential drop of the cell and the faradaic efficiency which is usually lower that 1 as the conversion is usually not complete.

The performance of passive DEFCs with Pd/C and Pd-CeO$_2$/C anode catalysts is shown in Figure 3-4. 2 M Ethanol + 2 M KOH was chosen as the fuel which balances the kinetics and long time performance. At first glance (Figure 3-4a) we may notice that both cells show a high OCV, about 0.9 V. This fact is attributed to the use of the FePc-CoPc/C catalyst at the cathode side which has no activity toward ethanol oxidation [68]. Taking a deeper look, we can

find that all of the potential, current density and power density exhibit a tremendous increase as replacing Pd/C by Pd-CeO$_2$/C as anode catalyst. In particular, at the beginning part of polarization curve, which is much important for potable electronics, the DEFC equipped with Pd-CeO$_2$/C anode shows much higher potential than the Pd/C anode DEFC. This fact can be interpreted recalling CVs which show a much lower onset potential of the ceria promoted electrode as compared to Pd/C.

Figure 3-4b shows the comparison of the galvanostatic curve between Pd/C and Pd-CeO$_2$/C in 2M KOH + 2M ethanol. At a constant current of 20 mA/cm^2, the cell with Pd-CeO$_2$/C exhibits a considerably higher voltage than the cell with Pd/C. As a consequence the energy density released by a single fuel batch is 201.2 J/cm^3 for the system employing the Pd-CeO$_2$/C and 112.3 J/cm^3 for the system using Pd/C. Following from that, the energy efficiency increasing has nearly doubled, from 3.67 to 6.57%. The good performance of Pd-CeO$_2$/C can be ascribed to the ability of ceria of promoting the formation of Pd-OH$_{ads}$ species. As we know, the amount of Pd-OH$_{ads}$ is a crucial parameter determining the electro-oxidation of ethanol, which does not occur on Pd-O [45].
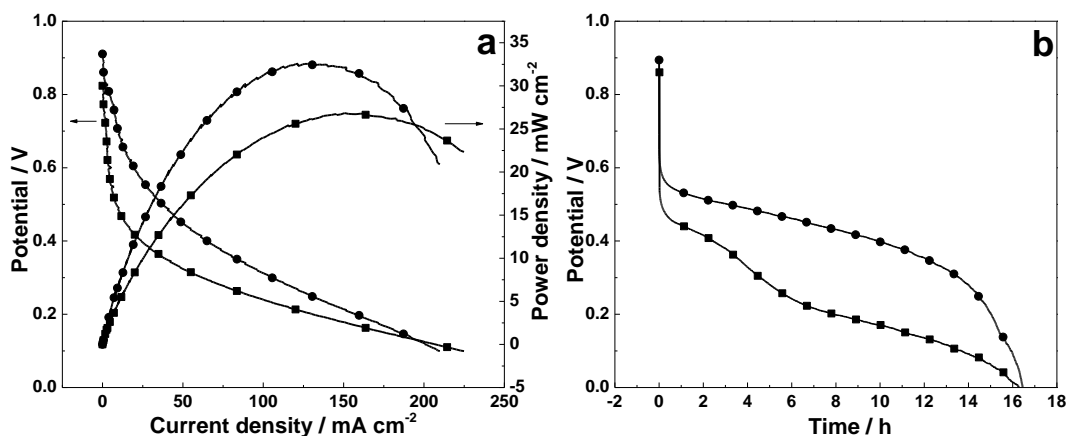

Figure 3-4. Comparision on the performance of the passive DEFCs containing the Pd/C (■) and Pd-CeO$_2$/C (●) anode catalysts and fueled with 2 M Ethanol + 2 M KOH. a) Polarization and power density curves and b) galvanostatic curves with the constant current density of 20 mA/cm^2.

The influence of fuel composition on the polarization is shown in Figure 3-5a. To meet the requirement of long time running of portable power sources, high concentration of ethanol in DEFCs is demanded. Following from that, 2, 4 and 6M ethanol were chosen. At the same time, the same concentration of KOH was added to the electrolyte as the demand of best performance of energy output and energy utilization. Both the limiting current density (Figure 3-5a) and the peak power density (Figure 3-5b) exhibit a tremendous increase when the ethanol concentration is increased from 2 to 4 M. This can be attributed to the fast kinetic of 4 M ethanol. Conversely, the power density drops markedly when the ethanol concentration is increased from 4 to 6 M. A maximum power density of 47.1 mW/cm^2 and a minimum of 18.7 mW/cm^2 are obtained with 4.0 M and 6.0 M ethanol separately, as shown in Figure 3-5b. The poor performance of 6 M ethanol may be due to the high resistance of electrolyte or the high level of ethanol crossover from anode to cathode. It is worth mentioning that the use of FePc-CoPc/C can prevent the reduction of cell voltage by ethanol crossover; even so, we cannot deny the fact of fuel loss by ethanol crossover membrane to cathode.

Galvanostatic curves at 20 mA cm^{-2} follow different trends (Figure 3-5c). The best performance, at least in terms of energy delivered for single cell, has been achieved with the most concentrated electrolyte (6 M ethanol + 6 M KOH). The cell fuelled with 2 M Ethanol + 2 M KOH lasts 16.4 h and releases the energy of 2.41 KJ; while the same cell propelled with 6 M Ethanol and 6 M KOH releases 3.95 J in 39.7 h. Hence we conclude that the long-term performance of the cells may benefit from the use of concentrated electrolyte even if high concentration of ethanol and KOH can be detrimental to get high power density.

Same benefits cannot be obtained at the side of the energy efficiency. Moving from 2 M to 6 M, fuel efficiency drops from 6.57 to 3.31%. This is mainly attributed to the high ethanol adsorption blocking the adsorption of Pd-OH$_{ads}$. In addition, the less use ratio of ethanol caused by the high adsorption of ethanol on Pt surface cannot be eliminating. In addition, the high crossover of fuel at high concentration is also an important reason of the lower energy efficiency at higher ethanol concentration. The energy efficiency of the passive DEFCs decreased with increasing ethanol concentrations consist with the passive DMFCs. In brief, the increase of discharge power by increasing ethanol concentration at the cost of loss of energy efficiency.
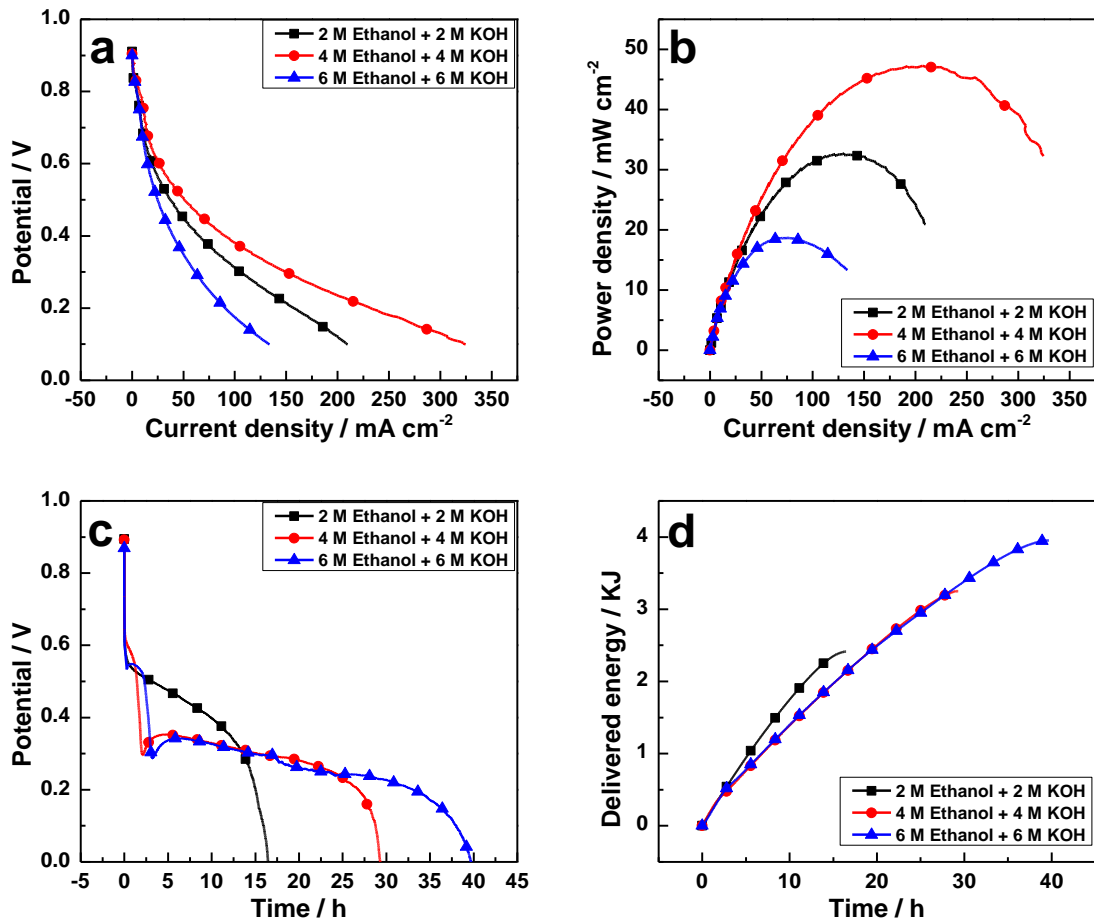
Figure 3-5. Effect of ethanol concentration on the performance of the air-breathing AEM-DEFCs containing the Pd-CeO$_2$/C anode electrocatalyst. a) Polarization curves, b) Power density curves, c) galvanostatic curves and d) discharge energy curves.

It's worth noting that OH$^-$ takes a pivotal role for the oxidation of ethanol. It is well known that in alkaline DEFC, selective oxidation of 1 M ethanol to acetate consumes 5 hydroxyl ions which reported in Eq. 3-8.

$$CH_3CH_2OH + 5OH^- \rightarrow CH_3COO^- + 4H_2O + 4e^- \tag{3-8}$$
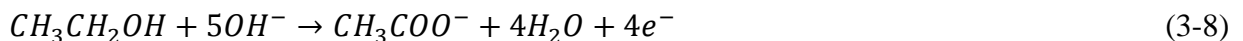
Of particular note is that the oxidation of ethanol results in the formation of acetate instead of acetic acid. Hence a hydroxyl ion, from the fuel rather than cathode reaction product, has to be consumed to balance the charge. A consequence of this is that OH$^-$ has to

be consumed at the same rate of ethanol. Ultimately, alkaline DEFCs operate under a progressive reduction of the pH. At the side of the kinetics, OH$^-$ adsorption plays a crucial role in the oxidation mechanism at low overpotential. Such aspect has been investigated in half-cell experiments. Nevertheless, there is a lack of information of the effect of OH$^-$ concentration on devices' performance. For this reason we have performed a series of experiments (polarization and galvanostatic curves) where ethanol concentration of has been kept constant (4 M) with varying OH$^-$ concentration from 2 to 6 M (Figure 3-6).
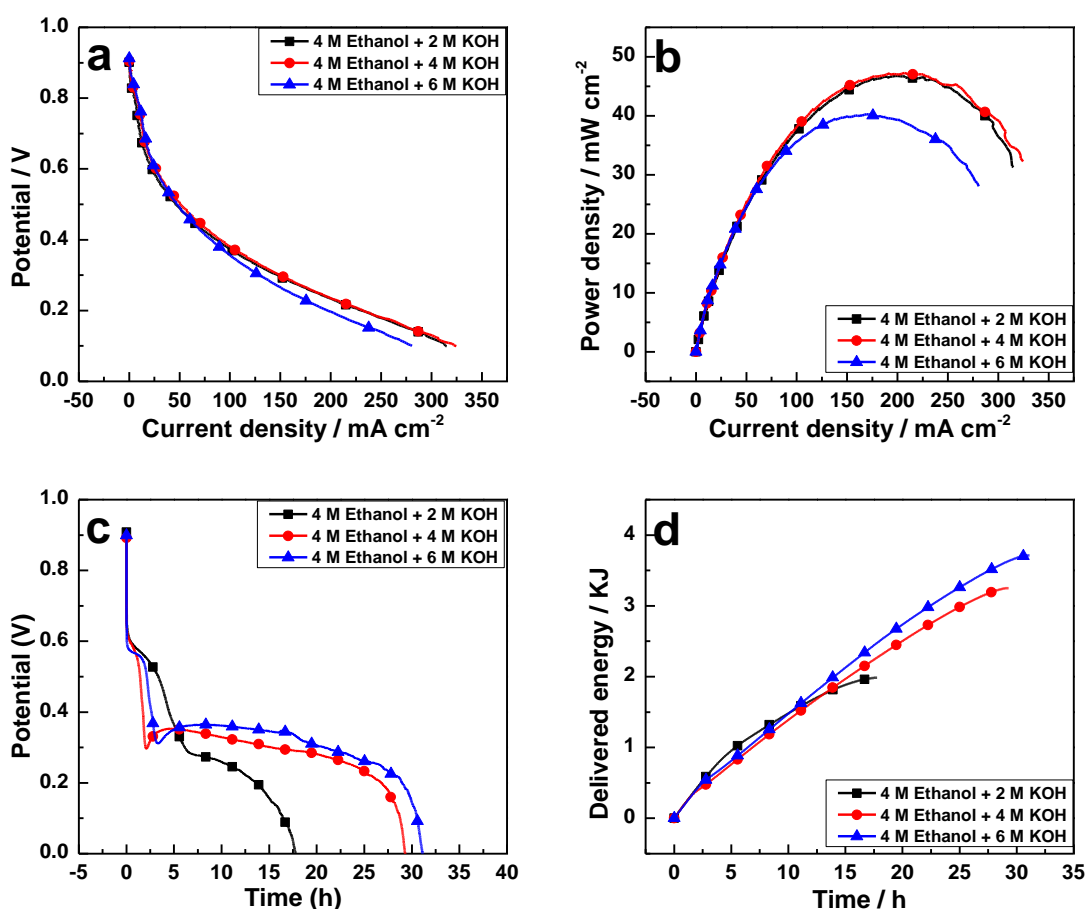

Figure 3-6. Effect of KOH concentration on the performance of the air-breathing AEM-DEFCs containing the Pd-CeO$_2$/C anode electrocatalyst. a) Polarization curves, b) Power density curves, c) galvanostatic curves and d) discharge energy curves.

The highest potential and peak power density during polarization were found in the fuel cell equipped with 4 M KOH. Increasing KOH concentration from 4 to 6 M results in the dramatic decrease of power density, shown in Figure 3-6b. As previously reported, this may be a consequence of the reduction of the electrolyte conductivity at high alkaline concentration.

On the side of the galvanostatic curves, Figure 3-6c shows that duration is benefited as increasing the concentration of KOH. This fact results in a 100% increase in the discharge energy in the cell with 6 M KOH fuel as compared to 2 M KOH. Furthermore, the energy efficiency of the cells jumps from 2.77 (KOH 2 M) to 4.65% (KOH 6 M).

The superiority of high KOH concentration can be explained in two aspects. On the one hand, the first step of the ethanol oxidation reaction on Pd, the dehydrogenation process, can be accelerated at higher OH^- concentration.

$$Pd - H_{abs/ads} + OH^- \rightarrow Pd + H_2O + e^- \tag{3-9}$$

On the other hand, the increasing of the OH^- concentration leads to a higher coverage of the reactive $Pd\text{-}OH_{ads}$, which facilitates the ethanol oxidation reaction by the removal of the adsorbed ethanol. The equation, which is the rate-determining step, is shown in Eq. 3-4.

Figure 3-7 shows an overview performance of all the cells equipped with the two different anode electro-catalysts and fueled with different electrolytes. Three critically important parameters, peak power density (Fig. 3-7a), discharge energy density (Fig. 3-7b) and energy efficiency (Fig. 3-7c) have been reported as a function of the fuel composition and the anode material. These three parameters show completely different trends indicating that care should be taken when selecting the factor for performance assessing. Highest power density can be gotten at suitable concentration of ethanol and KOH. For some application, such as military, the power density is the overriding factor. But for the application as portable power source, standby or remote power, discharge capacity is the most relevant factor. Fig. 3-7b shows that high concentration of ethanol and KOH is required for high discharge energy. However, high concentration of fuel results in low energy efficiency.

We have observed that the performance of $Pd\text{-}CeO_2/C$ is better than Pd/C for all the reported experiments irrespectively of the fuel composition. We would also like to mention

that energy efficiency are still rather low indicating that much more efforts should be made on the developing electro-catalysts with high catalytic activity and the better design of cell, etc.
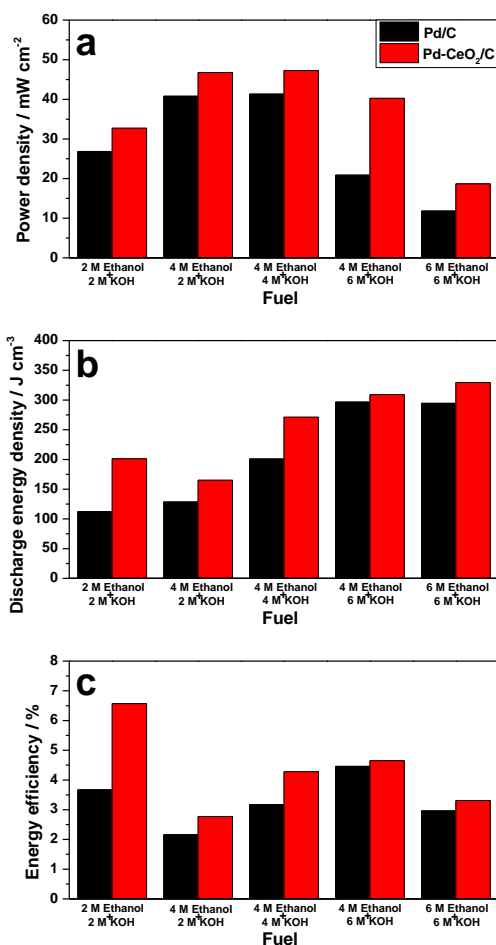

Figure 3-7. Maximum power density, discharge energy density and energy efficiency of the passive DEFCs fueled with ethanol and KOH at different concentrations.

3.2.4 Micro Air-breathing Direct Ethanol Fuel Cells Durability

As the potential of DEFCs for portable devices application, the assessment of micro DEFCs performance, especially stability, is imperative. A micro air-breathing DEFC with 1 cm^2 MEA (which is composed of Pd-CeO$_2$/C as anode, FePc-CoPc/C as cathode, and Tokuyama A201 as anion exchange membrane) was assembled. Longest duration fuel, 6 M Ethanol plus 6 M KOH, was chosen to fuel the device. The constant current density, 1 mA/cm^2, was selected to test the stability of our micro cell. As seen from Figure 3-8, the cell has run for 87 days with a

potential drop of 3 mV/day. After 2000 hours, the cell still ran at 380 mV. The delivered energy during 2000 hours is 3.89 kW while the power density moved from 0.63 µW/cm^2 at the beginning to 0.38 µW/cm^2 at the end. The oscillation of the curve is attributed to the temperature variation during the day and night and during the weekend which became more pronounced in the winter season.
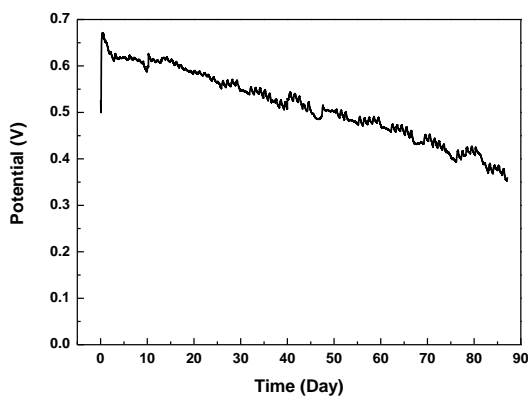

Figure 3-8. Stability test at 1 mA/cm^2 of micro air-breathing DEFC fueled with 6 M ethanol and 6 M KOH.

3.3 Conclusions

We have investigated platinum-free alkaline direct ethanol fuel cells fuelled with a variety of electrolytes in order to determine how the fuel composition affects maximum power density, discharge energy density and energy efficiency. We have found that these parameters showed a different dependence on the fuel composition. Particularly we have noticed that in order to increase the maximum power density appropriate alkaline concentration should be chosen. The best power density has been obtained with a balanced electrolyte containing 4 M ethanol and 4 M KOH. An increase in KOH concentration results in a dramatic decrease of the maximum power density that occurs independently of ethanol concentration. Unlike maximum power density, discharge energy is benefited from increasing in both KOH and ethanol concentration.

We have also found that at even ethanol concentration (4 M) the increase in the KOH concentration produces an increase in the energy efficiency. On the contrary, energy efficiency decreased with increasing the ethanol concentration.

The DEFCs equipped with the Pd/C and Pd-CeO$_2$/C show the same trend with respect to all the different electrolytes. Nevertheless, the performance of the Pd-CeO$_2$/C is better as compared to Pd/C. This is attributed to the kinetics of the anodic reaction. Ethanol oxidation reaction requires the adsorption of hydroxyl ions at the palladium surface. This reaction is the rate determining step at low over-potential. The addition of ceria to Pd speeds up such step through the primary oxide spillover. According to this mechanism the hydroxide is first formed at the surface of ceria and then quickly transferred to the surface of Pd. This interaction requires the two species to be in contact in order to allow the surface diffusion.

As the different effect of electrolyte composition on DEFCs parameters, optimization of performance varies with specific practical applications. Furthermore energy efficiency are still rather low (6.57% at maximum in this study), suggesting that much more efforts should be made on the developing electro-catalysts with high catalytic activity.

In the end the performance of micro direct ethanol fuel cells was evaluated. Membrane electrode assembly with a size of 1 cm^2 has been test under constant current of 1 mA/cm^2 for 2000 hours with a slowly gradual potential drop. As thus the potential of DEFCs to provide power to portable devices has been further confirmed.

4. Non-platinum Electrocatalysts for Air-breathing Direct Formate Fuel Cells

4.1 Introduction

Polymer electrolyte membrane fuel cells, in particular, the direct liquid fuel cells (DLFCs) are viewed as viable candidates to replace batteries in portable power devices. Formic acid has recently attracted attention as an alternative fuel for DLFCs due to their considerably advantages over methanol and ethanol. The rate of formic acid cross-over is two orders of magnitude smaller than that of methanol, allowing for high fuel concentrations and thinner electrolytes [75-76]. The formic acid also has a higher theoretical open circuit voltage (OCV), as shown by Eq. 4-1,2,3, than either hydrogen or direct methanol fuel cell. The chemical reactions for the direct formic acid fuel cells (DFAFCs) system can be expressed as follows:

Anode: $HCOOH \rightarrow CO_2 + 2H^+ + 2e^-$ $E^0_{anode} = -0.22\ V$ (4-1)

Cathode: $\frac{1}{2}O_2 + 2H^+ + 2e^- \rightarrow H_2O$ $E^0_{cathode} = 1.23\ V$ (4-2)

Overall: $HCOOH + \frac{1}{2}O_2 \rightarrow CO_2 + H_2O$ $E^0 = 1.45\ V$ (4-3)

In addition, formic acid is a naturally-occurring substance and a relatively benign chemical that is used as a food additive at lower concentrations. As a result, direct formic acid fuel cells are expected to be among the first commercial small fuel cells to appear on the consumer market [77].

A critical obstacle that limits the wide application of DFAFCs is the cost of the system, because a considerable amount of Pt-based catalysts at both the anode and cathode is required [78-80]. Unlike in acid media, the kinetics of both the formate oxidation and oxygen reduction reaction in alkaline media is much faster and allows the use of non-precious metal catalysts to reduce the cost of the fuel cells. On the one hand, palladium has been demonstrated as one of the most effective metals for small organic molecules electro-oxidation and consequently has been selected as catalytically active phase for the anode [27, 32, 81]. On the other hand, metal–

N_4 macrocycles, such as Fe- and Co-macrocycles, are important non-noble catalysts which have attracted attention due to their reasonable activity and remarkable selectivity towards the ORR [68-69]. In addition, this class of catalysts usually shows inertness to organic molecules oxidation [68] and thereby restrains the reduction of cell voltage by the fuel crossover. The effectiveness of alkaline direct formate fuel cells (DFFCs) is also related to the use of dedicated anion exchange polymer electrolyte such as those produced by Tokuyama.

For the above mentioned reasons the assessment of DFFCs appears to be an issue of importance. However, relatively little work has been reported about the evaluation of DFFCs especially with non-platinum electrocatalysts. Particularly worth mentioning is that the power density and energy efficiency of DEFCs, as a potential portable electronic device, is in badly need of investigation. High energy efficiency and high power density fuel cells are vitally needed for portable power source applications to minimize fuel consumption, weight, volume and capital cost of power plants [67]. In some extent the energy efficiency is more critical than the power density because the weight and volume of the energy storage systems are crucial important in portable power source.

In this paper we present the comprehensive assessment of passive air-breathing DFFCs, in which fuel and oxidant are passively delivered without any moving parts such as pumps, fans, or blowers. The analysis has been performed on DFFCs equipped with nanostructured palladium based anode catalysts, Pd/C. At the cathode a proprietary FePc-CoPc/C, cobalt and iron complexes with phthalocyanines (Pc) supported on carbon black, has been employed. The analysis has been focused on the determination of the following parameters: maximum power density, delivered energy, faradic efficiency, and energy efficiency. We believe that such an analysis deserves a special attention.

4.2 Results and discussion

4.2.1 Electrocatalyst characterization

Transmission electron microscopy (TEM) images of the Pd/C electrocatalyst are shown in Figure 4-1a. The Pd nanoparticles are generally well distributed over the carbon support and are of an even size distribution with most of the particles below 10 nm in diameter (mean 3.2 ± 0.8 nm). The morphology of the as-synthesized FePc-CoPc/C was observed by TEM (Figure 4-1b). All Ketjen Blacks appear as nanoparticles with a diameter of about 30 nm.

Most of the compartments were empty which indicates that neither metals nor Fe-Co alloy were formed.
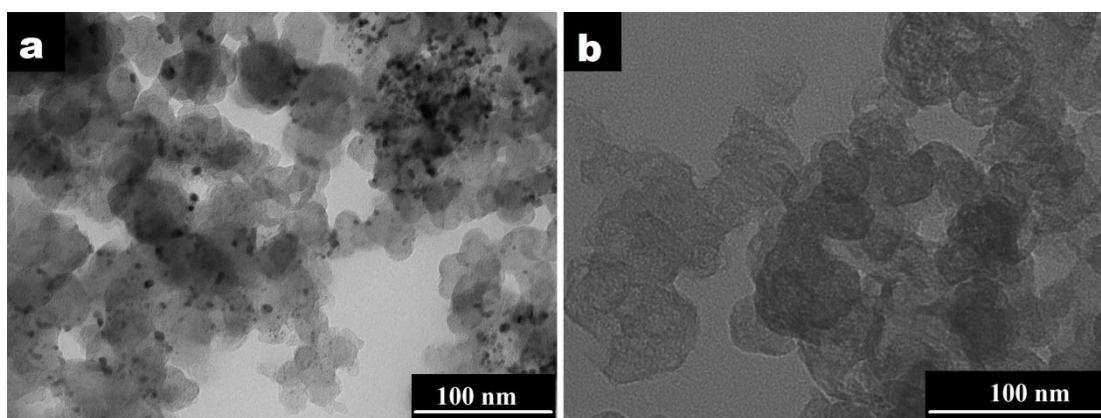

Figure 4-1. Representative TEM micrograms of a) Pd/C and b) FePc-CoPc/C.

Information about the nature of the structure of the investigated electrocatalysts has been obtained by powder X-ray diffraction (XRD) (Figure 4-2). Pd nanoparticles supported on carbon black exhibit the characteristic XRD pattern of a face-centered-cubic (fcc) lattice structure as shown in Fig. 4-2a. The strong diffraction peaks at the Bragg angles of 40.16°, 46.54°, 68.31°, 82.05° and 86.83° are respectively assigned to the (1 1 1), (2 0 0), (2 2 0), (311) and (222) Bragg reflections of metallic Pd. The Sherrer equation applied to the Pd (1 1 1) reflection has returned an average crystallite size of 6.1 nm. Apart from the broad peak attributed to C (0 0 2) no peaks other than those of metallic Pd have been detected.

The XRD of FePc–CoPc/C shows the typical pattern of the carbon support with two very broad diffraction peaks centered at ca. 25.31 and 43.38°, which are attributed to the presence of an amorphous phase of the MPc species [69]. No metallic particles were generated on the carbon surface.
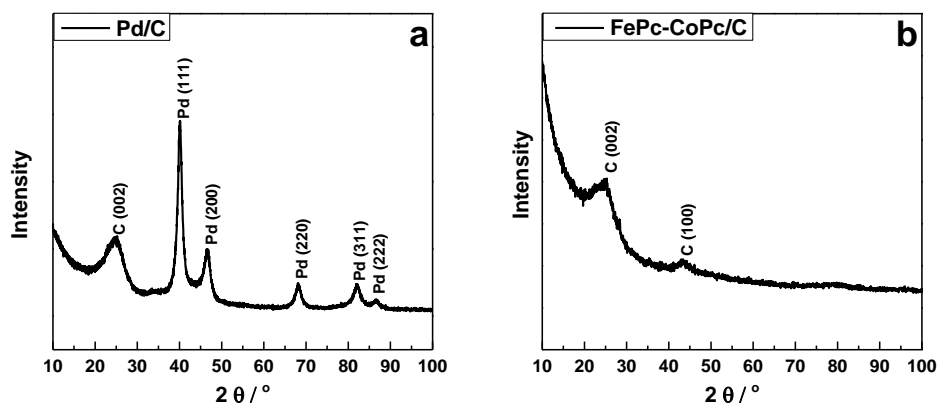
Figure 4-2. Powder XRD diffraction patterns of a) Pd/C and b) FePc-CoPc/C.

4.2.2 Half-cell characterization

Cyclic voltammetry (CV) of the Pd/C was undertaken in N_2-saturated electrolyte at room temperature. The CV of a single Pd/C electrode in 2 M KOH is shown in Figure 4-3. The EASA of Pd in the single electrode was calculated using the charge associated with the reduction peak of the first monolayer of PdO [74]. A value of 51.6 m^2/g_{Pd} was obtained.
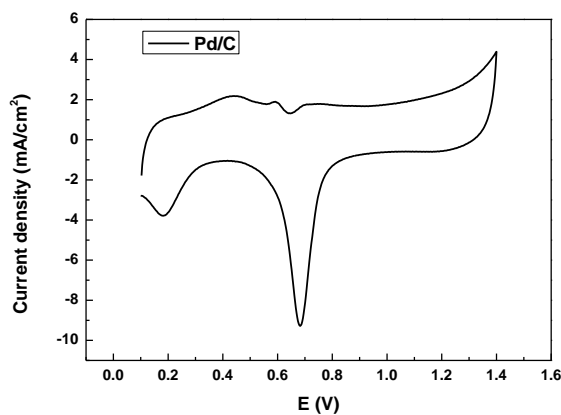

Figure 4-3. Cyclic voltammograms of Pd/C in 2 M KOH electrolyte with a scan rate of 50 mV/s.
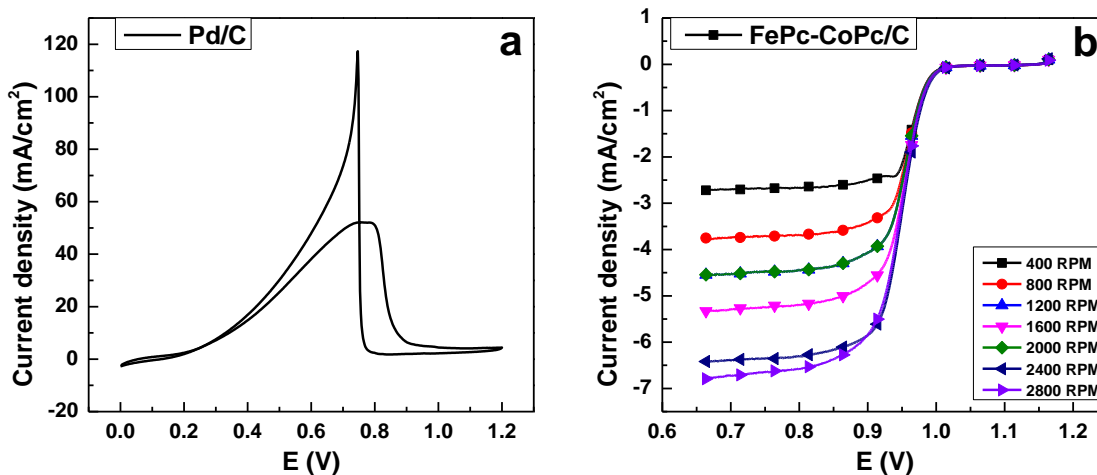
Figure 4-4. a) Cyclic voltammograms of Pd/C in 2 M Ethanol + 2 M KOH with a scan rate of 50 mV/s; b) Rotating-disk voltammograms of FePc-CoPc/C electrocatalysts in O_2-saturated 0.1 M KOH with a scan rate of 5 mV/s.

The activity of Pd/C toward formate oxidation reaction has been determined by acquiring CV in 2M KOH plus 2M formate electrolyte. The electrolyte has been selected for the fact of having been practically exploited in real anion exchange membrane fuel cells as well as in electrochemical reforming devices [42, 82-83].

Fig. 4-4a shows the formate oxidation peak at 0.74 V with an intensity controlled by the progressive coverage of the electrode surface by Pd-O. At potentials higher than 1 V, the anodic current was comparable to that observed for the 2 M KOH alone (Figure 4-3), indicating that only a negligible fraction of the electrocatalyst sites remains active for formate oxidation. The reverse scan shows a further anodic peak occurring at 0.76 V due to the oxidation of fresh formate on the electrocatalyst surface freed from Pd oxide.

The electrochemical activity of FePc–CoPc/C for the oxygen reduction reaction (ORR) was investigated by linear sweep voltammetry at room temperature using a rotating disc electrode (RDE). The polarization curves are shown in Figure 4-4b. The experimentally determined limiting currents were within the ±10% limit theoretically established by the Levich equation [84]. From the data reported in Figure 4-4b, one may readily realize that the FePc-CoPc/C electrocatalyst shows superior ORR activity which is comparable with the Pt-based electrocatalysts [69]. A superior performance of Fe and Co electrocatalysts, as compared

to Pt, for the ORR has been previously observed in alkaline media [68-69]. As pointed out by literatures, nitrogen functionalities in the carbon support may have a role in the ORR activity in alkaline media [85-86]. Therefore, we cannot rule out that the functionalized Ketjen Black may contribute to the observed ORR activity.

4.2.3 Air-breathing Direct Formate Fuel Cells performance

The fuel cell performance has been evaluated in single cell fed with formate and KOH solution. Different fuel compositions, reported in Table 4-1, have been employed.

Table 4-1. Anode electrolyte composition. Formate and KOH concentrations.

Anode electrolyte composition	
Formate	KOH
2 M	2 M
3 M	3 M
4 M	2 M
4 M	4 M
4 M	6 M
5 M	5 M
6 M	6 M

Performance evaluation has been performed on the basis of potentiodynamic and galvanostatic (20 mA cm^{-2}) curves. From potentiodynamic we have extracted the maximum power density, while from galvanostatic data the delivered energy, faradic efficiency and energy efficiency have been respectively obtained.

The delivered energy has been evaluated applying equation 4-4 by integrating the galvanostatic curve over the time up till a negligible cell potential was reached.

$$E = I \int_0^t V(t)dt \tag{4-4}$$

Where:

I is constant current flowing through the cell, 102 mA;

V(t) is transient cell voltage.

To investigate the fuel utilization, we define the Faradic efficiency as:

$$\eta_F = \frac{discharge\ capacity}{theoretical\ discharge\ capacity} = \frac{\int_0^t I(t)dt}{2C_f V_F F} \tag{4-5}$$

Where:

I(t) is the transient discharge current;

C_F is the initial formate concentration;

V_F is the formate solution volume;

F is the Faraday constant.

The Faradic efficiency defined in Eq. 4-5 indicates the ratio of the actual discharging capacity to the theoretical discharging capacity.

Energy efficiency determination has been done according to equation 4-6:

$$\eta_E = \frac{E}{-MV\Delta H^0} \tag{4-6}$$

Where:

E is the delivered energy from the single cell;

M is molarity of formate in the cell;

V is the volume of formate fuel;

ΔH^0 represents the enthalpy change of formate oxidation reaction as shown by equation 4-7.

$$HCOOK + \frac{1}{2}O_2 + KOH \rightarrow K_2CO_3 + H_2O \tag{4-7}$$

The relevant standard enthalpy of formation of chemicals in Eq. 4-7 is shown in Table 4-2. Then the enthalpy change of formate oxidation reaction can be figured out as -254.14 KJ/mol.

Table 4-2. Standard enthalpy of formation of chemicals in Eq. 4-7 (at 25 °C, 298 K).

Formula	Phase	$\Delta_f H^0$ (KJ/mol)
HCOOK	aqueous	-679.9
O_2	gaseous	0
KOH	aqueous	-482.4
K_2CO_3	aqueous	-1130.6
H_2O	liquid	285.8

It is worthwhile mentioning that such an energy efficiency definition is comprehensive as it accounts for the thermodynamic efficiency, the potential drop of the cell and the faradaic efficiency which is usually lower that 1 as the conversion is usually not complete.

The influence of formate concentration was investigated through polarization and constant current test, shown in Figure 4-5. The corresponding detailed parameters were collected in Table 4-3.

To meet the requirement of long time running of portable power sources, high concentration of formate in DFFCs is demanded. Following from that, 2, 3, 4, 5 and 6 M formate were chosen. At the same time, the same concentration of KOH with formate was added to the electrolyte as the demand of best performance of energy output and energy utilization [45, 47].
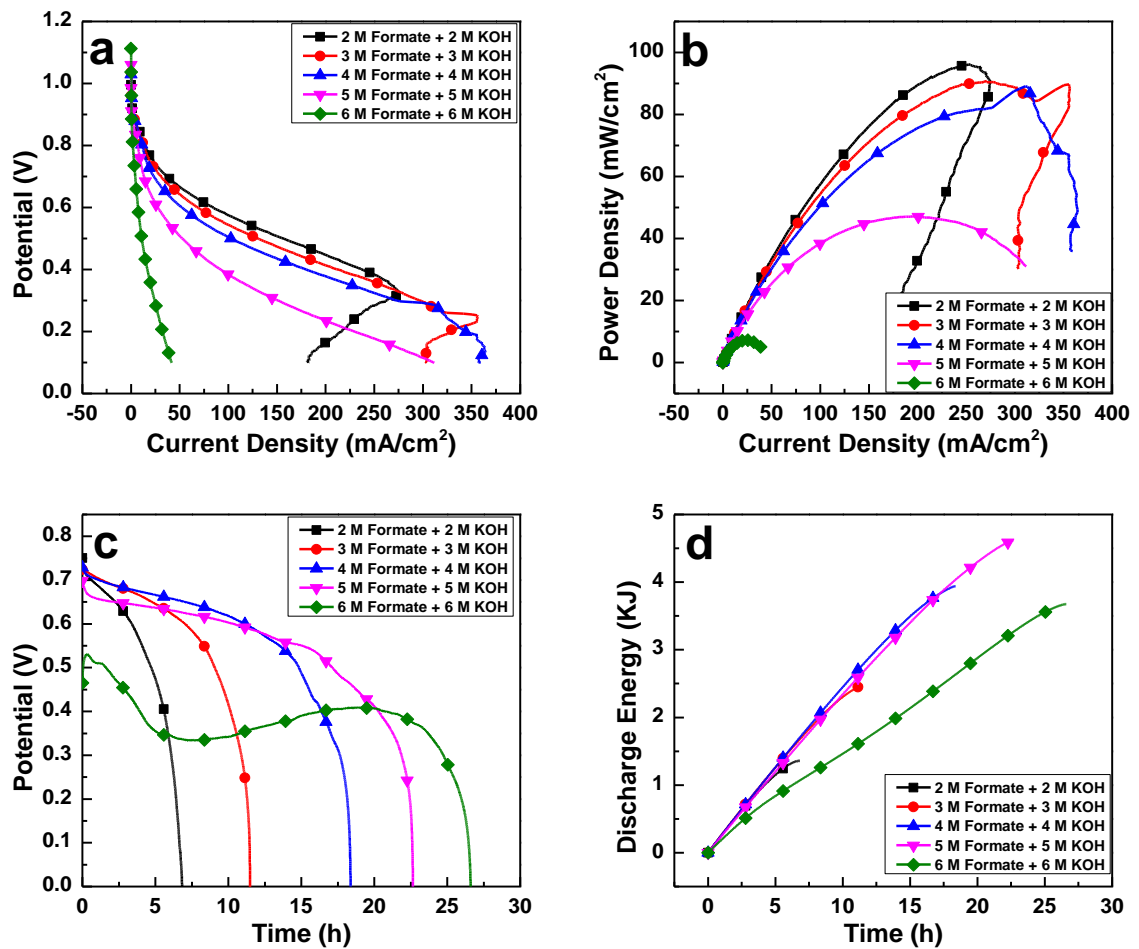
Figure 4-5. Effect of formate concentration on the performance of the air-breathing direct formate fuel cell. a) Polarization curves, b) Power density curves, c) galvanostatic curves and d) discharge energy curves.

Table 4-3. The performance of the air-breathing DFFC with different electrolytes.

	Electrolyte				
	2 M Formate 2 M KOH	3 M Formate 3 M KOH	4 M Formate 4 M KOH	5 M Formate 5 M KOH	6 M Formate 6 M KOH
Open Circuit Voltage (V)	1.00	1.04	1.03	1.06	1.13
Current density at 0.5 V (mA/cm^2)	154.80	129.26	102.71	52.70	10.96
Maximum Power Density (mW/cm^2)	96.33	90.84	89.07	47.21	7.25
Discharge Energy (KJ)	1.36	2.47	3.94	4.61	3.68
Faradic Efficiency (%)	53.15	59.59	71.42	70.51	68.98
Energy Efficiency (%)	22.30	27.00	32.30	30.23	20.11

In the present research a method of constant current discharge is employed to examine the long-term performance. The influence of formate concentration for constant current discharge and the relevant discharge energy are shown in Figure 4-5c and 4-5d respectively.

Both the duration and discharge energy density increased more than three times as increasing the concentration of ethanol from 2 to 5 M. Differently, single cell fueled with 6 M formate has delivered less energy compared to the cell with 6 M formate, which is due to the lower potential of 6 M cell.

Fuel utilization factor has been calculated by equation 4-5. The corresponding results are shown in Table 3. Different from the DMFCs and DEFCs, the faradic efficiency of DFFCs increased as increasing the fuel concentration from 2 to 4 M and decreased from 4 to 6 M [64, 87].

Particularly, the efficiency of the DFFC, fueled with 4 M Formate and 4 M KOH, reaches up to 71.42%, which is much higher than the highest utilization of DMFC, 52.0% [64].

In addition, energy efficiency of air-breathing DFFCs has been calculated by equation 4-6. The highest energy efficiency was obtained at the cell with 4 M Formate plus 4 M KOH electrolyte. Surprisingly, the number, 32.3%, is pretty higher than the DMFCs (6.8-15.4%) [64] and DEFCs (6.0%) [42].
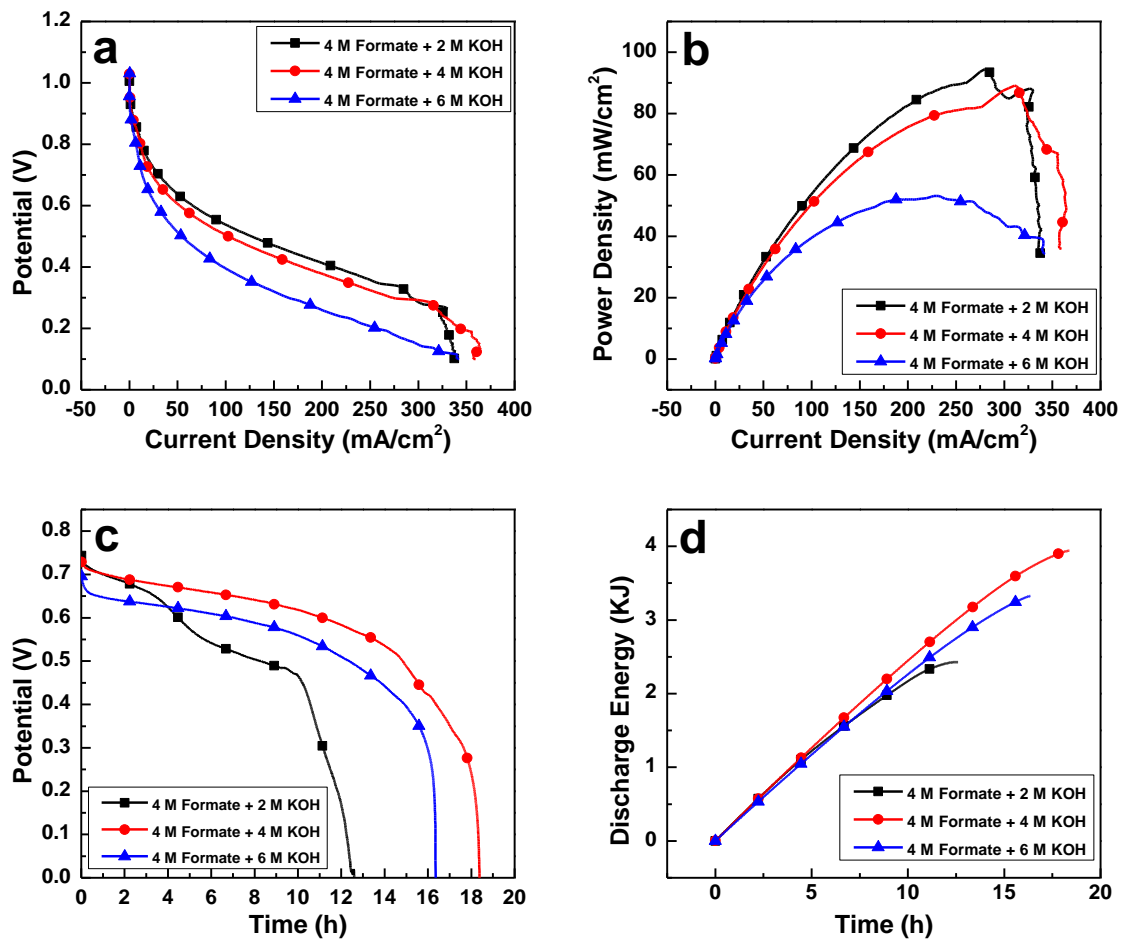

Figure 4-6. Effect of KOH concentration on the performance of the air-breathing direct formate fuel cell. a) Polarization curves, b) Power density curves, c) galvanostatic curves and d) discharge energy curves.

Table 4-4. The performance of the air-breathing DFFC with different electrolytes.

	Electrolyte		
	4 M Formate 2 M KOH	4 M Formate 4 M KOH	4 M Formate 6 M KOH
Open Circuit Voltage (V)	1.01	1.03	1.03
Current density at 0.5 V (mA/cm^2)	125.25	102.71	54.26
Maximum Power Density (mW/cm^2)	94.40	89.07	53.16
Discharge Energy (KJ)	2.43	3.94	3.33
Faradic Efficiency (%)	49.01	71.42	63.59
Energy Efficiency (%)	19.92	32.30	27.30

It has been recognized that OH^- has a fundamental role in the oxidation of formate. To understand better, it is necessary to recall the anode and cathode reaction in DFFCs.

$$COOH^- + 3OH^- \rightarrow CO_3^{2-} + 2H_2O + 2e^- \tag{4-8}$$

$$\frac{1}{2}O_2 + H_2O + 2e^- \rightarrow 2OH^- \tag{4-9}$$

The formation of carbonate consumes 3 hydroxyl ions at the anode while only 2 hydroxyl ions are formed from cathode. Hence a hydroxyl ion has to be consumed to balance the charge. A consequence is that as formate is consumed during the experiment, OH^- is consumed at the same rate. Ultimately alkaline DFFCs operate under a constant and progressive reduction of the pH. On the side of the kinetic, OH^- adsorption plays a crucial role in the oxidation mechanism so much that at low overpotential the formation of adsorbed hydroxyl is the rate determining step. For this reason we have performed a series of experiments where ethanol concentration of has been kept constant (4 M) varying OH^- concentration between 2 and 6 M (Figure 4-6). The relevant parameters were collected in Table 4-4.

The peak power density has exhibited its maximum when the KOH concentration is 2 M (94.40 mW/cm^2). When the concentration is increased from 2 to 6 M the power density drops markedly leading to a peak power density of (53.16 mW/cm^2). This can be ascribed to the conductivity of KOH electrolytes but kinetic reasons such as very strong OH$^-$ adsorption could also concur to the performance degradation. Galvanostatic curves at 20 mA cm^{-2} follow different trends. The best performance has been achieved with the middle concentrated KOH (4M). The cell fuelled with different concentrations of KOH 2.43, 3.94, 3.33 KJ, separately. The trend of KOH concentrations works same on the faradic efficiency and energy efficiency. Hence we conclude that the cell performance benefits with the concentration of formate and KOH at the same level.

4.3 Conclusions

Pd/C was synthesized with an even size of 3.2 ± 0.8 nm. Iron and cobalt phthalocyanines on Ketjen Black were synthesized giving materials containing arrays of single metal ions coordinated by four nitrogen atoms (M-N$_4$ units). Both electrocatalysts were characterized by XRD, TEM, and cyclic voltammetry in half cell, polarization and constant current test in passive air-breathing direct formate fuel cells.

The polarization investigation shows that the assembled DFFC shows high current density, high OCV and high power density. Particularly, the high OCV, ≥ 1.0 V, is mainly attributed to the higher theoretical electromotive force of DFFCs. And the using of FePc-CoPc/C as cathode electrocatalyst to restrain the reduction of cell voltage by fuel crossover is another key factor. In addition, the highest power density, 96.33 mW/cm^2, was obtained which is much higher than the similar equipped air-breathing direct methanol fuel cells and direct ethanol fuel cells. In particular, this maximum power density is relatively higher than the passive DFCFCs but using much inexpensive electrocatalysts instead of Pt-based electrocatalysts. Furthermore, the energy efficiency of DFFCs is more than 1 time higher than DMFCs and 4 times higher than DEFCs.

We have also examined this non-platinum direct formate fuel cells fuelled with a variety of electrolytes in order to determine how the fuel composition affects OCV, maximum power density, discharge energy, faradic efficiency and energy efficiency. We have found that those parameters show a different dependence on the fuel composition. The highest OCV was

gotten in the cell with 6 M formate plus 6 M KOH. We have found that both the current density and power density exhibit a tremendous decrease as increasing the fuel concentration. This is mainly due to the high ohmic losses at high fuel concentrations. The best current density and power density were obtained in the cell fueled with 2 M Formate plus 2 M KOH, while the highest delivered energy, fuel utilization and energy efficiency have been found in the single cell equipped with 4 M formate plus 4 M KOH. The parameters show completely different trends indicating that care should be taken when selecting the specific factor for performance assessing. The targeted application should always kept in mind in order to optimize the fuel composition.

Combining the superiority of low crossover, high open circuit voltage, high current density, high power density, high fuel utilization, and high energy efficiency, DFFCs are expected to be among the first commercial fuel cells as portable devices.

5. Electrochemical Growth of Palladium Nanostructures for Enhanced Alcohols Oxidation

5.1 Introduction

5.1.1 Crystal structure affects catalytic activity

The catalytic action of the solid surface involves the adsorption of the reactant molecules at certain sites where bond breaking (C—H, C—C and H—H) occurs followed by rearrangement of the adsorbed reaction intermediate. After that, the product molecule will be desorbed from the catalyst surface so that the process could be constantly repeated [88].

The chemically active solid surface is structurally heterogeneous and may be viewed as shown by the model in Fig. 5-1, which illustrates the names for the atomic positions and point defects on a surface for a simple cubic lattice.
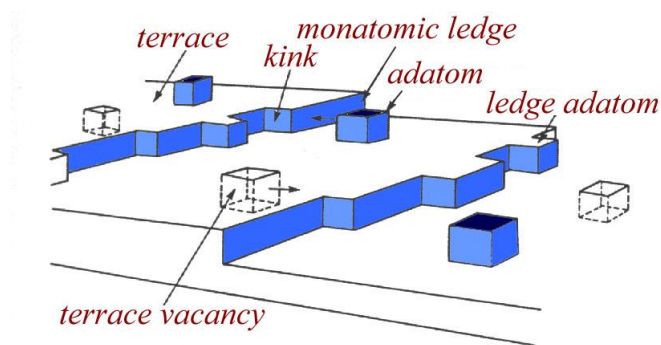

Figure 5-1. The names for the various atomic positions.

There are atoms in terraces surrounded by the largest numbers of nearest neighbors. There are surface irregularities, steps and kinks, in which atoms have less nearest neighbors. Among them, the atoms with less neighbors, such as steps and kinks, on catalyst surfaces are active in breaking C—H, C—C and H—H bonds.

5.1.2 High index facets

High-index facets, which are denoted by a set of Miller indices with at least one index greater than unity, are considered as one kind of open structures [89]. The different types of polyhedron and their surface facets is shown in Fig. 5-2. At the three vertices are polyhedrons enclosed by three low-index facets: octahedron with 8 (111) facets, cube with 6 (100) facets, and rhombic dodecahedron with 12 (110) facets. Among them, the (100) and (111) planes have closely packed surface, whereas the (110) planes have stepped atoms. The polyhedrons in three sidelines and interior of the triangle represent four types of polyhedrons, tetrahexahedra (THH), trapezohedra (TPH), trisoctahedra (TOH), and hexoctahedra (HOH), with high indexed facets. Each polyhedron type is associated with a specific class of high-index facets. THH are bounded by 24 (hk0) (h > k > 0) facets, TPH by 24 (hkk) (h > k > 0), TOH by 24 (hhl) (h > l > 0), and HOH by 48 (hkl) (h > k > l > 0) facets.
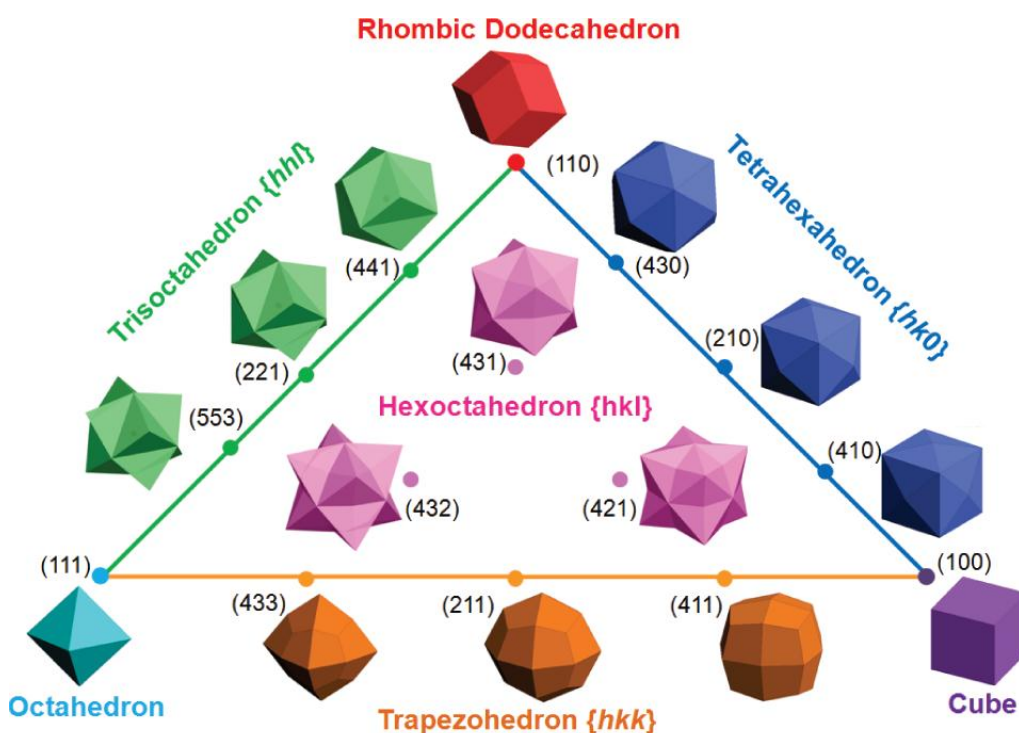

Figure 5-2. Triangular diagram of polyhedral fcc metal bounded by different crystallographic facets [90].

These facets possess a high density of low-coordinated atoms such as steps, edges, and kinks, serving as large amount active sites. As a result, noble metal catalysts with high-index

facets usually exhibit significantly enhanced activities compared with those close-packed low-index facets. Consequently, high-indexed noble metal nanocrystals are expected to possibly serve as a new generation of catalysts. The synthesis of nanocrystals enclosed by high-index facets remains a challenge because of high index facets normally grow faster during a growth stage and thus are preferentially eliminated to minimize total surface energies of the final nanocrystals. Apparently, it is a challenge to produce high-indexed noble metal nanocrystal.

During all kinds of synthetic methods of nanocrystals enclosed by high-index facets, the square-wave potential (SWP) treatment shows unique advantages of simple and effective [29, 34, 91]. The electro-oxidation of metal and reduction of its surface oxide lead to changes in the surface morphology and roughness. Repetitive oxide growth and reduction increase the electrode's real surface area and also the structure, which include high index facets, through the formation of surface defects, such as clusters of ad-atoms, vacancies, rearrangement of atoms at grain boundaries, etc. These morphological changes translate into modified electrocatalytic properties of the metal/electrolyte interphase [74].

5.1.3 Anion exchange membrane direct alcohol fuel cells

Direct alcohol fuel cells are devices that the free energy of alcohols can be converted into electrical energy, with contemporaneous release of high added-value products. A crucial role for achieving this goal is played by the anode electrocatalysts which must promote the partial oxidation of renewable alcohols, such as ethanol, glycerol, ethylene glycol, to carboxylic compounds, preferentially in a selective way and with fast kinetics. It is known that alcohol partial oxidation is particularly effective in alkaline electrolyte. Table 5-1 summarizes the electrooxidation of alcohols in alkaline medium studied in this work.

Table 5-1. Electrochemical oxidation of alcohols in alkali.

Alcohol	Reaction Equation	E^0 (vs. RHE)	Energy Density (Wh/kg)
Ethanol	$CH_3CH_2OH + 2OH^- \rightarrow CH_3CHO + 2H_2O + 2e^-$ $CH_3CH_2OH + 5OH^- \rightarrow CH_3COO^- + 4H_2O + 4e^-$ $CH_3CH_2OH + 16OH^- \rightarrow 2CO_3^{2-} + 11H_2O + 12e^-$	-0.77	8030
Ethylene Glycol	$(CH_2OH)_2 + 10OH^- \rightarrow (CO_2)_2^{2-} + 8H_2O + 8e^-$ $(CH_2OH)_2 + 14OH^- \rightarrow 2CO_3^{2-} + 10H_2O + 10e^-$	-0.72	5200
Glycerol	$CH_2OHCHOHCH_2OH + 12OH^-$ $\rightarrow 2COO^-COHCOO^- + 10H_2O + 10e^-$ $CH_2OHCHOHCH_2OH + 20OH^- \rightarrow 3CO_3^{2-} + 14H_2O + 14e^-$	-0.69	5000

5.1.4 Main work of this chapter

The previous study shows that high index faceted palladium is effective for small organic molecules oxidation [34]. In that work, Pd nanoparticles deposited on TiO_2 nanotube arrays have been treated by square wave potential followed by formation of high index faceted Pd which further enhance the activity toward alcohols electro-oxidation.

Here we show an analogous treatment magnifies alcohols electro-oxidation at polycrystalline bulk palladium electrodes investigating the effect of the treatment on the oxidation of ethanol, ethylene glycol and glycerol.

5.2 Results and discussion

5.2.1 Surface characterization

Alteration of the palladium electrode morphology has been demonstrated by SEM inspection of the electrode surface. Fig. 5-3a and 5-3b show the low and high magnification SEM images of the polycrystalline Pd foil surface after its polishing with diamond suspension. Fig. 5-3c

and 5-3d show the low and high magnification SEM micrographs of the same surface after the SWP treatment. Image comparison reveals dramatic surface roughening after treatment.
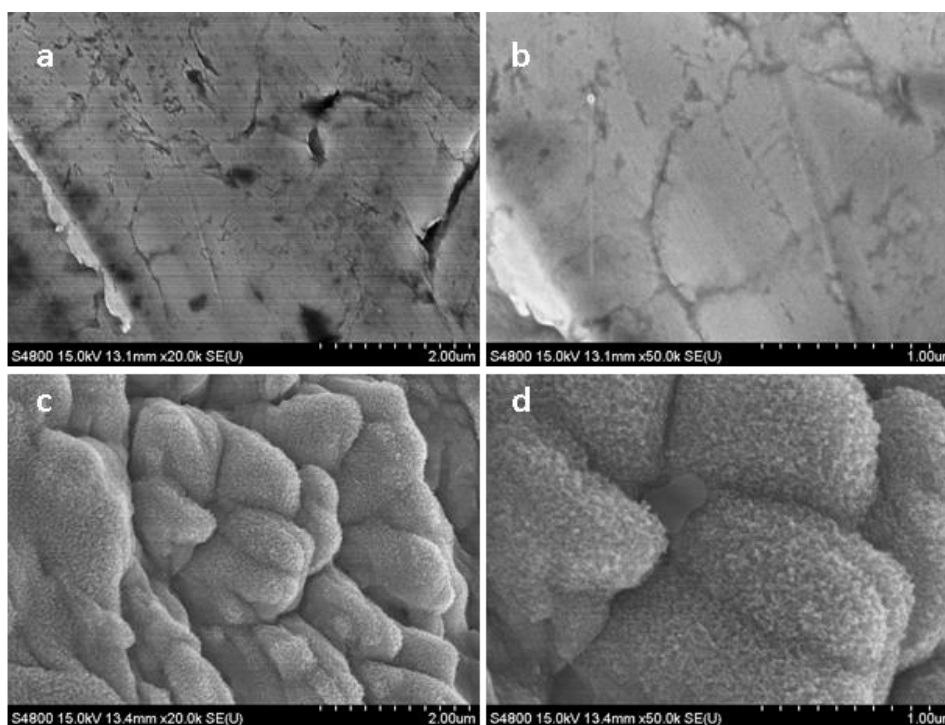

Figure 5-3. Scanning Electron Microscopy images of Pd surfaces before (low magnification (a), high magnification (b)) and after the SWP treatment (low magnification (c), high magnification (d)).

5.2.2 Voltammetric studies

Electrochemical roughening of polycrystalline palladium foil as a result of SWP treatment has been previously observed and it has been used to demonstrate the surface-enhanced Raman scattering activity as high as three orders of magnitude [92]. Here, we used different potential and frequency of SWP (Fig. 2-1). In addition, the roughing solution was changed from 1 M H_2SO_4 to 2 M KOH.

The extent of roughening has been quantified by the Electrochemically Active Surface Area (EASA) determination. EASA measurements have been performed by CV through the quantification of the cathodic peak corresponding to the reduction of a complete PdO

monolayer (1.4 V vs. RHE according to what reported in [74]). Table 5-2 shows the SWP treatment results in a twofold increase of the EASA.

Table 5-2. Parameters for the catalytic activity assessment

		Before SWP treatment	After SWP treatment
EASA (cm^2)		2.8	7.0
Onset potential (V *vs*. RHE)	Ethanol	0.39	0.19
	Ethylene glycol	0.50	0.37
	Glycerol	0.59	0.40
Peak current density / EACA peak current density (mA/cm^2)	Ethanol	34.4 / 3.5	193.9 / 7.8
	Ethylene glycol	52.4 / 5.3	207.3 / 8.4
	Glycerol	28.7 / 2.9	124.9 / 5.0

To characterize the other electrochemical properties of this treated electrode, other cyclic voltammetric studies were carried out. Fig. 5-4a gives cyclic voltammograms obtained from smooth and SWP treated Pd in 2 M KOH at a scan rate of 50 mV/s over the potential range from 0 to 1.2 V. It shows that the reduction of PdO occurs between 0.6 and 0.8 V. It is worth noting that the asymmetry of the CV after treatment (Fig. 5-4a), the positive cathodic current, should be ascribed to the oxidation processed being enhanced after treatment.
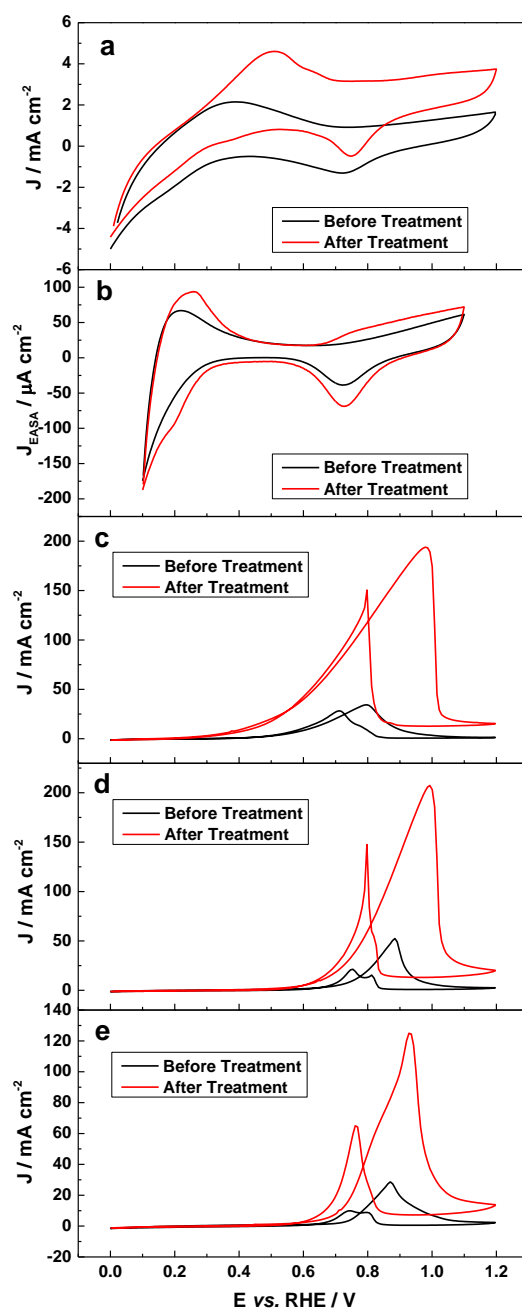
Figure 5-4. Cyclic voltammograms of Pd in a) 2 M KOH; b) 0.1 M HClO$_4$; c) 10 w.t.% Ethanol + 2 M KOH; d) 5 w.t.% ethylene glycol + 2 M KOH; e) 5 w.t.% glycerol + 2 M KOH. Scan rate: 50 mV/s.

CVs in 0.1 M HClO$_4$ were also tested to investigate oxygen adsorption/desorption electrochemical features before and after treatment (Fig. 5-4b). Specially, we display the current density normalized by EASA. Then we can find that the roughened Pd electrode presents essentially the same features as the smooth electrode except that the roughened Pd gives better-resolved hydrogen adsorption and desorption peaks in the negative potential region. Moreover, the current density of palladium oxide formation is much larger and happens at earlier potential (0.65 V). The Pd oxide reduction happened at the range of 0.6-0.8 V is also larger on treated Pd compared to smooth Pd. Both large current of the Pd oxide formation and reduction on SWP treated Pd reveals an increase in the density of low coordinated palladium atoms. The origin of such increased density may be ascribed to the rise of the number of exposed high index facets, as explained in [34]. The formation of crystal defects may not be excluded.

The electrocatalytic activity of palladium towards the alcohol oxidation (Fig. 5-4 c-e) has been estimated by CVs in 2M KOH electrolytes containing 10 w.t. % of ethanol, and 5 w.t. % of ethylene glycol and glycerol. Such fuel compositions have been found to be effective for powering alkaline DAFCs [42, 93]. From Fig. 5-4 c-e, we can find that the SWP treated Pd electrode provides lower onset potentials of alcohol oxidation as compared to the non-treated one for all the investigated electrolytes. In the same time, the dramatic increase of the peak current density for the alcohol oxidation can also be observed. The relevant quantitative value of alcohol oxidation current density was summarized in Table 5-2. The ratio between the current densities after and before the treatment is 5.6, 4.0 and 4.4 for the oxidation of ethanol, ethylene glycol and glycerol, respectively. Such ratios are much larger than the ratio of the EASA after and before the treatment, 2.5. Therefore, the much higher activity of SWP treated palladium cannot be explained solely by surface roughening.

To better understand the source of the good performance of SWP treated Pd, we'd like to trace back to the report in [34]. Over there, the same potential and frequency of SWP was used on the Pd particle which was deposited on TiO$_2$ nanotube array. High Resolution Transmission Electron Microscopy (HRTEM) analysis of the TiO$_2$ supported Pd after SWP treatment demonstrates the existence of high index facets (Fig. 5-5,6). The acquisition of HRTEM images under different focus allowed the assignment of the surface structure. Fig. 5-5 shows the presence of high index facets (210), (410) along the <100> direction. Figure 5-6

shows (211) and (311) facets along <110> direction. In addition, along the <110> direction one may also notice the presence of twinning and stacking faults.
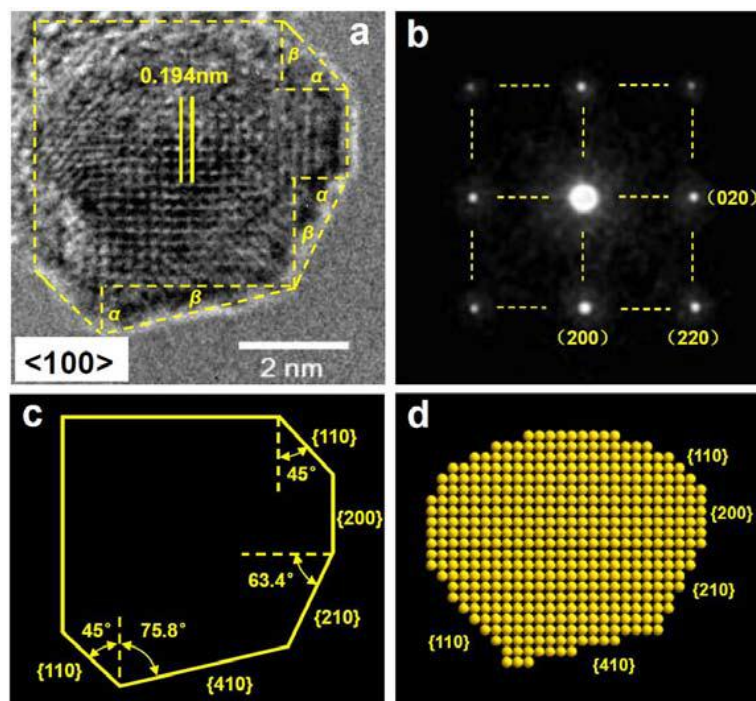

Figure 5-5. HRTEM image of Pd nanoparticles along <100> direction after SWP treatment and the corresponding facets identification. (a) HRTEM image and boundary identification; (b) Fourier Transform of the image for the determination of the axis of observation direction; (c) Sketch of the particle boundary for angle measurement; (d) Particle atomic model with facets assignment. [34]
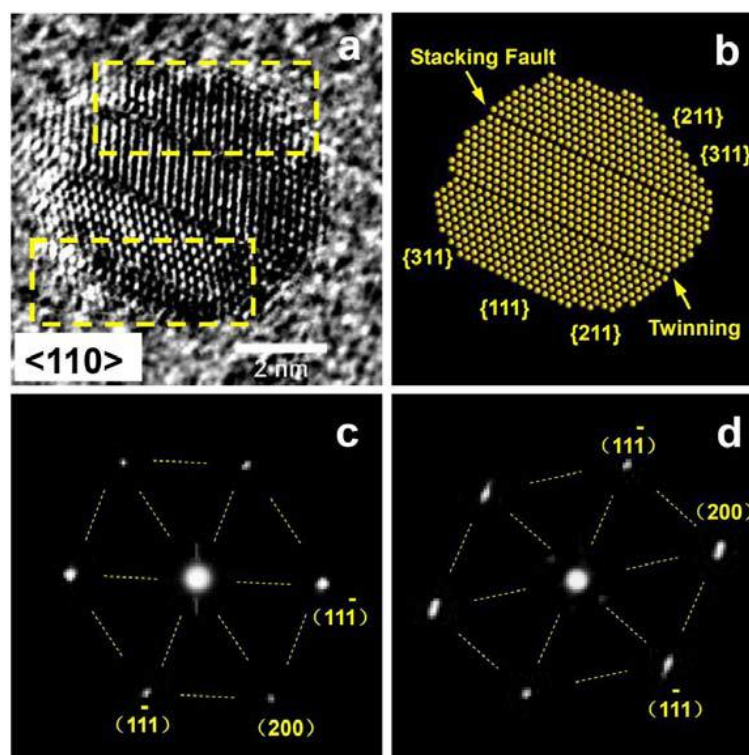
Figure 5-6. HRTEM image of Pd NP along <110> direction after SWP treatment and the corresponding facets identification. (a) HRTEM image of treated Pd; (b) Particle atomic model with facets assignment; (c,d) Fourier Transform of the image for the determination of the axis of observation direction of the top and bottom highlighted region of picture (a) respectively. [34]

In the end, combining the report in [34], we can ascribe the activity enhancement to a convolution of effect of the enlarged surface area and the increase in the density of low coordinated surface.

5.2.3 In situ FTIR spectroscopy

To detect the intermediate and products during alcohol oxidation on Pd, the *in-situ* FTIR spectroscopy was used. At the beginning, we would like to compare the difference of ethanol oxidation products on Pd before and after SWP treatment. Fig. 5-7 a,b, recorded in 10% ethanol + 2 M KOH, show the four downward bands at 1550, 1415, 1346 and 1018 cm^{-1} which allow a safe assignment to CH_3COO^- [47-48]. Nevertheless, it is known that the symmetric

stretching of COO⁻ (1415 cm⁻¹) is less intense than the asymmetric stretching band occurring at 1550 cm⁻¹ (Fig. 5-8) [48]. Unlike the normal way, Fig. 5-7 b shows the band intensity at 1415 cm⁻¹ is significantly larger as compared to the band at 1550 cm⁻¹. This effect can be ascribed to the formation of carbonate (1390 cm⁻¹) merged together with 1415 cm⁻¹. This evidence may indicate a larger tendency of the SWP treated Pd surfaces to produce C-C cleavage. The change may also be ascribed to local change in the pH for the larger activity of the system after treatment.

Figure 5-7 c,d show FTIR of the ethylene glycol oxidation on Palladium. At potential lower than 0.7 V on untreated Pd surface, we obtained oxidation bands with very low intensity which does not allow a safe assignment. At potential of 0.7 V and higher, we observe the formation of mixed carboxylates such as glycolate (1574 and 1406 cm⁻¹) [94] and oxalate (1570 and 1310 cm⁻¹) [95-96]. The formation of CO_3^{2-} cannot be excluded due to the superimposition of the carbonate bands to carboxylates. The electrooxidation of ethylene glycol on treated Pd at potential higher than 0.7V leads to the formation of glycolic acid (1732, 1436, 1083 cm⁻¹), oxalic acid (1732, 1240 cm⁻¹), glyoxylic acid (1736, 1240, 1095 cm⁻¹) and glyoxal (1415, 1083 cm⁻¹) [96-98]. At the same time, the final oxidation product, CO_2, is observed at 2343 cm⁻¹. A former report in [99] shows the influence of pH on the products of ethylene glycol oxidation. They proved that the lower pH is preferred to break C-C and then produce the CO_2. But it showed that quite small amount of CO_2 was formed on the polycrystalline Pd foil under 1.2 V even at the pH of 12. Compare the intensity of peak at 2343 cm⁻¹ in Fig. 5-7d with the result in [99], we can easily distinguish that the treated Pd oxidizes ethylene glycol to much more amount of CO_2. In the end we conclude that the observed variation in the selectivity due to a convolution of the larger tendency of the SWP treated Pd to produce C-C cleavage, which accounts for the main reason, and the local change in the pH.
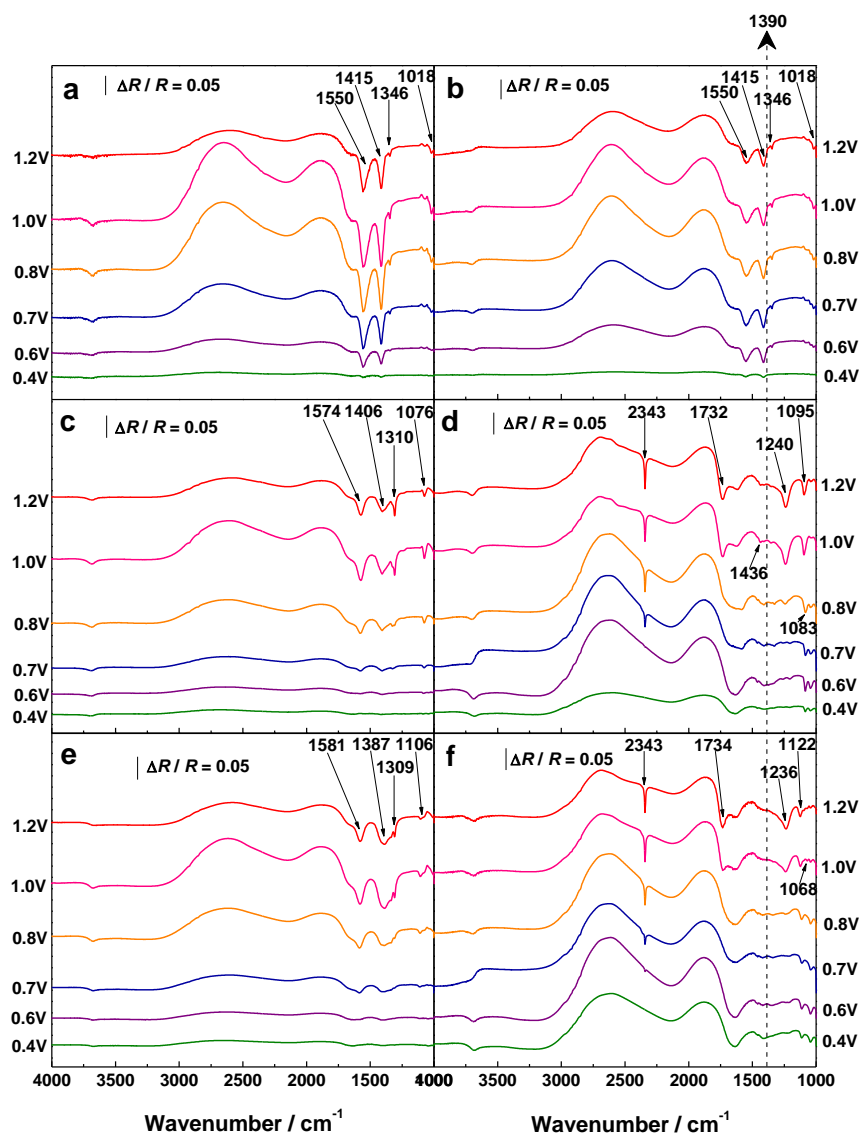
Figure 5-7. In situ FTIR spectra obtained under potential step polarization in a,b) 10% ethanol + 2 M KOH on Pd before and after SWP treatment; in c,d) 5% ethylene glycol + 2 M KOH on Pd before and after SWP treatment; e,f) 5% glycerol + 2 M KOH on Pd before and after SWP treatment.
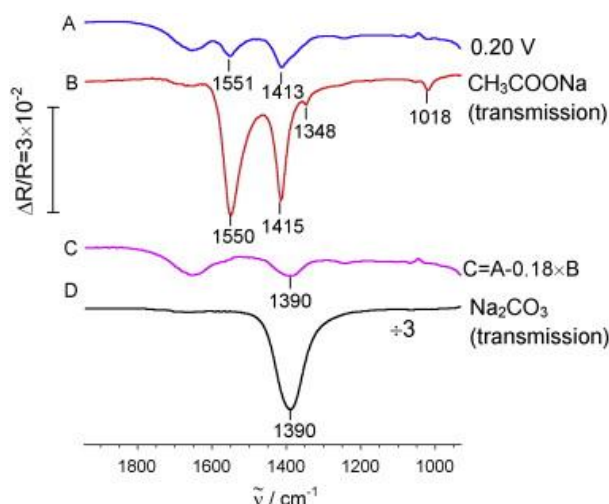
Figure 5-8. Identification of carbonate as product of ethanol oxidation. (A) *In situ* FTIR spectrum of the electrooxidation of 0.1 M ethanol; (B,D) Transmission IR spectra of 0.1 M CH_3COONa and 0.1 M Na_2CO_3 separately; (C) The resulting spectrum of $A - 0.18 \times B$.[48]

Figure 5-7 e,f show FTIR of the glycerol oxidation on Palladium. The electrooxidation of glycerol on untreated Pd results in the formation of glycerate (1581, 1387 and 1309 cm^{-1}) [100] at potential higher than 0.7 V. Carbonate formation cannot be excluded for the superimposition of the COO^- symmetric stretching band of glycerate. Instead, after the treatment, the formation of mixed carboxylic acids at potentials higher than 0.6V have been detected together with CO_2 (2343 cm^{-1}) formation.

Ethylene glycol and glycerol electrooxidation on treated Pd (Figure 5-7 d,f) results in the presence of carboxylic acids and CO_2 instead of carboxylates and carbonate which indicates pH decrease in the probed thin layer solution. The pH decrease originates from the OH^- consumption during alcohol oxidation reaction, which happened with larger intensity on treated Pd.

In brief, FTIR data not only supports the CV evidence for the increase in the electrocatalytic activity of Pd after SWP treatment, but also may suggest the difference in the selectivity of alcohol oxidation.

5.3 Conclusions

Palladium has been actively explored in recent years due to its unique properties and applications related to catalysis. Like other systems, the catalytic activity of Pd is strongly dependent on both size and shape, with the shape playing a more important role in determining the selectivity.

A simple square wave potential treatment has been used to change the size and also the crystal shape of polycrystalline palladium foil. The potential, frequency and the treating solution has been optimized selected as a former work about Pd nanoparticles deposited on TiO_2 nanotube array. Consequently, our polycrystalline palladium foil shows enhanced electrocatalytic activity for alcohol oxidation which was investigated by cyclic voltammetry. Three alcohols, ethanol, ethylene glycol and glycerol were chosen.

The CVs tested in alkaline medium show that the current density of alcohol oxidation is about 5 times higher on treated Pd than the untreated one. It is worth noting that the electrochemical active surface area is only 2.5 times. The phenomenon can be ascribed by both the roughness of surface and the change of the crystal shape, which includes the high index facets. In situ FTIR was used to test the intermediate and products of alcohol oxidation on Pd. The results reveal that a larger tendency of breaking C-C bond was happened on treated Pd towards alcohol oxidation. It proves that the treated Pd with changed crystal shape has the different selectivity of alcohol oxidation.

Our square wave potential treatment works effectively on palladium, which indicates that this treatment may be applied on the other metal surfaces to enhance their catalytic activity. Furthermore, this treatment leads to improve of the anode activity and then promote the higher efficiency of alkaline direct alcohol fuel cell.

6. Electrochemical Growth of Platinum Nanostructures for Enhanced Ethanol Oxidation

6.1 Introduction

To date platinum is still the most commonly exploited material in electrocatalysis. This is because of its good catalytic activity in a variety of energy related electrochemical reactions together with remarkable resistance to corrosion, even at high temperatures [101-104]. Polymer Electrolyte Membrane Fuel Cell (PEMFC) technology, which has a bright application aspect in electric vehicle and portable power, heavily relies on platinum for catalyzing both hydrogen oxidation and oxygen reduction reaction [105].

Platinum has also been proved to be effective for the catalysis of electrochemical oxidation of a variety of small molecules [106-109], which are more likely to be used as power sources for portable application as compared to hydrogen (Fig. 6-1). In particular, ethanol is extremely attractive for direct small molecule oxidation fuel cells operating at lower temperature values, as represented in 1.3.2.
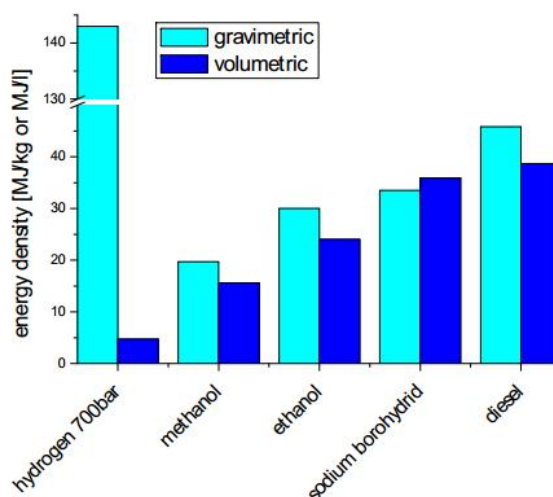

Figure 6-1. Theoretical energy storage densities for fuels considered for use in small fuel cells.

Platinum and PtRu have been shown to be effective catalysts for ethanol electrooxidation [100, 102, 105]. Recently PtSn alloys have been proved to be even more performing high activity in complete direct ethanol fuel cells tests [24-25, 110-111]. Nevertheless, the use of platinum generates two main issues hindering its practical exploitation: i) the need for high metal loadings [108, 112] and ii) CO poisoning [113-114]. The need for high Pt loadings poses severe limitations, as the scarcity of platinum resources limits its use to applications which is unavoidable. The European Union has classified platinum among the so-called "critical raw materials", stressing both on its technological relevance and rarity [115-116]. The US Department of Energy periodically publishes reports on future technology targets [117]. Lately a platinum content of 0.125 mg cm^{-2} for automotive PEMFCs has been fixed as an objective to be achieved by 2017. This is reasonably good to guarantee the sustainability of platinum supply for a full technological and commercial exploitation. At present only nanostructured thin films have been shown to be active enough to meet the requirements [118]. On the other hand, CO poisoning of platinum is critical for direct ethanol fuel cell performance. It is well known that the electrooxidation of ethanol undergoes parallel reactions producing CH_3CHO, CH_3COOH and CO_2 (Figure 6-2). CO, as an intermediate product of C-C breaking to further produce CO_2 during ethanol oxidation, strongly adsorbs at the platinum surface slowly poisoning the catalyst performance. The addition of ruthenium to platinum promotes CO oxidation and elimination, but CO poisoning is still an issue [119-125].
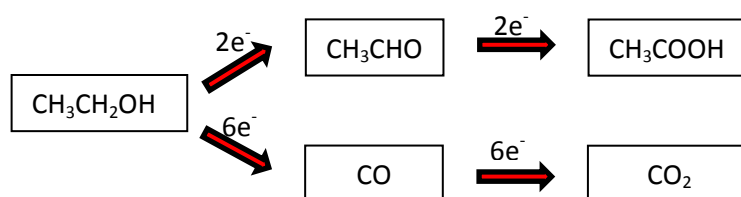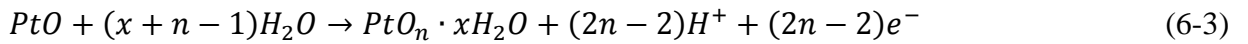

Figure 6-2. Schematic representation of the parallel pathways for ethanol oxidation.

In order to overcome the problem of CO production it has been demonstrated, at least with Pd catalysts [48], that it is convenient to operate in alkaline conditions, where the C-C cleavage of ethanol has been shown to be hampered resulting in negligible production of C_1

fragments. This could appear a limitation, in principle, as only four electrons are transferred. On the contrary, it is worth mention that to date the most energy efficient direct ethanol fuel cells are those operating in alkaline conditions resulting in the production of acetate. This is because no catalyst that produces effective C-C cleavage is actually known. Moreover, the complete oxidation of ethanol to CO_2 or carbonate has very sluggish kinetics [126-130]. These kinetic drawbacks lower fuel cell performance despite the fact of having 12 exchanged electrons.

In the present work we introduce a new approach to the activation of platinum surfaces for application in ethanol electro-oxidation in alkaline environment. Inspiration was taken from a previous paper reporting an analogous procedure for Pd. In that work a square wave potential with fixed frequency was chosen to activate the Pd surface. The procedure was successful in generating nanostructured highly active Pd electrocatalysts [34, 131]. Moreover, square wave potential treatment also has been used for Pt activation [106, 132-134]. Particularly, the nanoparticle Pt supported on carbon was treated by SWP and formed high index faceted Pt which exhibited catalytic selectivity for C-C cleavage [134]. The activation mechanism of Pt by SWP can be summarized as follow:

$$Pt + H_2O \rightarrow Pt(OH) + H^+ + e^- \tag{6-1}$$

$$Pt(OH) \rightarrow PtO + H^+ + e^- \tag{6-2}$$

$$PtO + (x + n - 1)H_2O \rightarrow PtO_n \cdot xH_2O + (2n - 2)H^+ + (2n - 2)e^- \tag{6-3}$$

Reaction (6-1) is a fast process which behaves in a reversible way. Pt(OH) species is considered as the starting material for producing the hydrated platinum oxide layer. Reactions (6-2), (6-3) are the O electro-adsorption process on platinum. The activity of the platinum electrode, which is usually assigned to dissolved oxygen in the metal during anodizing, should be primarily associated with the expansion of the metal lattice during the anodic potential treatment which facilitates oxygen penetration into the metal, at least in the order of a few metal layers [132].

The final modification of the active surface and the increase in the real surface area of platinum electrodes is produced by the electroreduction of the hydrated oxide layer generated by the SWP treatment.

$$PtO_n \cdot xH_2O + 2nH^+ + 2ne^- \rightarrow Pt + (x + n)H_2O \qquad (6\text{-}4)$$
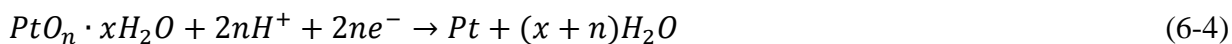
Unlike the former palladium activation procedure, we worked with different frequency and duration time of square wave potential treatment on platinum. The ultimate goal is to get nanostructured Pt with specific crystal shape to enhance the catalytic activity for ethanol oxidation with selectivity to produce acetate product to minimize the CO poisoning.

6.2 Results and Discussion

6.2.1 Surface characterization

Surface evolution as a result of the SWP treatment with various periods was investigated by field emission scanning electron microscopy. A set of three samples obtained with 6, 120 and 360 min periods was selected for such characterization. Fig. 6-3 clearly shows that surface nano-structuring occurs from a period of 6 minutes.
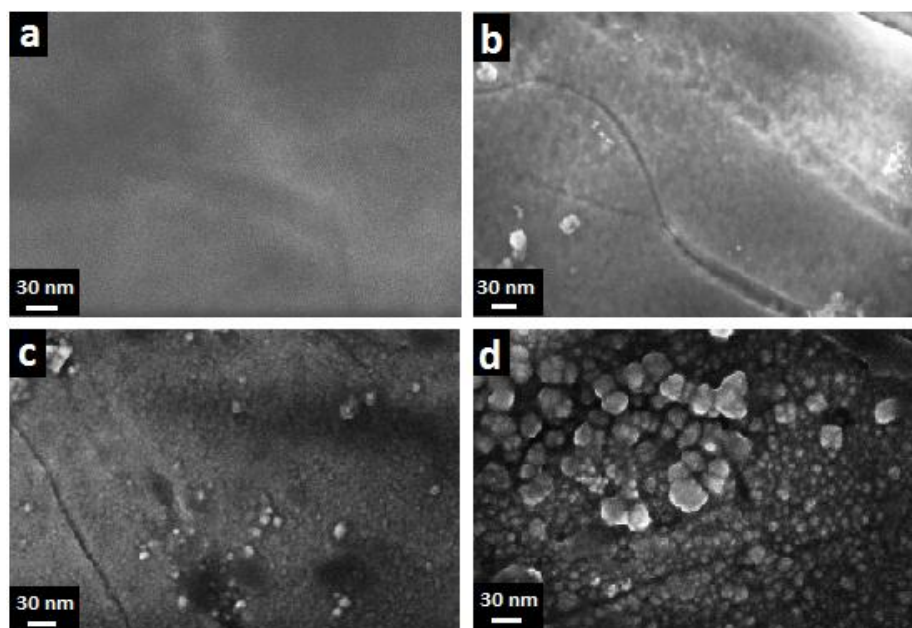

Figure 6-3. Microscopy reveals morphology changes induced by the treatment. Representative FESEM images of Pt surfaces after electrochemical treatment with different treated cycle time: a) pristine Pt surface, after square wave treatment with period of a) 6 min, b) 120 min, c) 360 min.

The roughness evolution results as a consequence of the morphology evolution occurring during platinum oxidation. It have been proven that there is an appreciable time effect of continuing growth of oxide film companied by the rearrangement of the surface structure [135]. In addition, the corresponding time of oxide reduction should be achieved. But conversely, for the time shorter than the induction time, the oxide formation scale is too low to produce significant alteration of the roughness. Longer oxidation time, usually longer than a few minutes, produce the formation of columnar islands which is revealed by a net increase in the oxidation current. Furthermore roughening may also be ascribed to platinum dissolution and re-deposition. Platinum dissolution may occur at high potentials [136]. Consistently re-deposition of dissolved platinum could be considered responsible for the formation of the largest nanostructure shown in Fig. 6-3 d. This also indicates that the metal dissolved can be recovered from the solution by subsequent electrodeposition.

6.2.2 Voltammetric studies

To give a quantitative assessment of the extent of roughening, CVs in 0.5 M H_2SO_4 was recorded (Fig.6-4). The EASA has been determined [137] from the hydrogen adsorption and desorption charge after stabilization (10 cycles). Table 6-1 shows that even the samples treated with the shortest square-wave period (6 min) the EASA is enhanced by a factor of 2.45. A fourfold enhancement was obtained for the 360 min square-wave period.

Table 6-1. Active surface area of SWP treated Pt.

Period (min)	Active Surface Area (cm^2)
0	1.806
6	4.433
120	6.177
360	7.246

A more detailed analysis of the CVs in the hydrogen adsorption/desorption region (<0.35 V) reveals changes in the distribution of the crystal terminations (Figure 6-4a). The two peaks, observed at the anodic scan of 0.11 and 0.22 V, in Under Potential Deposition (UPD) of hydrogen of the untreated sample can be attributed to H desorption on (110) and (100) sites respectively [138-140]. No clear H-desorption peak but a weak shoulder at 0.29 V possibly corresponding to the large (100) domains can be observed [141-142]. The hydrogen adsorption peaks position and current density change as a result of the treatment indicating the changing of the distribution of facets [143].
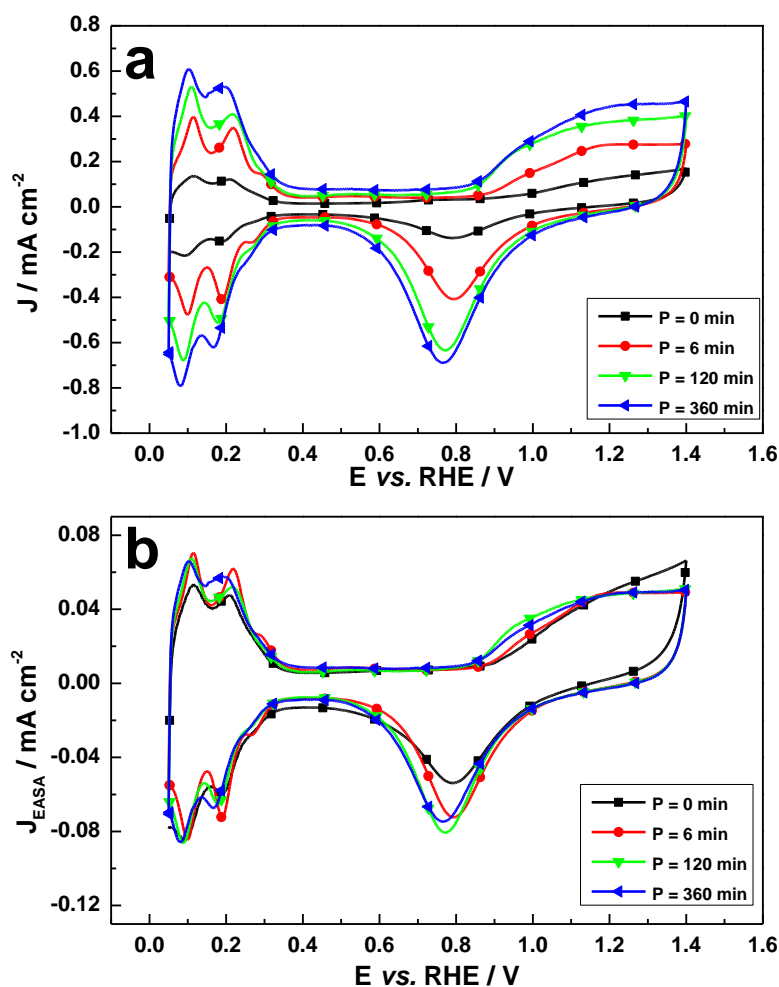

Figure 6-4. Cyclic voltammetry explains the surface modifications by SWP treatment. CVs in 0.5 M H_2SO_4 at a scan rate of 50 mV/s normalized by geometric area (a) and normalized by the EASA (b).

Surface structure evolution is also supported by the analysis of the CVs in the Pt oxidation region of 0.8 - 1.4 V. Pt oxidation is known as proceeding via a two-step mechanism according to equation 6-1 and 6-2. Eq. 6-1 is referred to the formation of a surface hydroxide while eq. 6-2 represents the formation of the surface Pt oxide. Two equations together are the electrochemical reactions that account for the anodic current density in the Pt oxidation region of the CV. Peculiarly, the detailed information of the Pd oxide reduction in Fig. 6-4 has been shown in Fig. 6-5. We observe that an extension of cycle time results in (a) larger current density of the peak of oxide reduction which indicates the formation of thicker oxide film; (b) the reduction peak potential which consistently shifts towards less-positive values is due to the more stable formation of Pd oxide.
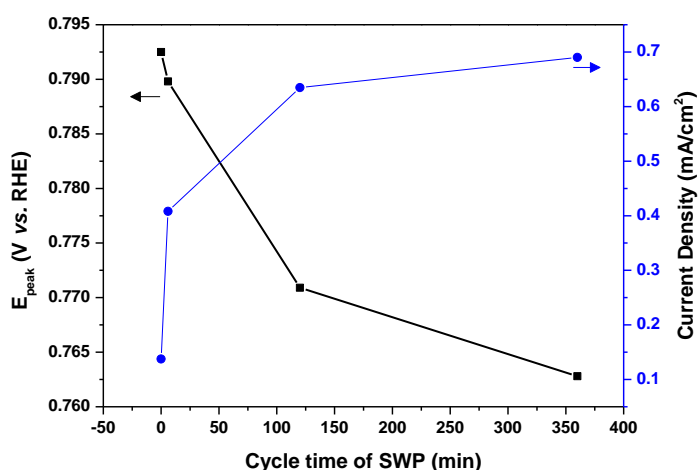

Figure 6-5. The relationship of the peak potential and charge density of Pd oxide reduction with SWP cycle time.

To have an insight into the detailed surface structure evolution of SWP treated platinum, we compared the CVs with EASA normalized current density (Fig. 6-4b). As we know, an increase in the EASA normalized current density for Pt oxidation at potential lower than 1.0 V is an indication of the presence of a larger density of low coordinated platinum atoms. In

addition, platinum sites with low coordination number show much higher tendency of oxide formation as compared to high coordination sites. The larger stability of platinum oxide results in the cathodic shift of the peak of the platinum oxide reduction [135]. The high density of low coordination surface atoms has been proved to promote the electro-catalytic oxidation of small organic molecules [91, 106]. In Fig 6-4b it is evident that amongst all the investigated samples the 120 min shows the largest EASA normalized current density under 1.0 V. Notably this is also the sample showing the largest ethanol oxidation activity which will be shown later. According to this we can conclude that the sample obtained with the cycle of 120 min is the one showing the largest density of low coordinated Pt surface atoms [91]. For SWP period larger than 120 min, such a density slightly diminishes. This could be attributed to the way that longer time produces a thicker oxide scale whose reduction results in the formation of larger nanostructures. Furthermore, as observed by FESEM investigation, re-deposition of dissolved platinum cannot be excluded leading to a completely different mechanism which, in principle could favor to form more thermodynamically stable surfaces.

Electrocatalytic activity of a series of SWP treated Pt was assessed toward ethanol electrooxidation in alkaline medium. It has been reported that higher ethanol and KOH concentration are required to get higher adsorption of ethoxy and hydroxyl yielding an increase in an oxidation current of EOR [45, 47]. Hence, we chose 2 M Ethanol 2M KOH solution electrolyte instead of low concentration electrolyte. In addition, another reason of choosing this 2 M Ethanol 2M KOH electrolyte is because it has been shown to be the most performing electrolytes in Direct Alcohols Fuel Cells [42, 73, 131].

The first voltammetric half-cycle sweeping between 0.05 and 0.70 V, are shown in Fig. 6-6a. The positive potential limit was chosen before the onset of surface oxidation to avoid surface disordering due to the formation and subsequent reduction of irreversible surface oxides [144]. It can be seen that the currents are monotonously increasing with increasing potential. Different voltammetric profiles can be found for Pt with different SWP treated period. The changes in the onset potential of the ethanol oxidation reaction and in the total current can both be found in Fig. 6-6a. All the treated Pt surfaces show lower onset potential of EOR. Particularly, the onset potential of Pt with treatment of 120 min shifts more than 100 mV negatively compared to other samples. This is consistent with the CV result of Pt oxidation in Fig. 6-4. As we know, platinum shows lower activity than palladium for ethanol

electrooxidation in alkaline media [145-146]. The current density of 3.0 mA/cm^2, which is shown at 0.7 V of untreated Pt in Fig. 6-6a, is lower compared to Pd towards ethanol oxidation in similar electrolyte reported in [45, 47]. However, Pt after treatment shows much higher current density towards ethanol oxidation compared to Pd. Especially, the current density of 9.1 mA/cm^2 on 0.7 V is found at the 120 min sample.
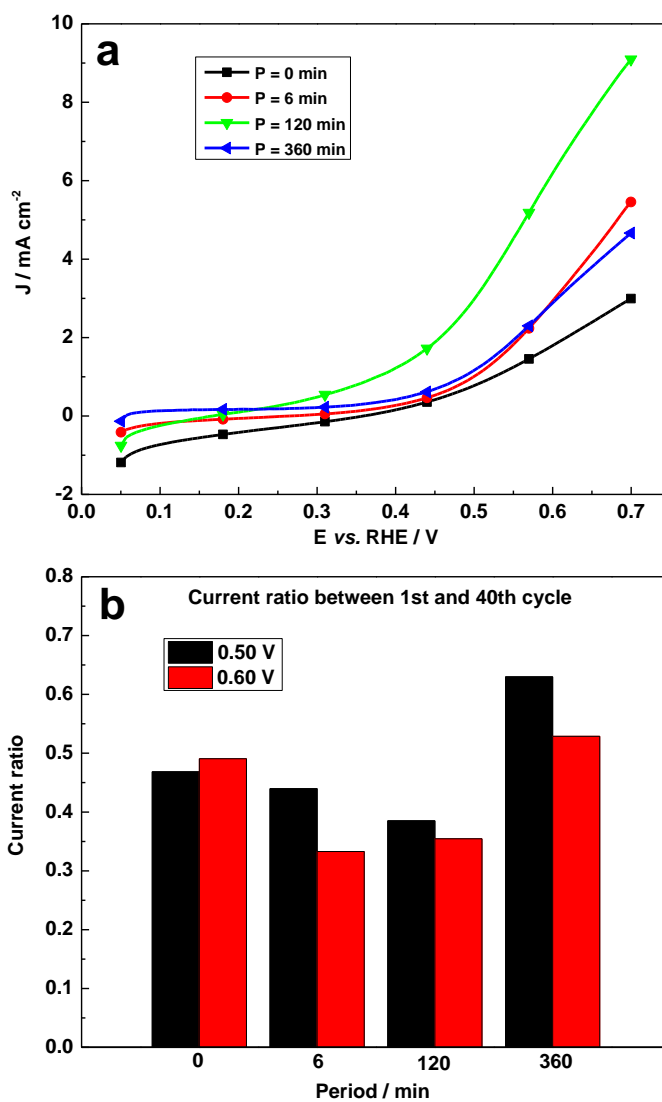

Figure 6-6. Electrocatalytic performance improves as a result of the surface modifications induced by the treatment. First positive sweep of the CVs in 2 M Ethanol 2 M KOH electrolyte (a) and current density ratio between the first and the fortieth cycle at 0.50 V and 0.60 V (b). The current is normalized by geometric area.

To see clearly through the CV performance of different treated samples, the current density at 0.50 and 0.60 V of Figure 6-6a was summarized in Table 6-2. A current density of 6.05 mA/cm^2 at 0.6 V was recorded for the 120 min sample while the untreated sample only delivered 1.75 mA/cm^2. And not only that, this current density of 120 min sample is even larger than the 360 min sample (2.80 mA/cm^2). This indicates that the peculiar structural modification, which can be identified by the CVs in H$_2$SO$_4$, plays a major role in ethanol oxidation catalytic activity. It can be explained that, surface defects, steps and kinks with their low coordination numbers (CN<8), usually exhibit very high chemical reactivity and catalytic activity for electro-oxidation of small organic molecules [134].

Cyclic voltammetry was also used to test the stability of the series of Pt samples. A total of forty cycles of CVs were measured. Fig. 6-6b reports the current ratio between the first and the fortieth cycle at 0.5 and 0.6 V respectively. And the original data of current density at 0.50 and 0.60 V of the positive-going scan of the 1st and 40th voltammetry cycles are shown in Table 6-2. The current of the 120 min sample drops significantly after 40 cycles. This sample lost more than 60% activity both at 0.50 and 0.60 V. This aspect can be related to the evolution of surface structure as a result of CV cycling, and can be possibly ascribed to the lower thermodynamic stability of open shell structures [135]. The lowest degradation rate has been obtained with the 360 min sample. After 40 cycles the activity of this sample was reduced of 37% and 47% at 0.5 and 0.6 V respectively.

Table 6-2. Current density at 0.50 and 0.60 V of the positive-going scan of the 1st and 40th voltammetric cycles for the electro-oxidation of 2 M Ethanol 2 M KOH electrolyte.

Period (min)	J (mA/cm^2) at 0.50 V		J (mA/cm^2) at 0.60 V	
	1st cycle	40th cycle	1st cycle	40th cycle
0	0.76158	0.35670	1.74697	0.90146
6	0.98782	0.46006	2.83116	0.98772
120	2.92976	1.18278	6.05378	2.23189
360	1.14237	0.75847	2.80075	1.54492

To further investigate the stability of SWP treated platinum, the ethanol oxidation reaction was also studied over longer time-scales with chronoamperometry measurements, as shown in Figure 6-7. In these measurements, the potential was stepped from 0 to 0.50 V at t = 0, after which the potential was kept constant for 1 hour. The potential of 0.50 V was chosen because it was well in the potential region where all surfaces show oxidation currents. In addition, the choosing of 0.50 V is of practical significance to portable application of direct ethanol fuel cells. It can be seen that the final activity trend qualitatively mirrors the trend found in the voltammetric measurements. All surfaces show a monotonously decaying current over time, with the rate of decay being the lowest for Pt 360 min and the highest for untreated Pt. At the end of the experiment, the current density for the 360 min sample was still 119 μA/cm^2 while the untreated sample couldn't deliver any appreciable current density indicating the almost complete exhaustion of the electrocatalytic activity. Therefore, Pt with the longest treated period is the optimal surface as balancing the catalytic activity and the catalytic stability.
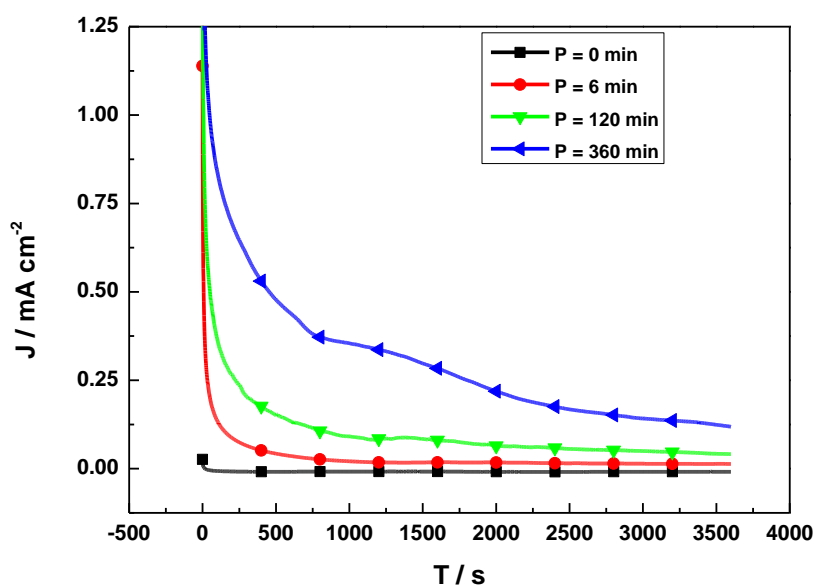
Figure 6-7. Enhanced electrocatalyst stability. Chronoamperometric curves recorded in 2 M Ethanol 2 M KOH electrolytes at 0.50 V. The current is normalized by geometric area.

6.2.3 In-situ FTIR spectroscopy

In situ Fourier Transform Infrared spectroscopy measurements were performed in order to shed more light on the electrochemical intermediate and product of ethanol oxidation on Pt surfaces. Two Pt were chosen as the working electrode, untreated Pt and SWP treated Pt with the 360 min cycle time. The latter one was selected as it showed the best performance in voltammetric measurement (combining catalytic activity and stability). Spectra have been recorded in an electrolyte containing 2 M KOH plus 2 M ethanol solution in the 0.1 - 1.2 V range. A series of typical in-situ FTIR spectra of ethanol oxidation are shown in Fig. 6-8.

For potential up to 0.2 V, the only detected oxidation product, even if in tiny amount, was CO_3^{2-} (1390 cm^{-1}) for both the examined surfaces. Formation of acetate starts at 0.3 V. It is worth noticing that the symmetric stretching vibration of COO^- (1415 cm^{-1}) cannot be resolved from the CO_3^{2-} (1390 cm^{-1}) [48]. The integrated band intensity ratio between 1415 cm^{-1} and 1550 cm^{-1} was shown in Table 6-3. The ratio for the treated sample is in a very steady state, around 0.84. Oppositely, the ratio for the untreated sample dropped from 1.104 to 0.889

with the potential increasing from 0.4 to 1.0 V. In particular, all the ratios of untreated sample are larger than treated one. This indicates that at most of the explored potential range, the FTIR spectra show that the formation of carbonate is negligible in the treated sample (Figure 6-8b). This is distinct from the pristine polycrystalline platinum foil which produces carbonate during the whole potential window (Figure 6-8a).

As we know, the formation of CO_2/CO_3^{2-} requires C-C cleavage and further CO formation which strongly adsorbs on the surface of platinum and occupies the activate atoms for ethanol adsorb and oxidation. Ultimately, this affects the stability of the device performance and limits technological exploitation. Two other downward bands at 1346 and 1018 cm^{-1} are also assigned to CH_3COO^- vibration modes. The two upward bands at 1093 and 1050 cm^{-1} are characteristic of ethanol (C-O stretching vibration), indicating its consumption as a result of the electro-oxidation. It is particularly important to compare the intensity of the bands, especially 1550 and 1415 cm^{-1}, in Figure 6-8a and Figure 6-8b. The latter one shows significantly more intense as compared to the former one. This is in good agreement with the results of chronoamperometry and CV.
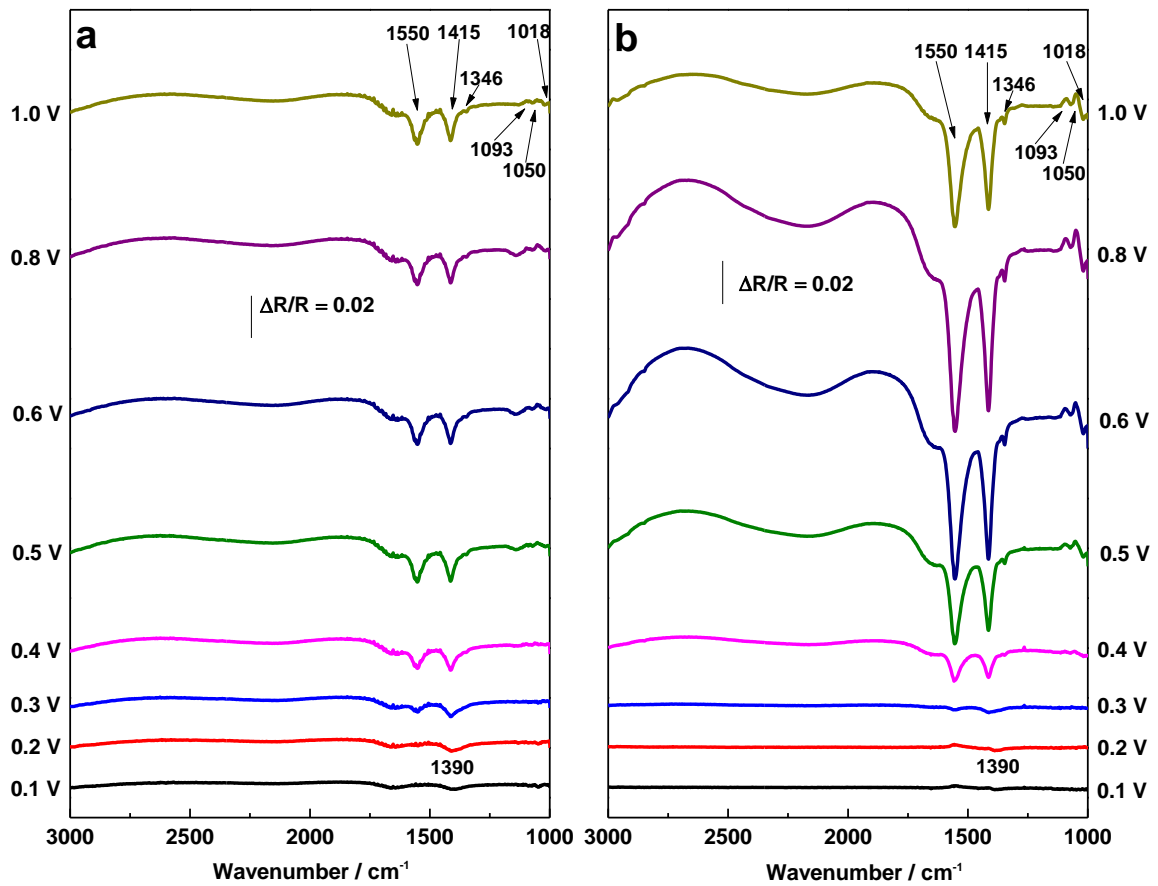
Figure 6-8. Spectroelectrochemistry investigation. In situ FTIR spectra obtained under potential step polarization in 2 M Ethanol 2 M KOH solution on Pt a) before treatment; b) after SWP treatment with the treating cycle of 360 min.

Table 6-3. The integrated band intensity ratio between the symmetric stretching vibration of COO⁻ (1415 cm⁻¹) and the asymmetric stretching vibration of COO⁻ (1550 cm⁻¹) in Figure 6-8.

Potential (V)	Band intensity ratio on Pt before treatment	Band intensity ratio on Pt after treatment with the treating cycle of 360 min
0.4	1.104	0.853
0.5	0.972	0.820
0.6	0.969	0.845
0.7	0.977	0.856
0.8	0.930	0.855
0.9	0.902	0.841
1.0	0.889	0.827

6.3 Conclusions

We have successfully demonstrated that oxidation and subsequent reduction can be used for enhancing the electrocatalytic activity of platinum surfaces. The application of square wave potential with high anodic (4.55 V) and high cathodic polarization (-1.95 V) enhances the active surface area up to a factor of 4 as compared to pristine Pt. The frequency of the square wave potential treatment has major profound implications in the evolution of the Pt surface morphology and structure. We have found that the sample obtained with the longest treating period results in highest active surface area while the sample of 120 min shows the biggest structure evolution.

Elctro-activity of the series of Pt surfaces was investigated for ethanol oxidation by voltermmetric measurements. The most active surface has been produced with a treating

period time of 120 min. Nevertheless, the 360 min sample has been found to be the most performing of stability. Structural effects may also be advocated for such an electro-catalytic activity enhancement. This is analogous to what has been previously shown by applying similar treatment on polycrystalline Pd.

Furthermore, in-situ FTIR measurements have shown that treated Pt surface has a significantly lower tendency to provoke C-C cleavage as compared to pristine Pt. This is especially important for practical applications as without C-C cleavage no production of adsorbed CO occurs, avoiding CO poisoning. This may explain the high stability of the surface which has been shown both by cyclic voltammetry and chronoamperometry.

This investigation is important for technological exploitation as it indicates that the proposed treatment allow a strategy to increase the stability of the performance of alkaline direct ethanol fuel cells for portable power application.

7. Deactivation of Palladium Electrocatalysts for Alcohols Oxidation in Basic Electrolytes

7.1 Introduction

7.1.1 Application of palladium as electrocatalysis

Palladium nanocrystals have been actively explored in recent years due to their unique properties and applications related to electrocatalysis. The main two application of Pd can be divided into two groups: as anode electrocatalyst in alkaline direct alcohol fuel cells and as electrocatalyst to get hydrogen production in water electrolyzer.

7.1.1.1 Palladium in alkaline direct alcohol fuel cells

As a less expensive and much larger abundant material than platinum, palladium shows better electrocatalytic activity in alkaline especially for ethanol oxidation reaction [145-146]. Nanostructured palladium has been recently employed as anode electrocatalyst in fuel cells fed with liquid alcohol electrolytes [42, 93, 147-149]. Fuel cells equipped with palladium anode deliver power densities even exceeding 100 mW cm^{-2} from alkaline alcohols electrolyte [42, 93, 149]. Such power densities are sufficient to support small portable devices.

Alkaline Direct Alcohol Fuel Cells (DEFCs) are also a completely Pt-free technology [150]. This is because non-noble metals are much stable in alkaline electrolytes compared to acid. Therefore, non-noble metals can be employed for catalyze the oxygen reduction reaction [68, 151]. This is a net advantage over concurring acidic technologies. Not only that, such non-noble metal electrocatalysts don't show any open circuit potential drop from fuel crossover [71], which owe to their completely inactive property for alcohol oxidation reaction.

7.1.1.2 Palladium in hydrogen production by electrochemical reforming

Hydrogen, as an efficient energy carrier, can be produced by two main trends, reforming of organic feedstock and water electrolysis.

Water electrolysis has the advantage of producing extremely pure hydrogen which makes it have a good application prospect. Especially, water electrolysis with a polymer electrolyte membrane possesses certain advantages compared with the classical alkaline process like: increased energy efficiency and specific production capacity and a simple system with a solid electrolyte at a low temperature. Nevertheless, its application is still limited by two major obstacles: high cost of catalyst material and high cost of electrical energy consumption.

One efficient strategy for reducing energy consumption of PEM electrolysis is the replacement of water with a soluble substrate which has a much lower oxidation potential. Compounds such as ammonia, methanol, ethanol, and glycerol have been investigated in PEM electrolysis. As the unique catalytic acivity of palladium in alkaline medium, Pd catalysts have been employed in the electrochemical reforming, achieving hydrogen productivity with energy saving higher than 50% as compared to the most advanced PEM electrolyzers [152-153].

7.1.2 Limitation of palladium exploitation

The main issue hampering the full exploitation of Pd as catalytic material for electrochemical oxidation of alcohols is the lack of stability.

A few previous papers have speculated that degradation can be ascribed to the adsorption of CO which is similar with what happens in acidic environment. We believe that such CO adsorption is not the primary cause in alkaline medium. It is a consolidated fact that C-C cleavage in ethanol oxidation does not occur at pH larger than 13 on Pd catalysts [47]. So we conclude that no possible pathways lead to CO adsorption occurs; or if it is so, it happens only in a very limited and undetectable amount.

In previous papers we have hypothesized that Pd oxidation could be the possible reason [45, 154]. We formulated this hypothesis from indirect evidence obtained from electrochemical measurements. Particularly we have noticed that the addition of tiny amount of sodium borohydride, a strong reducing agent, to the fuel compartment is beneficial to the DEFCs stability [155]. This investigation supports the assumption of Pd oxidation as the degradation reason but CO poisoning as the possibility of degradation cannot be excluded.

7.1.3 Main work of this chapter

With the present work we aim at identification of the Pd deactivation mechanism. A smart selection of the anode catalyst architecture and the operating conditions has been done to maximize the stability of the performance.

On the one hand, half-cell studies, including cyclic voltammetry and chronoamperometry, were investigated in the electrolyte containing ethanol. On the other hand, full-cell studies were performed in passive direct ethanol fuel cell. In particular, both half-cell and full-cell tests were fixed in alkaline medium because it is well known ethanol can be selectively oxidized to acetate without C-C cleavage which lead to the formation of CO poisoning adsorbents at pH above 13 [47]. Oppositely, C-C cleavage may occur on heavier alcohols, such as ethylene glycol, even at pH larger than 13 [99].

Furthermore, we have focused on the effect of a concentration of the electrolyte and the effect of the anode potential for the performance degradation.

Moreover we have investigated the palladium oxidation state in the anode catalyst by Fixed Energy X-Ray Absorption Voltammetry (FEXRAV) which keeps the detected energy constant while observing the variation of the X-ray mass absorption coefficient as a function of the applied electrode potential [62]. Here we applied FEXRAV to investigate the evolution of the palladium chemical evolution during cyclic voltammetry both in alkaline electrolytes with and without ethanol.

7.2 Results and discussion

7.2.1 Electrocatalyst characterization

The crystal structure of the resulting Pd/C electro-catalyst was investigated by XRD technique. The Pd nanoparticles supported on carbon black exhibits an XRD pattern of a typical face-centered-cubic (fcc) lattice structure as shown in Fig. 7-1. The strong diffraction peaks at the Bragg angles of 40.16°, 46.54°, 68.31°, 82.05° and 86.83° correspond to the (1 1 1), (2 0 0), (2 2 0), (311) and (222) facets of Pd crystal. The Pd (1 1 1) peak was used to calculate the particle size of Pd according to the Scherrer Equation. The average Pd nanoparticle size of Pd/C is 8.4 nm. The result indicates that palladium particles are well dispersed on carbon. In addition, no characteristic peaks of other impurities such as palladium oxide are detected.
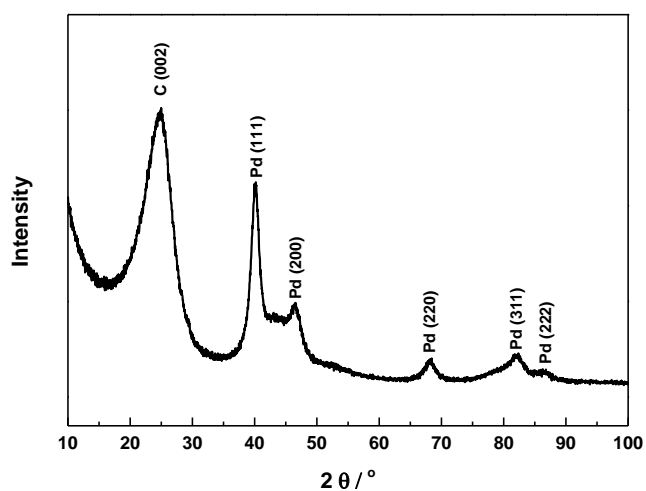
Figure 7-1. X-ray powder diffraction patterns of Pd/C.

Meanwhile, the crystal structure of FePc–CoPc/C, which is used as cathode catalyst of passive DEFC, was also investigated by XRD (Fig. 7-2). XRD spectra show the absence of any crystalline phase deriving from the decomposition of the metal complexes. Only the typical pattern of the carbon with two very broad diffraction peaks centered at ca. 25 and 43° can be observed.
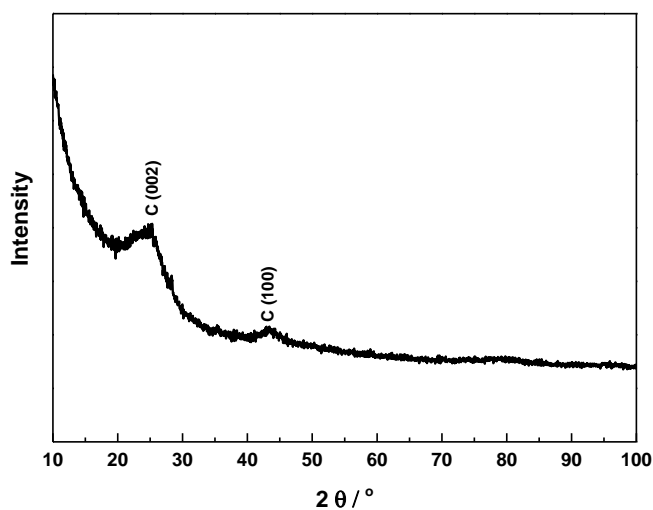

Figure 7-2. X-ray powder diffraction patterns of FePc-CoPc/C.

The morphology and structure of Pd/C has been demonstrated by TEM investigation, as shown in Fig. 7-3. Palladium particles are immobilized in a well-dispersed way on the outer surface of carbon. It can be observed that the diameter of palladium particles is about 5–10 nm, which is in accordance with the XRD result.
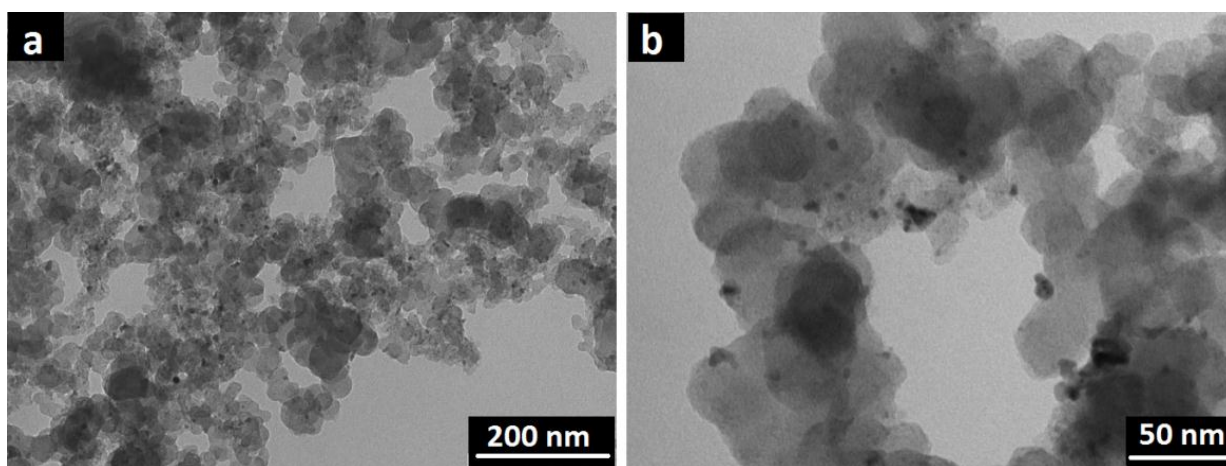

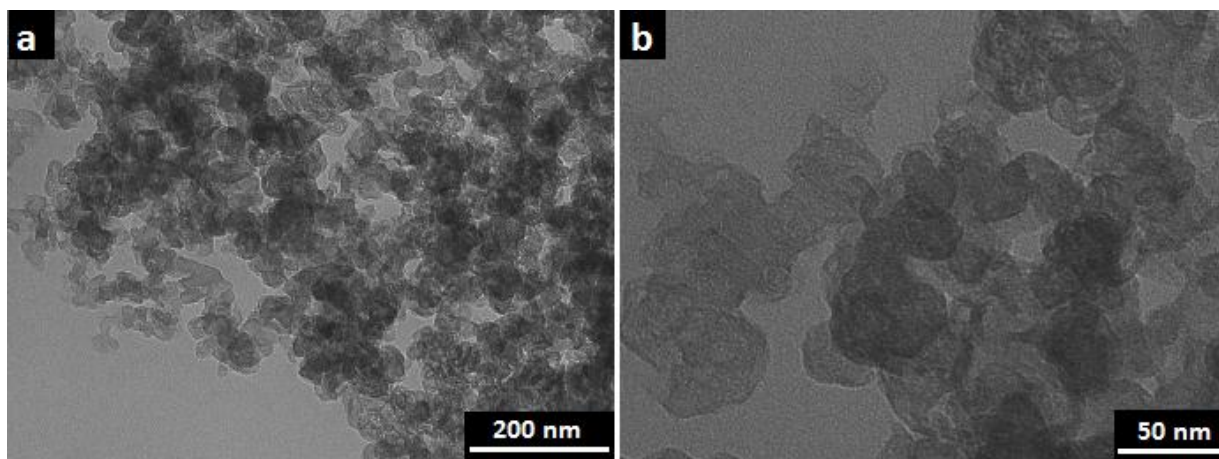**Figure 7-3.** Low and high magnification TEM micrographs of Pd/C.

Figure 7-4. Low and high magnification TEM micrographs of FePc-CoPc/C.

In addition, the morphology of FePc-CoPc/C has also been demonstrated by TEM investigation, as shown in Fig. 7-4. The material is dispersed uniformly at the whole detective range. No obvious particle belongs to any metal or alloy can be found.

7.2.2 Half-cell investigation

The activity and degradation of Pd/C was assessed by cyclic voltammetry (Fig. 7-5). The CVs of the Pd/C in 2 M KOH are shown in Fig. 7-5a. 0 - 0.40 V is the area of adsorption and desorption of hydrogen. A shoulder on the positive sweep around 0.60 V is attributable to pre-monolayer hydrous oxide formation [156]. Firstly Pd reacts with adsorbed OH^- to form Pd-OH_{ads}, and then Pd-OH_{ads} is further oxidized to Pd oxide [74], which can be expressed as Eq. 7-1,2.

$$Pd + OH^- \rightarrow Pd - OH_{ads} + e^- \qquad (7\text{-}1)$$

$$Pd - OH_{ads} + OH^- \rightarrow Pd - O + H_2O + e^- \qquad (7\text{-}2)$$

Pd-OH_{ads} is a reactive specie and its formation is highly reversible [156]. For this reason it cannot be advocated as a possible reason of performance degradation. The onset potential of Pd electro-oxidation is shown at about 0.70 V, which agrees well with the former reports [157-158]. Its reduction, observed in the reverse scan, usually occurs in the potential range of 0.45-0.90 V as clearly seen in Fig. 7-5a.
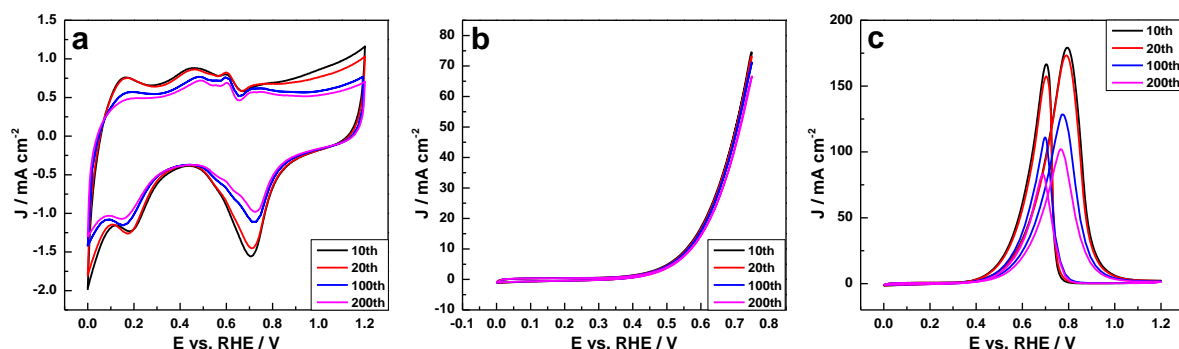

Figure 7-5. Cyclic voltammograms of Pd/C in (a) 2 M KOH and (b,c) 2 M Ethanol + 2 M KOH. Scan rate: 50 mV/s.

If the CV range is extended to 1.45 V, the reduction peak can be used for quantifying the real surface area of the catalyst (Fig. 7-6). It is recognized that the formation of the first monolayer of palladium oxide is achieved at 1.45 V [74]. The real surface area of the Pd/C catalyst calculated by this way is 81.8 m^2/g.
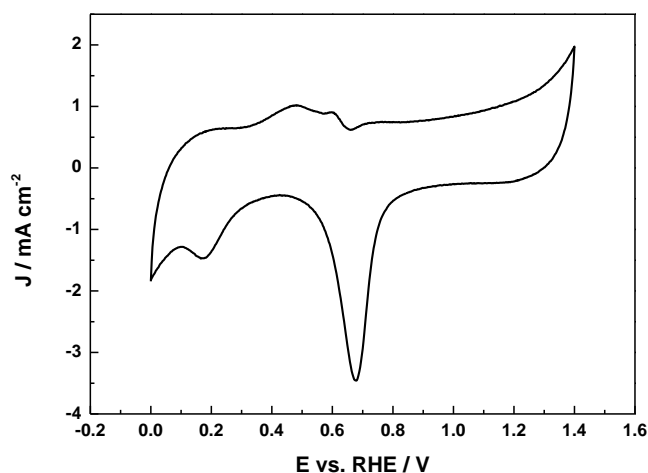

Figure 7-6. Cyclic voltammograms of Pd/C in 2 M KOH electrolyte. Scan rate: 50 mV/s.

What is the evolution extent of the catalyst as determined by a large amount of CV cycles? To answer this question we have cycled our catalyst between 0.00 and 1.20 V for 200 times at a scan rate of 50 mV/s. We have measured the electrochemical active surface area with a CV scan with the upper potential of 1.45 V after 10, 50, 100 and 200 cycles. The relevant data have been displayed in Table 7-1. Catalyst degradation is evident. Actually the peaks due to hydrogen absorption/adsorption decrease significantly and so also do the palladium oxide formation and reduction current. We can now formulate three hypothesis for such a degradation: i) loss of catalytic material from the electrode, ii) particle coarsening, iii) irreversible oxidation [159]. The first point can be safely discarded. No material has been found in the solution together with the evidence of no violent gas evolution from the working electrode during the measurements. At this stage, we cannot discriminate the final reason of

catalyst degradation from the last two hypotheses and the question cannot be resolved only with cyclic voltammetry.

The growth of oxides on Pd is complex and proceeding with the formation of a few layers of conformal oxide over the Pd surface (alpha oxide) then producing roughening (beta oxides) [74]. The oxide classification is based on their morphology rather than on their chemical state. It is known that the beta form is far less reversible than the alpha form. Furthermore, Pd(II) ions are formed by chemical dissolution of the oxides and during their electrochemical reduction [159]. Such transformation signifies the deactivation of active sites for electro-oxidation reaction of ethanol. This phenomenon can be confirmed by Figure 7-5b, c.

We have evaluated the catalytic activity of Pd/C by CVs in 2M KOH plus 2M ethanol electrolyte cycling for 200 times at 50 mV s^{-1}. We chose this composition because it shows good performance in alkaline direct ethanol fuel cells [42, 82]. Figure 7-5b and 7-5c report the CVs obtained with two different upper potential limits, 0.7 and 1.2 V (only forward scans reported). These data clearly show that larger potential limit implies a faster degradation rate.

In fact, curves appear significantly more depressed after cycling in Fig. 7-5c (0 - 1.2 V) as compared to Fig. 7-5b (0 - 0.7 V) in agreement with the electrochemical active surface area evolution as determined in bare KOH (Fig. 7-5a). We conclude that the anodic stress of the catalyst is a significant parameter in determining the evolution of the performance. More importantly it has been reported that CO adsorption does not occur on Pd at potentials larger than 0.75 V RHE in alkaline environment [160]. According to this reason, if CO was the problem we should be expected to observe greater degradation in the cyclic voltammetry with the limit potential of 0.70 V as compared to the CVs with upper potential at 1.20 V.

Table 7-1. Electrochemical active surface area of Pd/C at different voltammetric cycles in 2 M KOH.

Voltammetric Cycle Number	Electrochemical Active Surface Area (cm^2)
1	1.451
10	1.405
20	1.321
50	1.161
100	1.042
200	0.939

The electrochemical stability of Pd/C for ethanol electro-oxidation was investigated by chronoamperometric measurement at 0.7 V in different electrolytes (Figure 7-7a). The polarization current for the ethanol electro-oxidation reaction shows a rapid decay from 35 to 15 mA/cm^2 within 1 h in the first place. This may indicate a similar poisoning mechanism of the intermediate species during the ethanol electro-oxidation reaction on Pd/C. At the following 9 h test, the oxidation current on Pd/C is considerably stable with falling slowly. In addition, the chronoamperograms show that a decrease in ethanol concentration is accompanied by a decrease in currents obtained.

Figure 7-7b-d show the comparison of CVs, which recorded before and after chronoamperometry at 0.7 V for 10 h respectively. The current loss after constant voltage test is only 8.8% from 179.2 to 163.5 mA/cm^2 in 2 M Ethanol and 2 M KOH electrolyte (Fig. 7-7b). Nonetheless, the current loss was intensified with decreasing the concentration of ethanol. The current loss ratio are 14.7% and 23.9% in 1 M Ethanol + 1 M KOH and 0.5 M Ethanol + 0.5 M KOH separately (Fig. 7-7c,d). The phenomenon, current loss ratio decease with increasing ethanol concentration, can be attributed to the reducibility of ethanol. Ethanol as an

additive can reduce palladium oxide to palladium has been testified by Time resolved X-ray absorption spectra around the Pd K-edge by J. Grunwaldt [161].

During ethanol electro-oxidation, ethanol also plays another role of reducing the inert palladium oxide back to active palladium. Furthermore, higher ethanol concentration has an even stronger effect of activating the Pd (II) back to Pd (0).
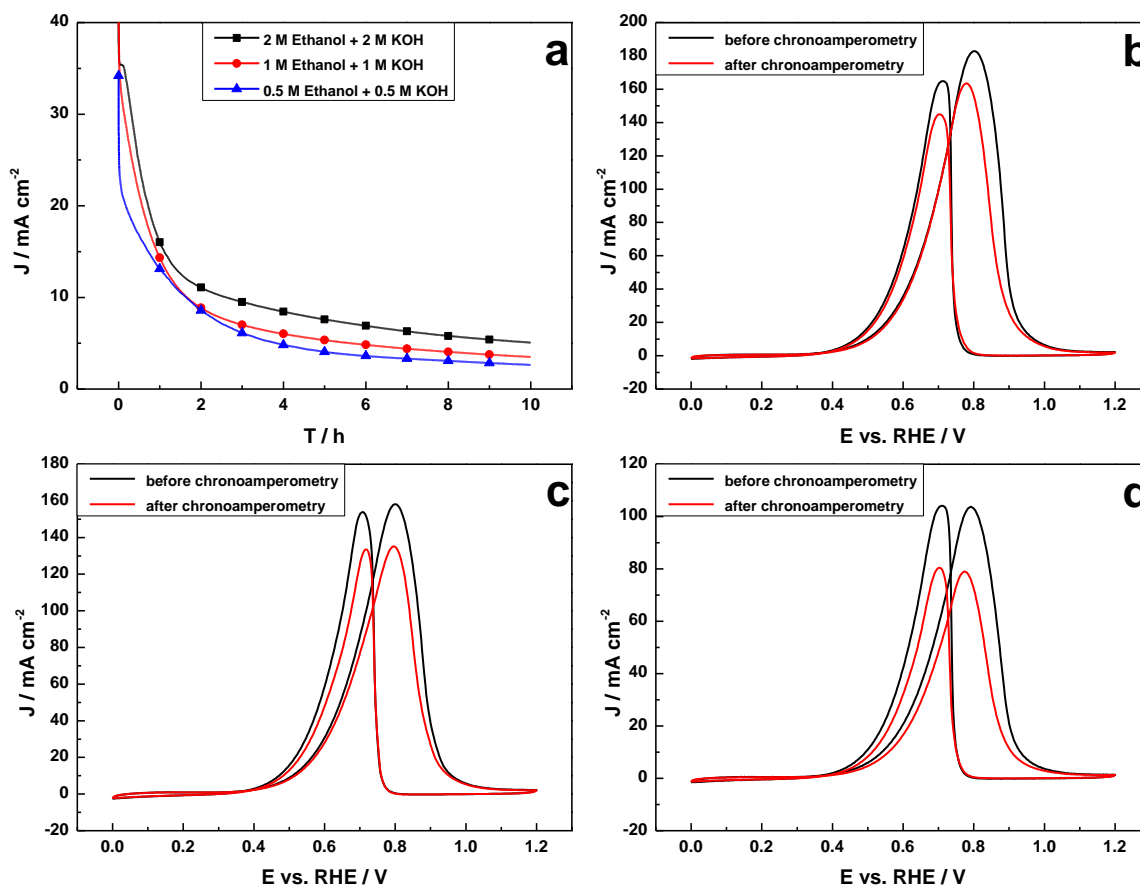

Figure 7-7. (a) Chronoamperometric curves for ethanol electrooxidation at 0.7 V on Pd/C in different electrolyte; (b) Cyclic voltammograms of Pd/C in 2 M Ethanol + 2 M KOH; (c) Cyclic voltammograms of Pd/C in 1 M Ethanol + 1 M KOH; (d) Cyclic voltammograms of Pd/C in 0.5 M Ethanol + 0.5 M KOH.

Table 7-2. Current ratio between after and before chronoamperometry at 0.60 V of the positive-going scan of voltammetry for the electro-oxidation of ethanol in different electrolyte.

Fuel Composition	Current Ratio of after and before chronoamperometry
2 M Ethanol 2 M KOH	94.60%
1 M Ethanol 1 M KOH	91.01%
0.5 M Ethanol 0.5 M KOH	81.05%

Chronopotentiometry, as well as other electrochemical methods, was employed for the investigation of electrode processes at Pd/C surfaces. Fig. 7-8a shows chronopotentiometric measurement of ethanol electro-oxidation at the Pd/C electrode. The figure represents the potential-time profiles obtained by setting the working electrode current at 10 mA/cm^2 in 2 M Ethanol + 2 M KOH electrolyte. The potential increased slowly and arrived at 0.70 V after 3 h resulted in the formation of Pd oxide. The Pd/C electro-catalyst became inactivate totally after 10 h. The comparison of CVs recorded before and after chronopotentiometry at 10 mA/cm^2 for 10 h was shown in Fig. 7-8b. The current density descends markedly. The peak current density dropped from 179.2 to 121.0 mA/cm^2 after chronopotentiometry test which again confirming the role of the anodic stress in the catalyst deactivation.
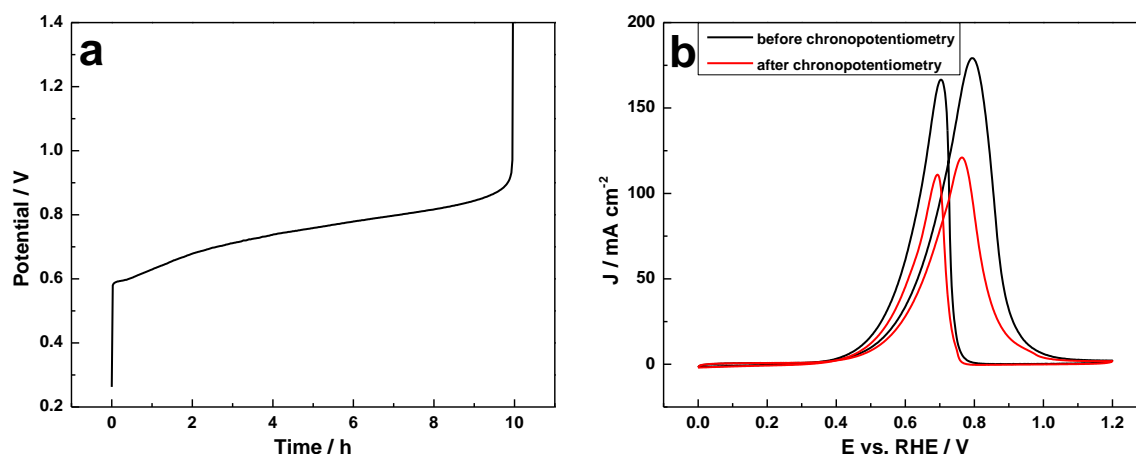
Figure 7-8. (a) Chronopotentiometric curve for ethanol electrooxidation at 10 mA/cm^2 on Pd/C in 2 M Ethanol + 2 M KOH electrolyte; (b) Cyclic voltammograms of Pd/C in 2 M Ethanol + 2 M KOH before and after the chronopotentiometry.

7.2.3 Passive Direct Ethanol Fuel Cell investigation

The role of palladium oxidation was also investigated in passive fuel cell. The recirculation of passive DEFCs was used by replacement of exhausted cells with fresh fuel on the same MEA. The first, second and third polarization curves were just recorded before the first, second and third galvanostatic test separately. Figure 7-9a shows the polarization curves of the passive DEFC containing Pd/C as anode and FePc-CoPc/C as cathode. Power density dramatically decreased for the second and third cycle. The maximum power density is 38.3, 14.9 and 9.9 mW/cm^2 separately for the three cycles. Figure 7-9b shows the galvanostatic curves of the passive DEFC. The anode potential increased with time results in the oxidation of palladium as we can know from Pd/C cyclic voltammetry in KOH electrolyte. At the same time, the arising of anode potential with time is in accordance with the half-cell result shown in Figure 7-8b. The final anode potential is about 0.8 V, which is higher than the onset potential of Pd oxide, at the end of galvanostatic. The lose efficacy of fuel cell by reutilization of the same MEA primarily caused by the oxidation of palladium. As shown in Figure 7-9b, the second and third cycle of constant current curves clearly exhibit a considerably lower cell voltage and higher anode potential compared to the first cycle. The energy density released during the galvanostatic experiments is 82.4, 60.6, 41.4 J/cm^3 separately.
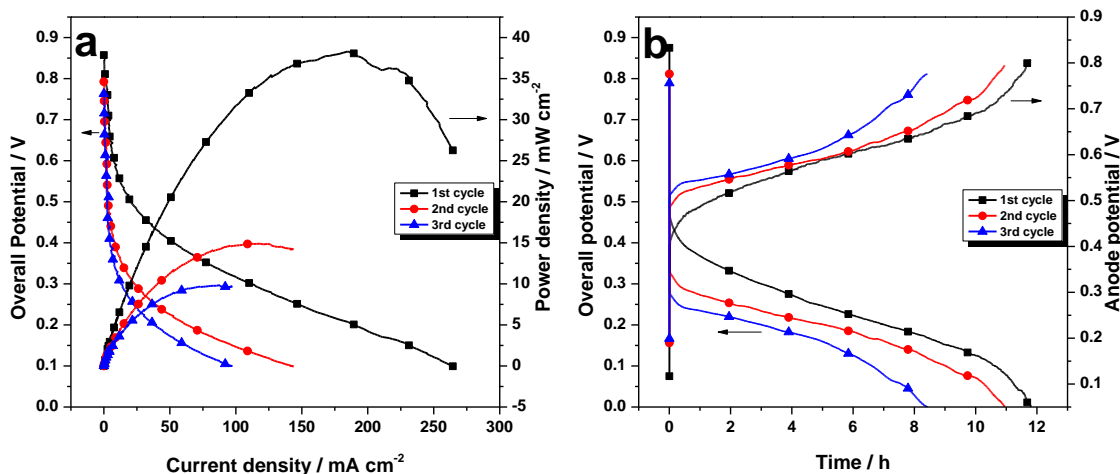
Figure 7-9. (a) The comparison on the performance of three cycles of the passive DEFC containing the Pd/C anode catalyst and fueled with 2 M Ethanol + 2 M KOH. a) Polarization and power density curves and (b) galvanostatic curves with the constant current density of 20 mA/cm^2.

Table 7-3. The performance of the three cycles of passive DEFCs.

Cycle	Open Circuit Voltage (V)	Current Density at 0.4 V (mA/cm^2)	Maximum Power Density (mW/cm^2)	Delivered Energy (J)
1	0.860	53.186	38.306	989.333
2	0.793	9.140	14.912	727.560
3	0.763	4.605	9.858	497.110

7.2.4 X-ray absorption spectroscopy

From the above, we know that Pd oxidation plays a major role in Pd degradation. One of the key points in understanding the phenomena occurring under ongoing chemical reactions is the evaluation of the oxidation state of palladium depending on its physicochemical conditions. As we know, XAS is sensitive to valence and local structures of investigated elements [162-163]. Furthermore, the fixed energy X-ray absorption voltammetry is a novel rapid XAS technique applied to electrochemical systems for the in situ XAS study of electrode materials [62, 164]. The fixed energy should be chosen on the absorption edge in order to give the maximum contrast between different oxidation states. It is known that K-edge XANES could be affected by the local structure as well as the oxidation states of the absorber. As the acquisition of K-edge XANES spectra of standard Pd and PdO samples [165-167], the correct X-ray energy can be chosen. The Pd K-edge in Pd metal shows two peaks characteristic of transition metals. There is a peak valley at about 23470 eV between the two peaks. Moreover, the XANES spectra of PdO have the strong absorption at the Pd K-edge, because the d-p hybridization of Pd^{2+} significantly increases the absorption cross-section, compared with that of Pd foil. Therefore, Pd oxide shows much higher absorption compared to Pd at fixed energy of 24370 eV. In addition, the different local structures for palladium and palladium oxide leads to the fact that a shoulder in the edge threshold (24347 eV) for Pd is not detected for palladium oxide. Based on the above, 24370 and 24347 eV were chosen as the fixed energy to detect the transform of Pd during cyclic voltammetry. Figure 7 displays the FEXRAV spectra for Pd/C recorded in 0.1 M KOH with a scan rate of 5 mV/s. Figure 7a shows the in situ X-ray absorption intensity employed for energy selection at 24370 eV.

At the potential window of -0.6 V ~ 0 V, the absorption of X-ray shows a gently unchanged situation, which means no obvious change of the charge state. From 0 V, the XAS intensity increased gradually caused by the change of charge state toward a higher value, i.e. Pd (II). The increasing in XAS intensity signifies the change amount of Pd (0) to Pd (II) rather than higher charge state value, i.e. Pd (IV). This is because Pd (IV) oxide is formed at potential higher than 1.5 V vs. RHE [74]. The formation of Pd (IV) proceeds until the potential limit of anodic scan. In the cathodic scan, the XAS intensity decreased until -0.35 V (vs. Ag/AgCl) presaging the reduction of Pd (II) to Pd (0). Fig. 7-10b shows the X-ray absorption intensity employed for energy selection at 24347 eV. It shows completely opposite tendency

with Fig. 7-10a. This precisely explains the same phenomena of Pd during electrochemical reaction as the XAS of Pd exhibits a smaller feature at 24370 eV and stronger feature at 24347 eV compared to PdO. At the same time, the result inosculates with the half cell and passive full cell experiments. And not only so, FEXRAV shows the more directly and intuitionistic evidence of the formation of palladium oxidation.
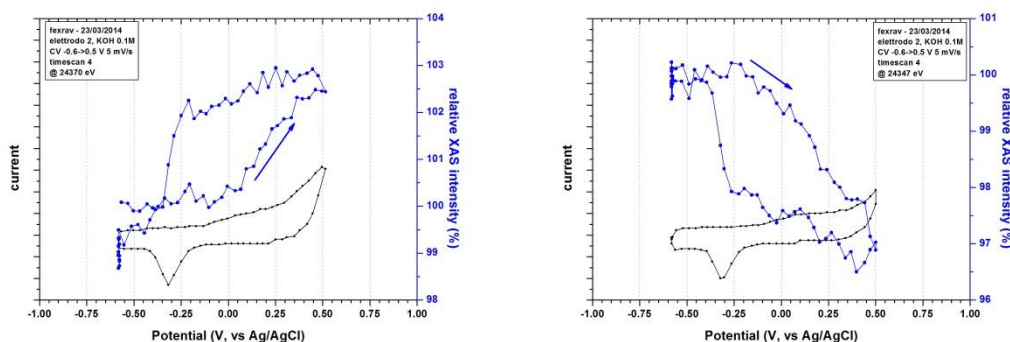

Figure 7-10. FEXRAV spectra and CV of Pd/C recorded in 0.1 M KOH with a scan rate of 5 mV/s employed for fixed energy at (a) 24370 eV and (b) 24347 eV.

In addition to FEXRAV, XAS has also been used to test the evolution before and after DEFCs investigation. In Fig. 7-11, Pd K-edge XANES spectra of standard Pd foil, new Pd/C before DEFC test, exhausted Pd/C after DEFC test and standard PdO powders are presented. The Pd K-edge in Pd foil shows two peaks characteristic of transition metals at lower energy than 24420 eV. However, no splitting of the edge is observed. The second absorption peak is stronger than the first, because the absorption cross-section in the K-edge region of transition metals is strongly influenced by d-s,p hybridization caused by unoccupied d bands [167]. Thus, in the systems where the d-s, p hybridization is strong, the p-like density of states is strongly enhanced and the absorption can be increased like the second absorption peak in the XANES spectrum of the Pd foil. The XANES spectra of PdO in the figure show the strong absorption at the Pd K-edge, because the d-p hybridization of Pd^{2+} significantly increases the absorption cross-section, compared with that of Pd foil. Figure 7-11 shows that the XANES spectra of exhausted Pd/C after DEFC test are distinctly different from new Pd/C before DEFC test. With some subtle differences, exhausted Pd/C after DEFC test is similar to that of PdO.

Meanwhile, new Pd/C before DEFC test is similar to standard Pd foil. This phenomenon strongly proves our hypothesis of Pd oxide formation as the main cause of Pd deactivation.
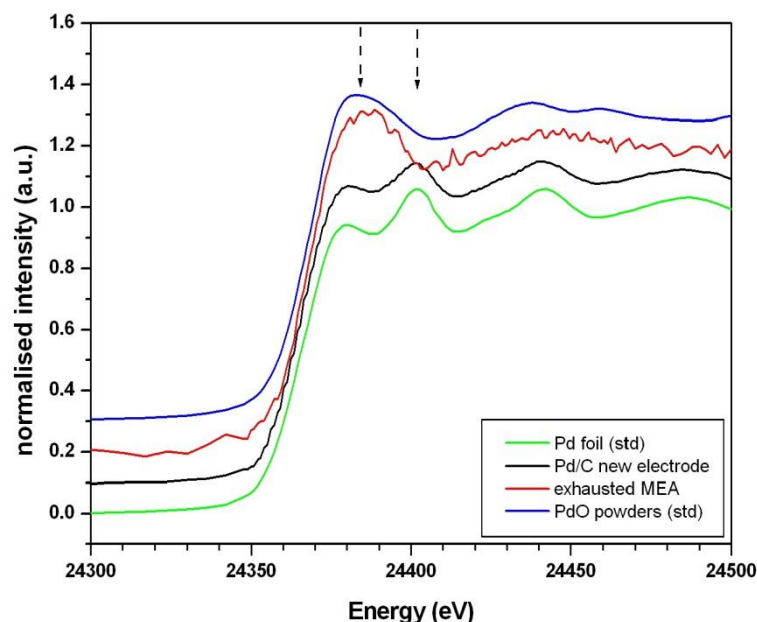

Figure 7-11. Normalized XANES spectra of standard Pd foil, new Pd/C before DEFC test, exhausted Pd/C after DEFC test and standard PdO powders.

7.3 Conclusions

Pd/C has been synthesized and used to investigate the performance of palladium in alkaline electrolyte. Cyclic voltammetry, chronopotentiometry, passive direct ethanol fuel cell test, normalized X-ray absorption near edge structure, and also fixed energy X-ray absorption voltammetry were chosen to investigate the mechanism of palladium degradation.

We have shown that palladium oxidation is the major causes of the deactivation of palladium-based electrocatalysts in alkaline electrolyte. Meanwhile, this deactivation process is significantly affected by the anodic stress. It has been demonstrated by the effect of the upper potential limit in cyclic voltammetry. Cycles with higher upper potential limit show a more pronounced reduction of the electrochemically active surface area as compared to

analogous cycles acquired with lower upper potential limit. Deactivation has been proved to be at least partially irreversible.

The synthesized Pd/C has been used as anode in anion exchange membrane direct ethanol fuel cell. This single cell has run for three cycles with the same membrane electrode assemble and only replacing the electrolyte after each cycle. The power density of the third cycle dropped to less than 30% of the initial one. The record of the anode potential has shown the evidence that palladium electrocatalysts is responsible for most of the cell potential drop observed in the galvanostatic trials.

X-ray absorption spectroscopy has been used to trace the direct evidence of palladium oxidation. On the one hand, fixed energy X-ray voltammetry shows the in-situ palladium oxidation and reduction during cyclic voltammetry. On the other hand, XANES before and after the galvanostatic cycles have shown that the exhausted catalyst is completely oxidized and we suggest that this is the origin of the degradation of electro-catalytic performances.

On the basis of our results we conclude that in order to prolong the life of palladium electrocatalysts in alkaline environment it is necessary to limit the exposition of large anode to over-potentials (e.g. exceeding 0.7 V). This way limits the formation of palladium oxide species which cannot be recovered to fresh metallic Pd in the operating conditions commonly encountered in direct alcohol fuel cells and electrochemical reformers.

8. Direct ethanol fuel cells with promoted temperature and pressure

8.1 Introduction

Palladium based catalysts have been actively explored as the anode in alkaline direct ethanol fuel cells in recent years due to their unique properties and applications towards ethanol oxidation. Details are involved in 1.3.3.

Meanwhile, tungsten carbide (WC) has been proposed as electrocatalyst or elctrocatalyst support, due to its high stability, low electrical resistivity, and strong interaction with other materials. More importantly, WC not only has platinum-like catalytic behavior but also shows good resistance to CO poisoning, these make cheaper WC a promising alternative anodic material for DEFCs.

Above all, ethanol is a sustainable, carbon-neutral transportation fuel source. It is an ideal fuel source for direct oxidation fuel cells for portable and mobile applications because it offers multiple advantages over hydrogen and methanol, including higher energy density and ease of transportation, storage, and handling. However, the power output of the DEFCs must be substantially improved before widespread commercialization is possible. One of the way to get the improvement of the DEFCs is to go high temperature in order to increase the kinetics both of EOR and ORR.

Increasing the operating temperature of DEFCs directly fed with liquid ethanol can effectively increase the ethanol electro-oxidation rate and decrease the over-potential. On the other hand, increasing operation temperature needs new solid electrolytes other than the usual Nafion® membranes [168] that cannot operate at higher temperatures for a long time. Thus, in order to improve the performance of DEFCs based on Nafion® membrane used extensively at present, it is of great importance to hunt for more active anode catalysts for ethanol electro-oxidation at lower temperatures.

8.2 Results and discussion

Table 8-1. The experimental conditions of temperature and pressure.

Temperature (°C)	Pressure (atm)
20	1.0
80	2.0
100	2.6
120	3.4
150	6.0

8.2.1 Pd electrochemical performance at high temperature

Prior to the discussion of Pd electrocatalytic activity of EOR, it is important to test a CV profile of Pd in basic acidic or alkaline solution recorded in the potential range of thermodynamic stability of electrolyte (0-1.20 V).

Figure 8-1 shows a typical CV profile for Pd (poly) electrode in aqueous H_3PO_4 at room temperature (20 °C). It reveals that the Pd electro-oxidation commences at ca. 0.90 V, while the oxide reduction starts at ca. 0.85 V. The CV profile also shows that the H adsorption and absorption commence at ca. 0.30 V. The large amount of H absorption overlaps the adsorption of H making difficulty to distinguish each other. It is interesting to compare the CVs of Pd in basic alkali and acid that we can find both the hydrogen adsorption/absorption and desorption are enhanced in alkali. This can't only be attributed to the higher capacity of ionization capacity in 0.1 M KOH than 0.1 M H_3PO_4, but also to the affect by the anion and cation [169-172]. It is important to notice the difference of surface oxide formation and reduction between two electrolytes. Especially, the corresponding current of reduction of Pd oxide at the range of 0.60 - 0.85 V is much higher in alkali which is due to the high intensity of adsorption of hydroxyl on Pd in alkali proceeding with the high Pd oxide formation and reduction.
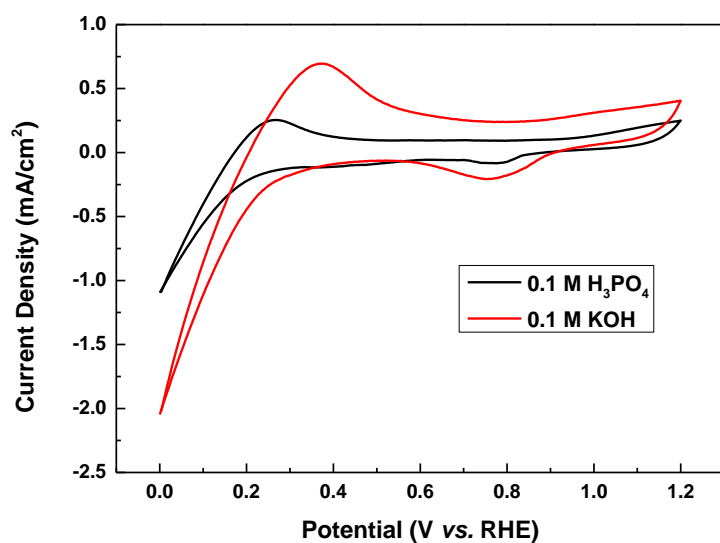
Figure 8-1. Cyclic voltammetry of polycrystalline Pd in 0.1 M H$_3$PO$_4$ and 0.1 M KOH separately at room temperature. Scan rate: 50 mV/s.

Figure 8-2 shows the influence of temperature on the CV profile of Pd both in acid and alkali. As increasing the temperature, the adsorption and absorption of hydrogen occurs earlier and the corresponding current is larger. Increasing the temperature also results in the increase of the amount of the Pd oxide formation and reduction. Peculiarly, the detailed information of the Pd oxide reduction in Figure 8-2 has been shown in Figure 8-3. We observe that an extension of temperature in acid results in an increase of temperature results in: (a) thicker oxide films up until 100 °C and then becoming thinner (greater current density); (b) the displacement of E$_{peak}$ towards less positive potentials. Similar moving of E$_{peak}$ is found in alkali, but the difference is the relation between current density and temperature is almost linear in alkali. This phenomenon may be explained by two aspects: a) increasing the temperature up till 100 °C generates thicker oxide but results in dissolution of Pd when the temperature getting higher than 100 °C in acid. Clearly, two electrode processes occur concurrently, namely Pd oxidation and direct Pd dissolution in acid; but only Pd oxidation occurs in alkali during the whole temperature range. b) on the other hand, a change of t has strong impact on the reduction peak potential, E_{peak}, which consistently shifts towards less-

positive values is due to the more stable formation of Pd oxide. Furthermore, the current of PdO reduction in alkali is higher than acid during the whole temperature range.
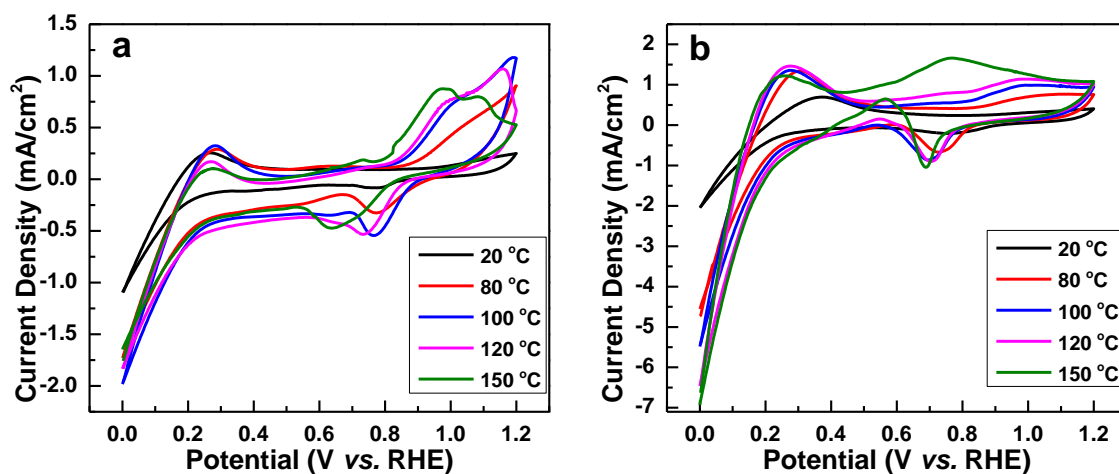

Figure 8-2. Cyclic voltammetry of polycrystalline Pd in a) 0.1 M H_3PO_4; b) 0.1 M KOH at different temperatures. Scan rate: 50 mV/s.
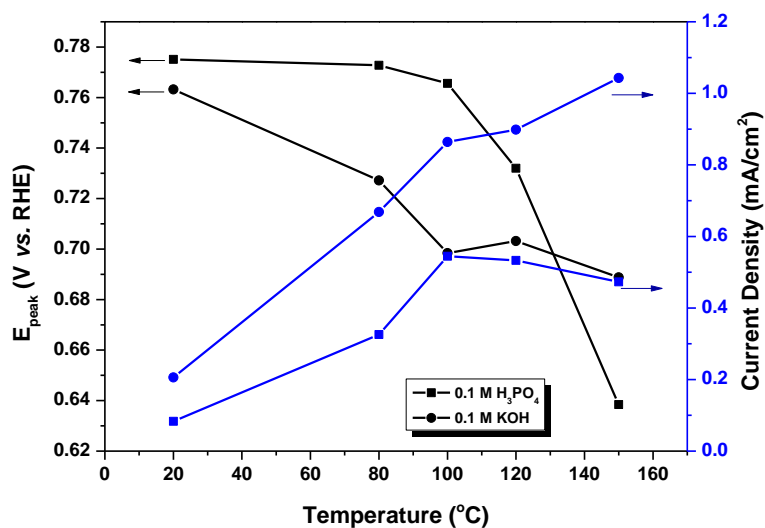

Figure 8-3. The relationship of the peak potential and charge density of Pd oxide reduction with temperature.

The catalytic activity of Pd for EOR has been investigated at promoted temperature in 0.1 M Ethanol with different solutions. The different electrolytes are shown in Table 8-2.

Table 8-2. Electrolyte composition. Ethanol and H_3PO_4/KOH concentrations.

Ethanol	H_3PO_4/KOH
	0.01 M
0.1 M	0.1 M
	1.0 M

Figure 8-4 shows the CV profile of Pd in 0.1 M Ethanol + 0.1 M H_3PO_4. Compared to the electrolyte without ethanol (Fig. 8-2a), we find that the only difference is the larger cathodic current during under potential deposition of hydrogen area which is caused by the adsorption of ethanol on Pd. Decreasing and increasing H_3PO_4 concentration (Fig.8-4a and Fig. 8-4b separately) result in different sorption of hydrogen, ethanol and oxide formation and reduction phenomenon but without any obvious ethanol oxidation current.
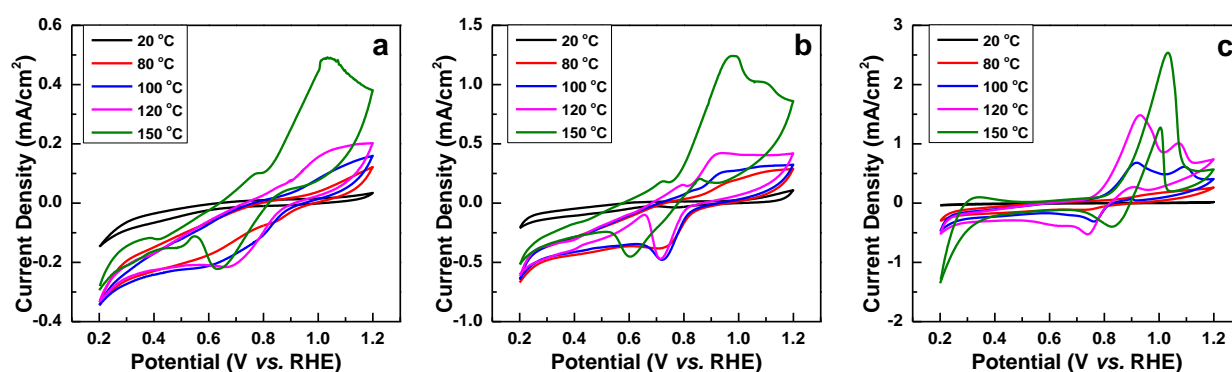

Figure 8-4. Cyclic voltammetry of polycrystalline Pd in a) 0.1 M Ethanol + 0.01 M H_3PO_4; b) 0.1 M Ethanol + 0.1 M H_3PO_4; c) 0.1 M Ethanol + 1 M H_3PO_4. Scan rate: 50 mV/s.

Figure 8-5b shows the CV profile of Pd in 0.1 M Ethanol + 0.1 M KOH. Different from the phenomenon in acid (Fig. 8-4b), Pd shows distinct catalytic activity for EOR. Increasing the temperature results in significant improve of the ethanol oxidation current. In addition, the onset potential of ethanol oxidation is also clearly negative-shifted. Specially, the peak current density is enhanced from 0.89 to 25.76 mA/cm^2 by increasing the temperature from 20 °C to 150 °C the improvement of catalytic activity can be attributed to the high kinetics of Pd absorbing hydroxyl which can be proved by Fig. 8-2b. As we know, the ability of adsorbing OH$^-$ is the crucial factor of Pd towards ethanol oxidation.

Keeping the same condition except lower KOH concentration lead to different catalytic activity. Fig. 8-5a shows the typical character of Pd for EOR at room temperature. But it's impossible to distinguish the ethanol oxidation current as overlapped by the large amount of Pd oxide formation current at higher t. This can be explained by the lack of OH$^-$ hindering the further oxidation of adsorbed ethanol on Pd surface.

On the contrary, keep the same ethanol concentration but increase the KOH concentration leads to the more remarkable improve of EOR (Figure 8-5c).
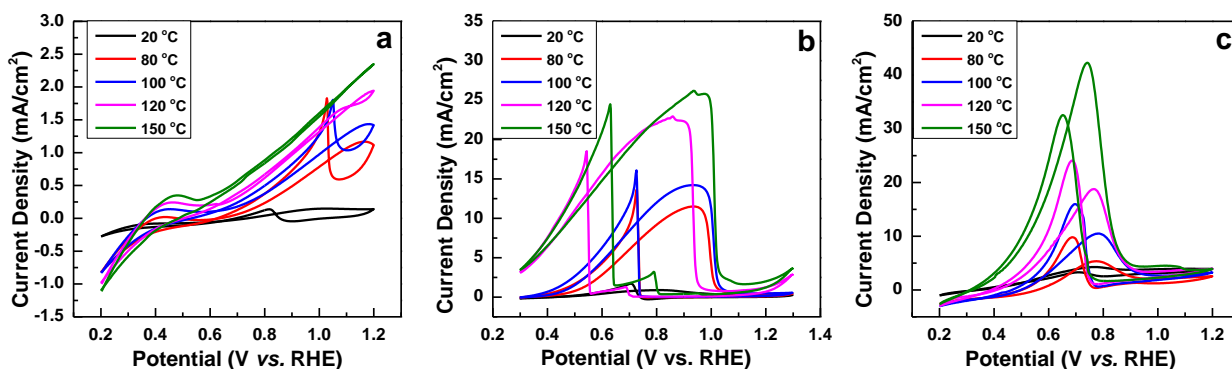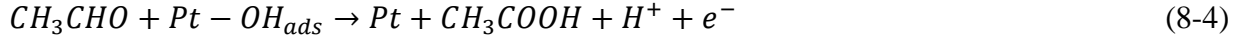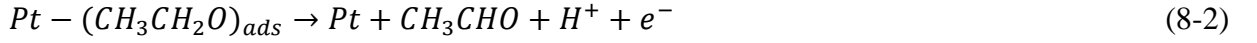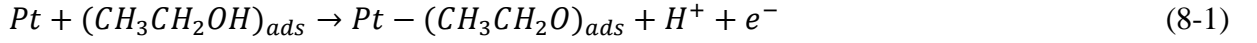

Figure 8-5. Cyclic voltammetry of polycrystalline Pd in a) 0.1 M Ethanol + 0.01 M KOH; b) 0.1 M Ethanol + 0.1 M KOH; c) 0.1 M Ethanol + 1 M KOH. Scan rate: 50 mV/s.

To explain the different performance of Pd in acid and alkali, we should trace back to the ethanol oxidation mechanism on catalyst surface. As we know, for example Pt as following:

$$Pt + (CH_3CH_2OH)_{ads} \rightarrow Pt - (CH_3CH_2O)_{ads} + H^+ + e^- \tag{8-1}$$

$$Pt - (CH_3CH_2O)_{ads} \rightarrow Pt + CH_3CHO + H^+ + e^- \tag{8-2}$$

$$Pt + H_2O \rightarrow Pt - OH_{ads} + H^+ + e^- \tag{8-3}$$

$$CH_3CHO + Pt - OH_{ads} \rightarrow Pt + CH_3COOH + H^+ + e^- \tag{8-4}$$

Due to the lack of the ability of dissociation of H_2O to hydron and hydroxyl as Pt (eq. 8-3), Pd adsorbs hydroxyl directly from the alkaline electrolyte (eq. 8-5).

$$Pd + OH^- \rightarrow Pd - OH_{ads} + e^- \tag{8-5}$$

This makes difficulty to oxidize ethanol in acid. Conversely, the EOR goes on wheels in alkali owe to the good ability of Pd adsorbing ions.

In the end, we can conclude that the amount of OH⁻ in electrolyte is the decisive factor of ethanol oxidation of Pd. Under the ensuring of enough amount of OH⁻, increasing the experimental temperature can enhance the ability of catalyzing EOR dramatically.

8.2.2 WC electrochemical performance at high temperature

8.2.2.1 Structure characterization

The crystal structure of the WC-Co was investigated by XRD technique as shown in Fig. 8-6. The strong diffraction peaks at the Bragg angles of 31.5°, 35.6°, 48.3°, 64.1°, 65.7°, 73.1°, 75.5°, 77.1°, 84.1°, 98.7° correspond to the (001), (100), (101), (110), (002), (111), (200), (102), (201), (112) facets of WC. The sample also exhibits diffraction patterns of 2θ values at 34.7°, 38.2°, 39.8°, 52.4°, 62.3° and 70.0° which can be indexed to (100), (002), (101), (102), (110), (103) facets of W_2C. The cobalt-containing phases (Co_6W_6C, Co_2W_4C) are not present in the X-ray diffraction of WC-Co. A small broad peak around 43° indicates the formation of amorphous Co and cobalt-containing materials.
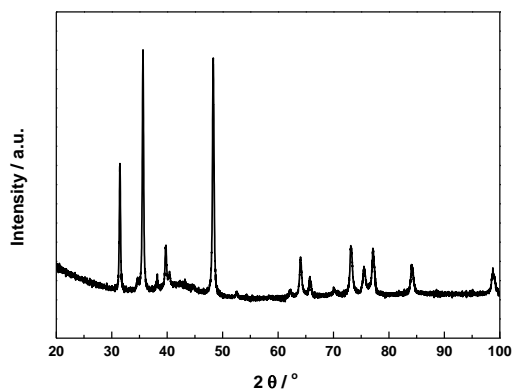
Figure 8-6. X-ray powder diffraction pattern of WC-Co.

8.2.2.2 Electrochemical characterization

Figure 8-7 displays CV curves for WC-Co surface exposed to 1 M H_3PO_4 without and with ethanol. The working electrode was cycled from 0 to 1.20 V and back to 0 V at a linear rate of 50 mV/s. The CV curve of WC shows a cathodic current at potential lower than 0.10 V due to the hydrogen evolution reaction (HER) [173]. Beyond 0.4 V, the onset of a significant oxidation current occurred and persisted to 1.20 V. This oxidation current is attributed to the irreversible oxidation of the WC film into W_xO_y species. As the potential of the WC working electrode was decreased, the curve retraced its path until the onset to a cathodic current at ~0.3 V, again due to the onset of the HER. In comparison, the CV curve of WC-Co in 1 M H_3PO_4 +1 M Ethanol displays much less current of HER and oxidation of WC. This means that the injection of ethanol suppresses the oxidation of WC. No clear ethanol oxidation can be observed.
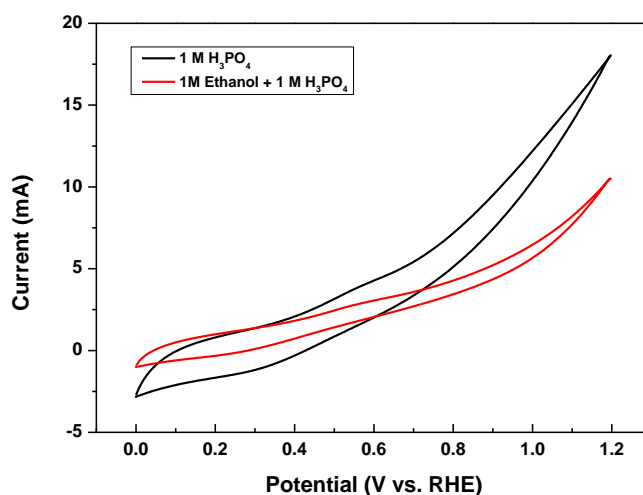
134

Figure 8-7. Cyclic voltammograms of WC-Co in 1 M H₃PO₄ and 1 M Ethanol + 1 M H₃PO₄ at 20 °C. Scan rate: 50 mV/s.

Figure 8-8 shows the CV profile of WC-Co at promoted temperature. As increasing temperature, the onset of surface oxidation moved to negative potential (Fig. 8-8a). In the same time, the oxidation current is increased intensely. It is worth noting that it shows obvious ethanol oxidation current at 50 °C (Fig. 8-8b). The plateau at ∼0.8 V is corresponding to the oxidation of ethanol. Further increasing the potential results in surface oxidation of WC-Co. At the reverse scan, as decreasing potential to ∼0.5 V, ethanol oxidation starts again. Keep increasing the temperature higher than 50 °C results in the tense surface oxidation hindering the catalytic activity of EOR. In addition, surface oxidation has a strong impact on the cyclic voltammetry which lead to prevent the observation of the current of EOR.
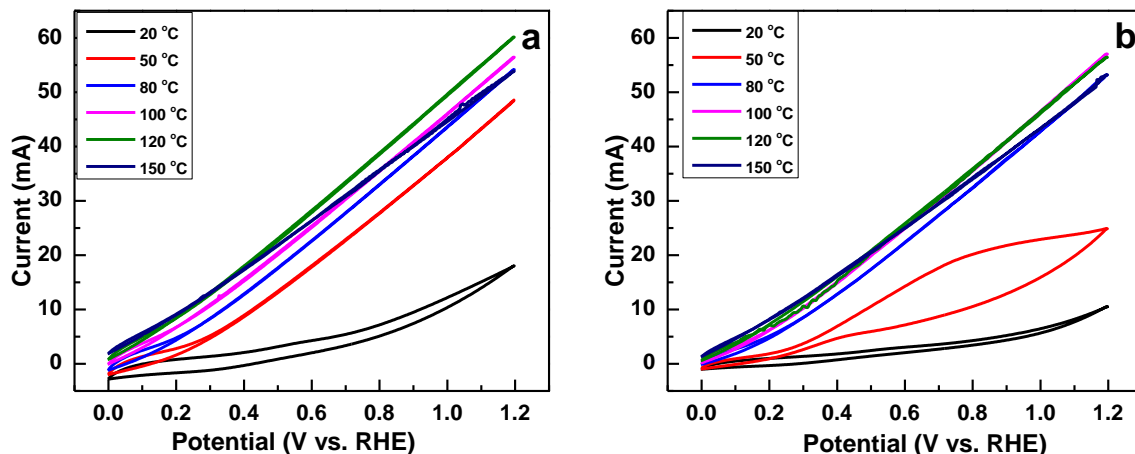
Figure 8-8. Cyclic voltammograms of WC-Co in (a) 1 M H_3PO_4 and (b) 1 M Ethanol + 1 M H_3PO_4 at promoted temperatures. Scan rate: 50 mV/s.

The electrochemical performance of WC-Co was also investigated in alkaline electrolyte. As shown in Fig. 8-9, the surface oxidation starts at ~0.9 V in 0.1 M KOH which is much more positive-going than in 1 M H_3PO_4. A plateau at the potential range of 0.6 - 0.7 V may be relevant with the ethanol oxidation. Linearly increasing the potential results in the surface oxidation. In addition, the surface oxidation current is reduced intensely as comparing the electrolyte with and without ethanol.

Figure 8-10 shows the CV tested at promoted temperature. Increasing the temperature leads to the enhanced hydrogen sorption and WC-Co oxidation. EOR cannot be observed due to the large current of surface oxidation. Specially, the current of WC-Co oxidation is effectively suppressed by adding ethanol during the whole temperature range.
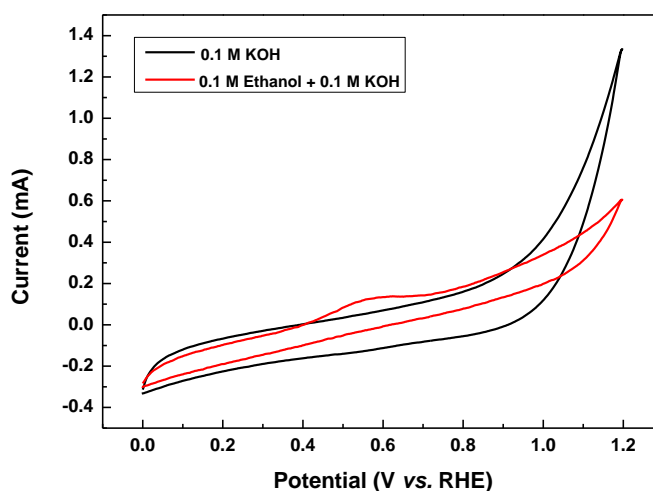
Figure 8-9. Cyclic voltammograms of WC-Co in 0.1 M KOH and 0.1 M Ethanol + 0.1 M KOH at 20 °C. Scan rate: 50 mV/s.
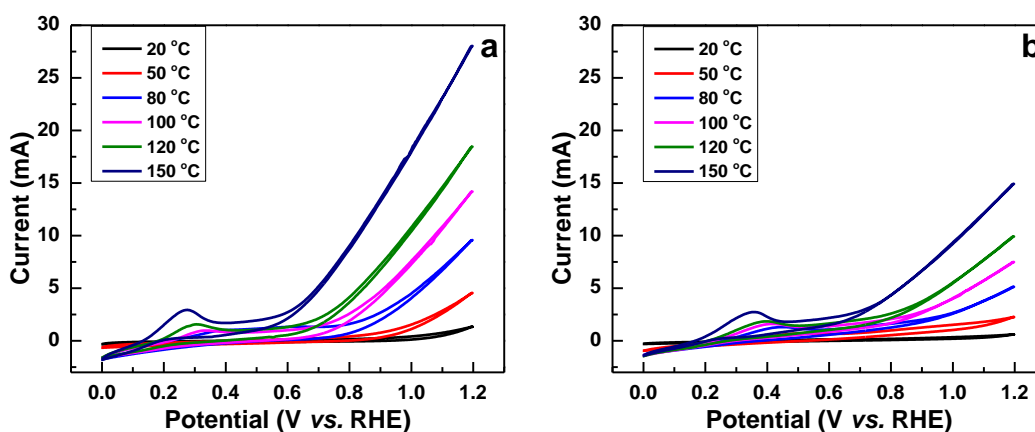

Figure 8-10. Cyclic voltammograms of WC-Co in a) 0.1 M KOH and b) 0.1 M Ethanol + 0.1 M KOH at promoted temperatures. Scan rate: 50 mV/s.

8.3 Conclusions

Both palladium and tungsten carbide have been investigated by cyclic voltammetry in acid and alkali at promoted temperatures.

The adsorption of hydroxyl is crucial to ethanol oxidation reaction on palladium. Due to the lack of the ability of dissociation of H_2O to hydron and hydroxyl, Pd can only adsorb hydroxyl directly from the alkaline electrolyte. This makes Pd difficulty to oxidize ethanol in acid. Conversely, the EOR goes on wheels in alkali owe to the good ability of Pd adsorbing ions. The amount of OH^- in electrolyte is the decisive factor of ethanol oxidation of Pd. Under the ensuring of enough amount of OH^-, increasing the experimental temperature can enhance the ability of catalyzing EOR dramatically.

Tungsten carbide does show catalytic activity of ethanol oxidation reaction. However, this activity is really poor due to the low stability of WC. To increase the catalytic activity and improve the stability of WC, it can be modify by doping with other stable metals such as Pt, Pd.

9. Conclusions and Perspective

This thesis presents the results of an extensive investigation of the electrochemical oxidation of small organic molecules for the application in Direct Liquid Fuel Cells. The main work has been focused on the development of novel platinum-free electrocatalysts and their application as anode materials in complete fuel cells. We have shown that a suitable tailoring of the anode electrocatalysts as well as an appropriate selection of the fuel composition can dramatically improve the performance of the system.

Most of the work has been focused on the electro-oxidation of ethanol. Ethanol is indeed by far the major renewable alcohol being obtained from the fermentation of sugars as well as from the steam reforming of cellulose. We have shown that the energy efficiency of direct ethanol fuel cells can be doubled as compared to state of the art devices by the use of suitable nanostructured palladium catalysts. Ethanol oxidation on palladium can also be promoted by adding oxides (e.g. ceria) resulting in further improvement of the performance. A suitable choice of the fuel composition has also been shown to be crucial. We have found that the concentration of ethanol in the fuel strongly affects the performance and has to be carefully selected in dependence of the application (powering small electronic devices, automotive, etc).

Among the other alcohols we have investigated glycerol and ethylene glycol. Glycerol is the major by-product of biodiesel industry and its exploitation in the concomitant production of energy and chemicals is an intriguing opportunity for increasing the energy efficiency and lowering the environmental impact of biodiesel production. We have shown that glycerol oxidation can also be significantly enhanced by applying appropriate catalysts. The partial oxidation of glycerol in alkaline DLFC has led to the concomitant production of electric power and tartronate, an important raw chemical for industrial applications, including pharmaceutics. The oxidation of ethylene glycol in DLFCs has led to the formation of valuable chemicals such as oxalate, an essential compound for a variety of industrial processes.

We have also explored formate as a fuel in order to get high performance direct liquid fuel cells. Direct formate fuel cells show higher open circuit voltage (≥ 1 V) as compared to

fuel cells fed with alcohols. Furthermore the oxidation kinetics of formate on palladium is faster as compared with ethanol and methanol. For this reason we have obtained AEM-DFFCs with high power density ($\approx$ 100 mW cm^{-2} @ 20 °C) and higher energy efficiency as compared to state-of-the-art AEM-DLFCs with alcohol containing fuels. We have also shown that fuel composition plays a key role in defining the devices performance and the overall energy efficiency.

The fuel cells developed in this study employ palladium based anodes (for the oxidation of alcohols and formate) and FePc-CoPc cathodes (for the oxygen reduction reaction). This is a key point. Indeed the DLFCs reported in the literature rely on the use of platinum at both anode and cathode. This fact results in an extremely high cost that hampers the possibility of a full commercial exploitation. We skip using platinum thanks to the use of an anion exchange membrane, Tokuyama A-201, that is very conductive in alkaline media. Using FePc-CoPc has also implication on the energy efficiency. In fact, FePc-CoPc is inactive toward organic compound oxidation, resulting in negligible potential drops for fuel crossover.

Our experiments have also shown that the performance of palladium based electrocatalysts in direct liquid fuel cells degrade with time. We have investigated such degradation to understand its primary causes. With a combined approach using electrochemical investigations and synchrotron light experiments (X-ray Absorption Spectroscopy) we have demonstrated that palladium oxide formation is the major cause. X-Ray Absorption Near Edge Structure (XANES) spectra of the Pd Kα edge before and after fuel cell runs has shown that Pd is present in its metallic form in the pristine catalyst, while it is almost completely oxidized after work. This study has also shown that to achieve suitable service life in real operation, palladium has to be exposed to anode potential lower than 0.7 V vs. RHE. In practice this can be achieved with the electronics control of the device.

Besides the analysis of the energy performance of complete fuel cells we have undertaken fundamental investigations to seek for novel strategies to improve the activity of the anode materials. To do so we have concentrated on electrochemical methods to alter the surface of metals. We have discovered that the application of a square wave potential (3 min. at 4.55 V RHE followed by 3 min. at -1.95 V and repeated for three cycles) to a polycrystalline palladium foil results in a dramatic roughening of the surface and so in an

increase of the catalytic activity. The catalytic activity enhancement (4 - 5.6 times) was found to be much larger than it would be expected just accounting for the increase of the real surface area (2.5 times). With tailored electrochemical investigations we have shown that the increase of the catalytic activity was also the result of a change in the distribution of the crystal surface termination. Particularly we have observed a net increase in the density of low coordination surface atoms (coordination number < 8). Low coordination sites are well known to be effective in promoting the oxidation of small organic molecules, more effective as compared to sites with higher coordination. We have also found that our square wave potential treatment affects the pathway of ethanol oxidation reaction. Indeed C-C cleavage has been achieved in a larger extent as compared to the untreated surface.

We have extended the same square wave potential treatment to platinum. We have discovered that the square wave period is crucial for the effectiveness of the treatment on platinum. The most active surface for Ethanol Oxidation Reaction (EOR) has been produced with a square wave period of 120 min, while the maximum stability of the catalytic performance has been obtained with the sample produced with a period of 360 min. The treatment has produced roughening and a significant increase in the electrocatalytic activity as compared to the untreated surface, as it was observed for palladium. These findings suggest that square wave potential can be a general technique to enhance performance of noble metals.

In conclusion, the thesis reports the first comprehensive investigation of the energy performance of anion exchange membrane direct liquid fuel cells. Our analysis has shown that the anode electrocatalyst is the major component that determines the direct liquid fuel cells behavior. We have found that the use of tailored nanostructured materials at the anode results in an enormous improvement in the exploitation of the energy content of the fuel. At present the energy efficiency of DLFCs is still not comparable to that of state-of-the-art hydrogen fed Polymer Electrolyte Membrane Fuel Cells (PEMFCs). With the development of suitable square wave treatment and the addition of promoting oxides we have indicated two strategies to drive the energy efficiency and power density of DLFCs toward those of the best performing hydrogen fuelled PEMFCs.

Publications

Publications on scientific journals

1. A. Marchionni, M. Bevilacqua, C. Bianchini, Y. X. Chen, J. Filippi, P. Fornasiero, A. Lavacchi, H. Miller, **L.Q. Wang**, F. Vizza, *Electrooxidation in Alkaline Media of Ethylene Glycol and Glycerol on Pd-(Ni-Zn)/C Anodes in Direct Alcohol Fuel Cells*, ChemSusChem, 6 (2013) 518.

2. **L.Q. Wang**, M. Bevilacqua, Y. X. Chen, J. Filippi, M. Innocenti, A. Lavacchi, A. Marchionni, H. Miller, F. Vizza, *Enhanced electro-oxidation of alcohols at electrochemically treated polycrystalline palladium surface*, J. Power Sources, 242 (2013) 872.

3. M. Bellini, M. Bevilacqua, M. Innocenti, A. Lavacchi, H.A. Miller, J. Fillipi, A. Marchionni, W. Oberhauser, **L.Q. Wang**, F. Vizza, *Energy & chemicals from renewable resources by electrocatalysis*, J. Elcetrochemical Society 161(2014) D3032.

4. Y.X. Chen, A. Lavacchi, H.A. Miller, M. Bevilacqua, J. Filippi, M. Innocenti, A. Marchionni, W. Oberhauser, **L.Q. Wang**, F. Vizza, *Nanotechnology makes biomass electrolysis more energy efficient than water electrolysis*, Nature Communications 5 （2014）DOI: 10.1038/ncomms5036.

5. **L.Q. Wang**, M. Bevilacqua, J. Filippi, P. Fornasiero, M. Innocenti, A. Lavacchi, A. Marchionni, H. A. Miller, F. Vizza, *Electrochemical growth of platinum Nanostructures for enhanced ethanol oxidation*, Applied Catalysis B 165(2015) 185.

6. Y.X. Chen, M. Bellini, M. Bevilacqua, P. Fornasiero, A. Lavacchi, H.A. Miller, **L.Q. Wang**, F. Vizza, *Direct Alcohol Fuel Cells: Toward the Power Densities of Hydrogen-Fed Proton Exchange Membrane Fuel Cells*, ChemSusChem 8 (2015) 524.

7. **L.Q. Wang**, A. Lavacchi, M. Bellini, F. D'Acapito, F. Di Benedetto, M. Innocenti, H.A. Miller, G. Montegrossi, C. Zafferoni, F. Vizza, *Deactivation of Palladium Electrocatalysts for Alcohols Oxidation in Basic Electrolytes*, Electrochimica Acta. DOI: 10.1016/j.electacta.2015.02.026.

8. **L.Q. Wang**, A. Lavacchi, M. Innocenti, P. Fornasiero, M. Bevilacqua, H.A. Miller, J. Filippi, A. Marchionni, F. Vizza, *Energy Performance of Platinum-Free Alkaline Direct Ethanol Fuel Cells*, Submitted to Chemcatchem.

9. **L.Q. Wang**, P. Fornasiero, A. Lavacchi, H.A. Miller, F. Vizza, *Non-platinum Catalysts for Air-breathing Direct Formate Fuel Cells*, Manuscript in preparation.

Publications/abstracts in conferences/congresses

1. S. Cinotti, E. Banchelli, L. Becucci, I. Bencista, M. Innocenti, A. Lavacchi, L. Luconi, **L.Q. Wang**, *Silver electrodeposition from ionic liquids: Coating morphology and mass transport issues*, ECS Transactions, 58 (2013) 43.

2. I. Bencista, F.D. Benedetto, M.L. Foresti, A. Lavacchi, F. Vizza, H.A. Miller, **L.Q. Wang**, M. Innocenti, *Electrodeposition of semiconductor thin films with different composition and band gap*, ECS Transactions, 58 (2013) 23.

Conferences, seminars, advanced courses and other didactic activities

1. Second Joint Summer School on nanotechnology, July 2–5, 2012, Udine, Italy.

2. International Conference on Electrochemical Materials and Technologies for Clean Sustainable Energy, 5-9 July, 2013, Guangzhou, China.

3. XXXII Convegno Interregionale delle Sezioni Toscana Umbria Marche Abruzzo della Società Chimica Italiana, 1-2 July, 2013, Sesto Fiorentino, Italy.

4. "Deactivation of Palladium based catalyst in direct ethanol fuel cell". L.Q. Wang, M. Bellini, M. Bevilacqua, J. Filippi, A. Lavacchi, A. Marchionni, H. Miller, F. Vizza, 65th Annual Meeting of the International Society of Electrochemistry, August 31-September 5, 2014, Lausanne, Switzerland.

Acknowledgements

Needless to say that in the completion of the dissertation, the endless love of my parents is of vital importance.

During those three years, I have taken so many benefits with all those peoples' help. I owe my deep thanks to them all.

References

(1)   "World Energy Intensity: Total Primary Energy Consumption per Dollar of Gross Domestic Product using Purchasing Power Parities, 1980-2004". Energy Information Administration, U.S. Department of Energy. **2006**.

(2)   Chefurka, S. World Energy and Population.

(3)   Shafiee, S.; Topal, E., When will fossil fuel reserves be diminished? *Energ Policy* **2009**, *37* (1), 181-189.

(4)   Barbir, F., Fuel Cell Electrochemistry. In *PEM Fuel cells: Theory and Practice*, Elsevier, 2012.

(5)   Lavacchi, A.; Miller, H.; Vizza, F., *Nanotechnology in Electrocatalysis for Energy*. Springer, 2013.

(6)   Mauritz, K. A.; Moore, R. B., State of understanding of Nafion. *Chem Rev* **2004**, *104* (10), 4535-4585.

(7)   Sammes, N.; Bove, R.; Stahl, K., Phosphoric acid fuel cells: Fundamentals and applications. *Curr Opin Solid St M* **2004**, *8* (5), 372-378.

(8)   Broers, G. H. J.; Ketelaar, J. A. A., High temperature fuel cells. *industrial & engineering chemistry* **1960**, *52*, 303-306.

(9)   Nernst, W., Uber die elektrolytische Leitung fester Korper bei sehr hohen Temperaturen. *Z. Electrochem.* **1899**, *6*, 41-43.

(10) Yamamoto, O., Solid oxide fuel cells: fundamental aspects and prospects. *Electrochim Acta* **2000**, *45* (15-16), 2423-2435.

(11) Doshi, R.; Richards, V. L.; Carter, J. D.; Wang, X. P.; Krumpelt, M., Development of solid-oxide fuel cells that operate at 500 degrees C. *J Electrochem Soc* **1999**, *146* (4), 1273-1278.

(12) The fuel cell industry review 2013.

(13) Hsueh, K. L.; Tsai, L. D.; Lai, C. C., Direct Methanol Fuel Cells. *Electrochemical Technologies for Energy Storage and Conversion* **2012**, *1&2*, 701-727.

(14) Alternative Fuels.

(15) Zhou, W. J.; Li, W. Z.; Song, S. Q.; Zhou, Z. H.; Jiang, L. H.; Sun, G. Q.; Xin, Q.; Poulianitis, K.; Kontou, S.; Tsiakaras, P., Bi- and tri-metallic Pt-based anode catalysts for direct ethanol fuel cells. *J Power Sources* **2004**, *131* (1-2), 217-223.

(16) Zhao, T. S.; Li, Y. S.; Shen, S. Y., Anion-exchange membrane direct ethanol fuel cells: Status and perspective. *Front. Energy Power Eng. China* **2010**, *4*, 443-458.

(17) Wan, Y.; Peppley, B.; Creber, K. A. M.; Bui, V. T.; Halliop, E., Quaternized-chitosan membranes for possible applications in alkaline fuel cells. *J Power Sources* **2008**, *185* (1), 183-187.

(18) Xua, T. W.; Liu, Z. M.; Li, Y.; Yang, W. H., Preparation and characterization of Type II anion exchange membranes from poly(2,6-dimethyl-1,4-phenylene oxide) (PPO). *J Membrane Sci* **2008**, *320* (1-2), 232-239.

(19) Pandey, A. K.; Goswami, A.; Sen, D.; Mazumder, S.; Childs, R. F., Formation and characterization of highly crosslinked anion-exchange membranes. *J Membrane Sci* **2003**, *217* (1-2), 117-130.

(20) Slade, R. C. T.; Varcoe, J. R., Investigations of conductivity in FEP-based radiation-grafted alkaline anion-exchange membranes. *Solid State Ionics* **2005**, *176* (5-6), 585-597.

(21) Varcoe, J. R.; Slade, R. C. T.; Yee, E. L. H.; Poynton, S. D.; Driscoll, D. J.; Apperley, D. C., Poly(ethylene-co-tetrafluoroethylene)-derived radiation-grafted anion-exchange membrane with properties specifically tailored for application in metal-cation-free alkaline polymer electrolyte fuel cells. *Chem Mater* **2007**, *19* (10), 2686-2693.

(22) Xing, B.; Savadogo, O., Hydrogen/oxygen polymer electrolyte membrane fuel cells (PEMFCs) based on alkaline-doped polybenzimidazole (PBI). *Electrochem Commun* **2000,** *2* (10), 697-702.

(23) Leykin, A. Y.; Shkrebko, O. A.; Tarasevich, M. R., Ethanol crossover through alkali-doped polybenzimidazole membrane. *J Membrane Sci* **2009,** *328* (1-2), 86-89.

(24) Colmati, F.; Antolini, E.; Gonzalez, E. R., Effect of temperature on the mechanism of ethanol oxidation on carbon supported Pt, PtRu and Pt3Sn electrocatalysts. *J Power Sources* **2006,** *157* (1), 98-103.

(25) Li, H. Q.; Sun, G. Q.; Cao, L.; Jiang, L. H.; Xin, Q., Comparison of different promotion effect of PtRu/C and PtSn/C electrocatalysts for ethanol electro-oxidation. *Electrochim Acta* **2007,** *52* (24), 6622-6629.

(26) Shen, Q. M.; Min, Q. H.; Shi, J. J.; Jiang, L. P.; Zhang, J. R.; Hou, W. H.; Zhu, J. J., Morphology-Controlled Synthesis of Palladium Nanostructures by Sonoelectrochemical Method and Their Application in Direct Alcohol Oxidation. *J Phys Chem C* **2009,** *113* (4), 1267-1273.

(27) Wang, X. G.; Wang, W. M.; Qi, Z.; Zhao, C. C.; Ji, H.; Zhang, Z. H., High catalytic activity of ultrafine nanoporous palladium for electro-oxidation of methanol, ethanol, and formic acid. *Electrochem Commun* **2009,** *11* (10), 1896-1899.

(28) Ksar, F.; Surendran, G.; Ramos, L.; Keita, B.; Nadjo, L.; Prouzet, E.; Beaunier, P.; Hagege, A.; Audonnet, F.; Remita, H., Palladium Nanowires Synthesized in Hexagonal Mesophases: Application in Ethanol Electrooxidation. *Chem Mater* **2009,** *21* (8), 1612-1617.

(29) Tian, N.; Zhou, Z. Y.; Yu, N. F.; Wang, L. Y.; Sun, S. G., Direct Electrodeposition of Tetrahexahedral Pd Nanocrystals with High-Index Facets and High Catalytic Activity for Ethanol Electrooxidation. *J Am Chem Soc* **2010,** *132* (22), 7580-+.

(30) Liu, H. P.; Ye, J. P.; Xu, C. W.; Jiang, S. P.; Tong, Y. X., Kinetics of ethanol electrooxidation at Pd electrodeposited on Ti. *Electrochem Commun* **2007,** *9* (9), 2334-2339.

(31)Bambagioni, V.; Bianchini, C.; Marchionni, A.; Filippi, J.; Vizza, F.; Teddy, J.; Serp, P.; Zhiani, M., Pd and Pt-Ru anode electrocatalysts supported on multi-walled carbon nanotubes and their use in passive and active direct alcohol fuel cells with an anion-exchange membrane (alcohol = methanol, ethanol, glycerol). *J Power Sources* **2009,** *190* (2), 241-251.

(32) Chen, X. M.; Wu, G. H.; Chen, J. M.; Chen, X.; Xie, Z. X.; Wang, X. R., Synthesis of "Clean" and Well-Dispersive Pd Nanoparticles with Excellent Electrocatalytic Property on Graphene Oxide. *J Am Chem Soc* **2011,** *133* (11), 3693-3695.

(33) Thotiyl, M. M. O.; Kumar, T. R.; Sampath, S., Pd Supported on Titanium Nitride for Efficient Ethanol Oxidation. *J Phys Chem C* **2010,** *114* (41), 17934-17941.

(34)Chen, Y. X.; Lavacchi, A.; Chen, S. P.; di Benedetto, F.; Bevilacqua, M.; Bianchini, C.; Fornasiero, P.; Innocenti, M.; Marelli, M.; Oberhauser, W.; Sun, S. G.; Vizza, F., Electrochemical Milling and Faceting: Size Reduction and Catalytic Activation of Palladium Nanoparticles. *Angew Chem Int Edit* **2012,** *51* (34), 8500-8504.

(35) Lee, Y. W.; Kim, M.; Kim, Y.; Kang, S. W.; Lee, J. H.; Han, S. W., Synthesis and Electrocatalytic Activity of Au-Pd Alloy Nanodendrites for Ethanol Oxidation. *J Phys Chem C* **2010,** *114* (17), 7689-7693.

(36) Cheng, F. L.; Dai, X. C.; Wang, H.; Jiang, S. P.; Zhang, M.; Xu, C. W., Synergistic effect of Pd-Au bimetallic surfaces in Au-covered Pd nanowires studied for ethanol oxidation. *Electrochim Acta* **2010,** *55* (7), 2295-2298.

(37) Nguyen, S. T.; Law, H. M.; Nguyen, H. T.; Kristian, N.; Wang, S. Y.; Chan, S. H.; Wang, X., Enhancement effect of Ag for Pd/C towards the ethanol electro-oxidation in alkaline media. *Appl Catal B-Environ* **2009,** *91* (1-2), 507-515.

(38) Oliveira, M. C.; Rego, R.; Fernandes, L. S.; Tavares, P. B., Evaluation of the catalytic activity of Pd-Ag alloys on ethanol oxidation and oxygen reduction reactions in alkaline medium. *J Power Sources* **2011,** *196* (15), 6092-6098.

(39) Maiyalagan, T.; Scott, K., Performance of carbon nanofiber supported Pd-Ni catalysts for electro-oxidation of ethanol in alkaline medium. *J Power Sources* **2010,** *195* (16), 5246-5251.

(40) Zhang, Z. Y.; Xin, L.; Sun, K.; Li, W. Z., Pd-Ni electrocatalysts for efficient ethanol oxidation reaction in alkaline electrolyte. *Int J Hydrogen Energ* **2011,** *36* (20), 12686-12697.

(41) Shen, P. K.; Xu, C. W., Alcohol oxidation on nanocrystalline oxide Pd/C promoted electrocatalysts. *Electrochem Commun* **2006,** *8* (1), 184-188.

(42) Bambagioni, V.; Bianchini, C.; Chen, Y. X.; Filippi, J.; Fornasiero, P.; Innocenti, M.; Lavacchi, A.; Marchionni, A.; Oberhauser, W.; Vizza, F., Energy Efficiency Enhancement of Ethanol Electrooxidation on Pd-CeO2/C in Passive and Active Polymer Electrolyte-Membrane Fuel Cells. *Chemsuschem* **2012,** *5* (7), 1266-1273.

(43) Hu, F. P.; Ding, F. W.; Song, S. Q.; Shen, P. K., Pd electrocatalyst supported on carbonized TiO2 nanotube for ethanol oxidation. *J Power Sources* **2006,** *163* (1), 415-419.

(44) Chu, D. B.; Wang, J.; Wang, S. X.; Zha, L. W.; He, J. G.; Hou, Y. Y.; Yan, Y. X.; Lin, H. S.; Tian, Z. W., High activity of Pd-In2O3/CNTs electrocatalyst for electro-oxidation of ethanol. *Catal Commun* **2009,** *10* (6), 955-958.

(45) Liang, Z. X.; Zhao, T. S.; Xu, J. B.; Zhu, L. D., Mechanism study of the ethanol oxidation reaction on palladium in alkaline media. *Electrochim Acta* **2009,** *54* (8), 2203-2208.

(46) Cui, G. F.; Song, S. Q.; Shen, P. K.; Kowal, A.; Bianchini, C., First-Principles Considerations on Catalytic Activity of Pd toward Ethanol Oxidation. *J Phys Chem C* **2009,** *113* (35), 15639-15642.

(47) Fang, X.; Wang, L. Q.; Shen, P. K.; Cui, G. F.; Bianchini, C., An in situ Fourier transform infrared spectroelectrochemical study on ethanol electrooxidation on Pd in alkaline solution. *J Power Sources* **2010,** *195* (5), 1375-1378.

(48) Zhou, Z. Y.; Wang, Q. A.; Lin, J. L.; Tian, N.; Sun, S. G., In situ FTIR spectroscopic studies of electrooxidation of ethanol on Pd electrode in alkaline media. *Electrochim Acta* **2010,** *55* (27), 7995-7999.

(49) Blizanac, B. B.; Ross, P. N.; Markovic, N. M., Oxygen electroreduction on Ag(111): The pH effect. *Electrochim Acta* **2007,** *52* (6), 2264-2271.

(50) Guo, J. S.; Hsu, A.; Chu, D.; Chen, R. R., Improving Oxygen Reduction Reaction Activities on Carbon-Supported Ag Nanoparticles in Alkaline Solutions. *J Phys Chem C* **2010,** *114* (10), 4324-4330.

(51) Yang, D. S.; Bhattacharjya, D.; Inamdar, S.; Park, J.; Yu, J. S., Phosphorus-Doped Ordered Mesoporous Carbons with Different Lengths as Efficient Metal-Free Electrocatalysts for Oxygen Reduction Reaction in Alkaline Media. *J Am Chem Soc* **2012,** *134* (39), 16127-16130.

(52) Liang, Y. Y.; Li, Y. G.; Wang, H. L.; Zhou, J. G.; Wang, J.; Regier, T.; Dai, H. J., Co3O4 nanocrystals on graphene as a synergistic catalyst for oxygen reduction reaction. *Nat Mater* **2011,** *10* (10), 780-786.

(53) Nagaiah, T. C.; Kundu, S.; Bron, M.; Muhler, M.; Schuhmann, W., Nitrogen-doped carbon nanotubes as a cathode catalyst for the oxygen reduction reaction in alkaline medium. *Electrochem Commun* **2010,** *12* (3), 338-341.

(54) Chen, R. R.; Li, H. X.; Chu, D.; Wang, G. F., Unraveling Oxygen Reduction Reaction Mechanisms on Carbon-Supported Fe-Phthalocyanine and Co-Phthalocyanine Catalysts in Alkaline Solutions. *J Phys Chem C* **2009,** *113* (48), 20689-20697.

(55) Olson, T. S.; Pylypenko, S.; Atanassov, P.; Asazawa, K.; Yamada, K.; Tanaka, H., Anion-Exchange Membrane Fuel Cells: Dual-Site Mechanism of Oxygen Reduction Reaction in Alkaline Media on Cobalt-Polypyrrole Electrocatalysts. *J Phys Chem C* **2010,** *114* (11), 5049-5059.

(56) Randin, J. P., Interpretation of the relative electrochemical activity of various metal phthalocyanines for the oxygen reduction reaction. *Electrochim Acta* **1974,** *19* (2), 83-85.

(57) Fujiwara, N.; Siroma, Z.; Yamazaki, S. I.; Ioroi, T.; Senoh, H.; Yasuda, K., Direct ethanol fuel cells using an anion exchange membrane. *J Power Sources* **2008,** *185* (2), 621-626.

(58) Bianchini, C.; Bambagioni, V.; Filippi, J.; Marchionni, A.; Vizza, F.; Bert, P.; Tampucci, A., Selective oxidation of ethanol to acetic acid in highly efficient polymer electrolyte membrane-direct ethanol fuel cells. *Electrochem Commun* **2009,** *11* (5), 1077-1080.

(59) Modestov, A. D.; Tarasevich, M. R.; Leykin, A. Y.; Filimonov, V. Y., MEA for alkaline direct ethanol fuel cell with alkali doped PBI membrane and non-platinum electrodes. *J Power Sources* **2009,** *188* (2), 502-506.

(60) d'Acapito, F.; Trapananti, A.; Torrengo, S.; Mobilio, S., X-Ray Absorption Spectroscopy: The Italian Beamline Gilda at the ESRF. *Notiziario Neutroni e Luce di Sincrotrone* **2014,** *19*, 14-23.

(61) Ashley, K.; Pons, S., Infrared Spectroelectrochemistry. *Chem Rev* **1988,** *88*, 673-695.

(62) Minguzzi, A.; Lugaresi, O.; Locatelli, C.; Rondinini, S.; D'Acapito, F.; Achilli, E.; Ghigna, P., Fixed Energy X-ray Absorption Voltammetry. *Anal Chem* **2013,** *85* (15), 7009-7013.

(63) Chu, D. R.; Jiang, R. Z., Effect of operating conditions on energy efficiency for a small passive direct methanol fuel cell. *Electrochim Acta* **2006,** *51* (26), 5829-5835.

(64) Liu, J. G.; Zhao, T. S.; Chen, R.; Wong, C. W., The effect of methanol concentration on the performance of a passive DMFC. *Electrochem Commun* **2005,** *7* (3), 288-294.

(65) Hammerschlag, R., Ethanol's energy return on investment: A survey of the literature 1990 - Present. *Environ Sci Technol* **2006,** *40* (6), 1744-1750.

(66) Global Ethanol Supply to Exceed 100 Mln Tonnes in 2018, According to Topical Report by Merchant Research & Consulting.

(67) Srinivasan, S.; Velev, O. A.; Parthasarathy, A.; Manko, D. J.; Appleby, A. J., High-Energy Efficiency and High-Power Density Proton-Exchange Membrane Fuel-Cells - Electrode-Kinetics and Mass-Transport. *J Power Sources* **1991,** *36* (3), 299-320.

(68) Bezerra, C. W. B.; Zhang, L.; Lee, K. C.; Liu, H. S.; Marques, A. L. B.; Marques, E. P.; Wang, H. J.; Zhang, J. J., A review of Fe-N/C and Co-N/C catalysts for the oxygen reduction reaction. *Electrochim Acta* **2008,** *53* (15), 4937-4951.

(69) Bambagioni, V.; Bianchini, C.; Filippi, J.; Lavacchi, A.; Oberhauser, W.; Marchionni, A.; Moneti, S.; Vizza, F.; Psaro, R.; Dal Santo, V.; Gallo, A.; Recchia, S.; Sordelli, L., Single-site and nanosized Fe-Co electrocatalysts for oxygen reduction: Synthesis, characterization and catalytic performance. *J Power Sources* **2011,** *196* (5), 2519-2529.

(70) Lamy, C.; Lima, A.; LeRhun, V.; Delime, F.; Coutanceau, C.; Leger, J. M., Recent advances in the development of direct alcohol fuel cells (DAFC). *J Power Sources* **2002,** *105* (2), 283-296.

(71) Barragan, V. M.; Heinzel, A., Estimation of the membrane methanol diffusion coefficient from open circuit voltage measurements in a direct methanol fuel cell. *J Power Sources* **2002,** *104* (1), 66-72.

(72) Vigier, F.; Coutanceau, C.; Perrard, A.; Belgsir, E. M.; Lamy, C., Development of anode catalysts for a direct ethanol fuel cell. *J Appl Electrochem* **2004,** *34* (4), 439-446.

(73) Bianchini, C.; Shen, P. K., Palladium-Based Electrocatalysts for Alcohol Oxidation in Half Cells and in Direct Alcohol Fuel Cells. *Chem Rev* **2009,** *109* (9), 4183-4206.

(74) Grden, M.; Lukaszewski, M.; Jerkiewicz, G.; Czerwinski, A., Electrochemical behaviour of palladium electrode: Oxidation, electrodissolution and ionic adsorption. *Electrochim Acta* **2008,** *53* (26), 7583-7598.

(75) Rhee, Y. W.; Ha, S. Y.; Masel, R. I., Crossover of formic acid through Nafion((R)) membranes. *J Power Sources* **2003,** *117* (1-2), 35-38.

(76) Jeong, K. J.; Miesse, C. A.; Choi, J. H.; Lee, J.; Han, J.; Yoon, S. P.; Nam, S. W.; Lim, T. H.; Lee, T. G., Fuel crossover in direct formic acid fuel cells. *J Power Sources* **2007,** *168* (1), 119-125.

(77) Miesse, C. M.; Jung, W. S.; Jeong, K. J.; Lee, J. K.; Lee, J.; Han, J.; Yoon, S. P.; Nam, S. W.; Lim, T. H.; Hong, S. A., Direct formic acid fuel cell portable power system for the operation of a laptop computer. *J Power Sources* **2006,** *162* (1), 532-540.

(78) Liu, C. T.; Chen, M.; Du, C. Y.; Zhang, J.; Yin, G. P.; Shi, P. F.; Sun, Y. R., Durability of Ordered Mesoporous Carbon Supported Pt Particles as Catalysts for Direct Formic Acid Fuel Cells. *Int J Electrochem Sc* **2012,** *7* (11), 10592-10606.

(79) Rice, C.; Ha, S.; Masel, R. I.; Wieckowski, A., Catalysts for direct formic acid fuel cells. *J Power Sources* **2003,** *115* (2), 229-235.

(80) Wei, J.; Wang, D. T.; Ling, M., Anodic Catalysts for Direct Formic Acid Fuel Cells. *Rare Metal Mat Eng* **2010,** *39* (2), 292-295.

(81) Liu, Z. L.; Hong, L.; Tham, M. P.; Lim, T. H.; Jiang, H. X., Nanostructured Pt/C and Pd/C catalysts for direct formic acid fuel cells. *J Power Sources* **2006,** *161* (2), 831-835.

(82) Bambagioni, V.; Bianchini, C.; Filippi, J.; OberhauserIal, W.; Marchionni, A.; Vizza, F.; Psaro, R.; Sordelli, L.; Foresti, M. L.; Innocenti, M., Ethanol Oxidation on Electrocatalysts Obtained by Spontaneous Deposition of Palladium onto Nickel-Zinc Materials. *Chemsuschem* **2009,** *2* (1), 99-112.

(83) Bartrom, A. M.; Haan, J. L., The direct formate fuel cell with an alkaline anion exchange membrane. *J Power Sources* **2012,** *214*, 68-74.

(84) Mayrhofer, K. J. J.; Strmcnik, D.; Blizanac, B. B.; Stamenkovic, V.; Arenz, M.; Markovic, N. M., Measurement of oxygen reduction activities via the rotating disc electrode method: From Pt model surfaces to carbon-supported high surface area catalysts. *Electrochim Acta* **2008,** *53* (7), 3181-3188.

(85) Gong, K. P.; Du, F.; Xia, Z. H.; Durstock, M.; Dai, L. M., Nitrogen-Doped Carbon Nanotube Arrays with High Electrocatalytic Activity for Oxygen Reduction. *Science* **2009,** *323* (5915), 760-764.

(86) Chen, Z.; Higgins, D.; Chen, Z. W., Nitrogen doped carbon nanotubes and their impact on the oxygen reduction reaction in fuel cells. *Carbon* **2010,** *48* (11), 3057-3065.

(87) Liu, J. G.; Zhao, T. S.; Liang, Z. X.; Chen, R., Effect of membrane thickness on the performance and efficiency of passive direct methanol fuel cells. *J Power Sources* **2006,** *153* (1), 61-67.

(88) Somorjai, G. A., Active Sites for Hydrocarbon Catalysis on Metal Surfaces. *Pure & Appl. Chem.* **1978,** *50*, 963-969.

(89) Quan, Z. W.; Wang, Y. X.; Fang, J. Y., High-Index Faceted Noble Metal Nanocrystals. *Accounts Chem Res* **2013,** *46* (2), 191-202.

(90) Yu, Y.; Zhang, Q. B.; Liu, B.; Lee, J. Y., Synthesis of Nanocrystals with Variable High-Index Pd Facets through the Controlled Heteroepitaxial Growth of Trisoctahedral Au Templates. *J Am Chem Soc* **2010,** *132* (51), 18258-18265.

(91) Tian, N.; Zhou, Z. Y.; Sun, S. G., Platinum Metal Catalysts of High-Index Surfaces: From Single-Crystal Planes to Electrochemically Shape-Controlled Nanoparticles. *J Phys Chem C* **2008,** *112* (50), 19801-19817.

(92) Liu, Z.; Yang, Z. L.; Cui, L.; Ren, B.; Tian, Z. Q., Electrochemically roughened palladium electrodes for surface-enhanced Raman spectroscopy: Methodology, mechanism, and application. *J Phys Chem C* **2007,** *111* (4), 1770-1775.

(93)Marchionni, A.; Bevilacqua, M.; Bianchini, C.; Chen, Y. X.; Filippi, J.; Fornasiero, P.; Lavacchi, A.; Miller, H.; Wang, L. Q.; Vizza, F., Electrooxidation of Ethylene Glycol and Glycerol on Pd-(Ni-Zn)/C Anodes in Direct Alcohol Fuel Cells. *Chemsuschem* **2013,** *6* (3), 518-528.

(94) Cabaniss, S. E.; McVey, I. F., Aqueous infrared carboxylate absorbances: Aliphatic monocarboxylates. *Spectrochim Acta A* **1995,** *51* (13), 2385-2395.

(95) Strathmann, T. J.; Myneni, S. C. B., Speciation of aqueous Ni(II)-carboxylate and Ni(II)-fulvic acid solutions: Combined ATR-FTIR and XAFS analysis. *Geochim Cosmochim Ac* **2004,** *68* (17), 3441-3458.

(96) Cabaniss, S. E.; Leenheer, J. A.; McVey, I. F., Aqueous infrared carboxylate absorbances: aliphatic di-acids. *Spectrochim Acta A* **1998,** *54* (3), 449-458.

(97) Falase, A.; Main, M.; Garcia, K.; Serov, A.; Lau, C.; Atanassov, P., Electrooxidation of ethylene glycol and glycerol by platinum-based binary and ternary nano-structured catalysts. *Electrochim Acta* **2012,** *66*, 295-301.

151

(98) Falase, A.; Garcia, K.; Lau, C.; Atanassov, P., Electrochemical and in situ IR characterization of PtRu catalysts for complete oxidation of ethylene glycol and glycerol. *Electrochem Commun* **2011,** *13* (12), 1488-1491.

(99) Wang, L. Q.; Meng, H.; Shen, P. K.; Bianchini, C.; Vizza, F.; Wei, Z. D., In situ FTIR spectroelectrochemical study on the mechanism of ethylene glycol electrocatalytic oxidation at a Pd electrode. *Phys Chem Chem Phys* **2011,** *13* (7), 2667-2673.

(100) Simoes, M.; Baranton, S.; Coutanceau, C., Electro-oxidation of glycerol at Pd based nano-catalysts for an application in alkaline fuel cells for chemicals and energy cogeneration. *Appl Catal B-Environ* **2010,** *93* (3-4), 354-362.

(101) Markovic, N. M.; Schmidt, T. J.; Stamenkovic, V.; Ross, P. N., Oxygen Reduction Reaction on Pt and Pt Bimetallic Surfaces: A Selective Review. *Fuel Cells* **2001,** *1* (2), 105-116.

(102) Mayrhofer, K. J. J.; Arenz, M.; Blizanac, B. B.; Stamenkovic, V.; Ross, P. N.; Markovic, N. M., CO surface electrochemistry on Pt-nanoparticles: A selective review. *Electrochim Acta* **2005,** *50* (25-26), 5144-5154.

(103) Yoo, E.; Okata, T.; Akita, T.; Kohyama, M.; Nakamura, J.; Honma, I., Enhanced Electrocatalytic Activity of Pt Subnanoclusters on Graphene Nanosheet Surface. *Nano Lett* **2009,** *9* (6), 2255-2259.

(104) Li, Y. J.; Li, Y. J.; Zhu, E. B.; McLouth, T.; Chiu, C. Y.; Huang, X. Q.; Huang, Y., Stabilization of High-Performance Oxygen Reduction Reaction Pt Electrocatalyst Supported on Reduced Graphene Oxide/Carbon Black Composite. *J Am Chem Soc* **2012,** *134* (30), 12326-12329.

(105) Brouzgou, A.; Song, S. Q.; Tsiakaras, P., Low and non-platinum electrocatalysts for PEMFCs: Current status, challenges and prospects. *Appl Catal B-Environ* **2012,** *127*, 371-388.

(106) Tian, N.; Zhou, Z. Y.; Sun, S. G.; Ding, Y.; Wang, Z. L., Synthesis of tetrahexahedral platinum nanocrystals with high-index facets and high electro-oxidation activity. *Science* **2007,** *316* (5825), 732-735.

(107) Zhou, W. J.; Zhou, Z. H.; Song, S. Q.; Li, W. Z.; Sun, G. Q.; Tsiakaras, P.; Xin, Q., Pt based anode catalysts for direct ethanol fuel cells. *Appl Catal B-Environ* **2003,** *46* (2), 273-285.

(108) Tripkovic, A. V.; Popovic, K. D.; Grgur, B. N.; Blizanac, B.; Ross, P. N.; Markovic, N. M., Methanol electrooxidation on supported Pt and PtRu catalysts in acid and alkaline solutions. *Electrochim Acta* **2002,** *47* (22-23), 3707-3714.

(109) Rousseau, S.; Coutanceau, C.; Lamy, C.; Leger, J. M., Direct ethanol fuel cell (DEFC): Electrical performances and reaction products distribution under operating conditions with different platinum-based anodes. *J Power Sources* **2006,** *158* (1), 18-24.

(110) Zhou, W. J.; Song, S. Q.; Li, W. Z.; Zhou, Z. H.; Sun, G. Q.; Xin, Q.; Douvartzides, S.; Tsiakaras, P., Direct ethanol fuel cells based on PtSn anodes: the effect of Sn content on the fuel cell performance. *J Power Sources* **2005,** *140* (1), 50-58.

(111) Jiang, L. H.; Sun, G. Q.; Sun, S. G.; Liu, J. G.; Tang, S. H.; Li, H. Q.; Zhou, B.; Xin, Q., Structure and chemical composition of supported Pt-Sn electrocatalysts for ethanol oxidation. *Electrochim Acta* **2005,** *50* (27), 5384-5389.

(112) Han, K.; Lee, J.; Kim, H., Preparation and characterization of high metal content Pt-Ru alloy catalysts on various carbon blacks for DMFCs. *Electrochim Acta* **2006,** *52* (4), 1697-1702.

(113) Baschuk, J. J.; Li, X. G., Carbon monoxide poisoning of proton exchange membrane fuel cells. *Int J Energ Res* **2001,** *25* (8), 695-713.

(114) Li, Q. F.; He, R. H.; Gao, J. A.; Jensen, J. O.; Bjerrum, N. J., The CO poisoning effect in PEMFCs operational at temperatures up to 200 degrees C. *J Electrochem Soc* **2003,** *150* (12), A1599-A1605.

(115) Bardi, U.; Borri, C.; Lavacchi, A.; Tolstogouzov, A.; Trunin, E. B.; Trunina, O. E., Purification of liquid indium by electric current-induced impurity migration in a static transverse magnetic field. *Scripta Mater* **2009,** *60* (6), 423-426.

(116)   Graedel, T. E., On the Future Availability of the Energy Metals. *Annu Rev Mater Res* **2011,** *41*, 323-335.

(117)   Spendelow, J. S.; Papageorgopoulos, D. C., Progress in PEMFC MEA Component R&D at the DOE Fuel Cell Technologies Program. *Fuel Cells* **2011,** *11* (6), 775-786.

(118)   van der Vliet, D. F.; Wang, C.; Tripkovic, D.; Strmcnik, D.; Zhang, X. F.; Debe, M. K.; Atanasoski, R. T.; Markovic, N. M.; Stamenkovic, V. R., Mesostructured thin films as electrocatalysts with tunable composition and surface morphology. *Nat Mater* **2012,** *11* (12), 1051-1058.

(119)   Gasteiger, H. A.; Markovic, N.; Ross, P. N.; Cairns, E. J., Co Electrooxidation on Well-Characterized Pt-Ru Alloys. *J Phys Chem-Us* **1994,** *98* (2), 617-625.

(120)   Gasteiger, H. A.; Markovic, N. M.; Ross, P. N., H-2 and Co Electrooxidation on Well-Characterized Pt, Ru, and Pt-Ru .2. Rotating Disk Electrode Studies of Co/H-2 Mixtures at 62-Degrees-C. *J Phys Chem-Us* **1995,** *99* (45), 16757-16767.

(121)   Markovic, N. M.; Gasteiger, H. A.; Ross, P. N.; Jiang, X. D.; Villegas, I.; Weaver, M. J., Electrooxidation Mechanisms of Methanol and Formic-Acid on Pt-Ru Alloy Surfaces. *Electrochim Acta* **1995,** *40* (1), 91-98.

(122)   Yajima, T.; Uchida, H.; Watanabe, M., In-situ ATR-FTIR spectroscopic study of electro-oxidation of methanol and adsorbed CO at Pt-Ru alloy. *J Phys Chem B* **2004,** *108* (8), 2654-2659.

(123)   Koper, M. T. M.; Shubina, T. E.; van Santen, R. A., Periodic density functional study of CO and OH adsorption on Pt-Ru alloy surfaces: Implications for CO tolerant fuel cell catalysts. *J Phys Chem B* **2002,** *106* (3), 686-692.

(124)   Tong, Y. Y.; Kim, H. S.; Babu, P. K.; Waszczuk, P.; Wieckowski, A.; Oldfield, E., An NMR investigation of CO tolerance in a Pt/Ru fuel cell catalyst. *J Am Chem Soc* **2002,** *124* (3), 468-473.

(125)   Brankovic, S. R.; Wang, J. X.; Adzic, R. R., Pt submonolayers on Ru nanoparticles - A novel low Pt loading, high CO tolerance fuel cell electrocatalyst. *Electrochem Solid St* **2001,** *4* (12), A217-A220.

(126)   Mann, J.; Yao, N.; Bocarsly, A. B., Characterization and analysis of new catalysts for a direct ethanol fuel cell. *Langmuir* **2006,** *22* (25), 10432-10436.

(127)   Lai, S. C. S.; Koper, M. T. M., Electro-oxidation of ethanol and acetaldehyde on platinum single-crystal electrodes. *Faraday Discussions* **2008,** *140*, 399-416.

(128)   Tarnowski, D. J.; Korzeniewski, C., Effects of surface step density on the electrochemical oxidation of ethanol to acetic acid. *Journal of Physical Chemistry B* **1997,** *101* (2), 253-258.

(129)   Colmati, F.; Tremiliosi-Filho, G.; Gonzalez, E. R.; Berná, A.; Herrero, E.; Feliu, J. M., Surface structure effects on the electrochemical oxidation of ethanol on platinum single crystal electrodes. *Faraday Discussions* **2008,** *140*, 379-397.

(130)   Kowal, A.; Li, M.; Shao, M.; Sasaki, K.; Vukmirovic, M. B.; Zhang, J.; Marinkovic, N. S.; Liu, P.; Frenkel, A. I.; Adzic, R. R., Ternary Pt/Rh/SnO2 electrocatalysts for oxidizing ethanol to CO2. *Nat Mater* **2009,** *8* (4), 325-330.

(131)   Wang, L. Q.; Bevilacqua, M.; Chen, Y. X.; Filippi, J.; Innocenti, M.; Lavacchi, A.; Marchionni, A.; Miller, H.; Vizza, F., Enhanced electro-oxidation of alcohols at electrochemically treated polycrystalline palladium surface. *J Power Sources* **2013,** *242*, 872-876.

(132)   Changes in the electrochemical response of noble metals produced by square-wave potential perturbations. *J Electroanal Chem* **1983,** *146*, 93-108.

(133)   Chen, Y. J.; Sun, S. G.; Chen, S. P.; Li, J. T.; Gong, H., Anomalous IR properties of nanostructured films created by square wave potential on an array of pt microelectrodes: An in situ microscope FTIRS study of CO adsorption. *Langmuir* **2004,** *20* (23), 9920-9925.

(134)   Zhou, Z. Y.; Huang, Z. Z.; Chen, D. J.; Wang, Q.; Tian, N.; Sun, S. G., High-Index Faceted Platinum Nanocrystals Supported on Carbon Black as Highly Efficient Catalysts for Ethanol Electrooxidation. *Angew Chem Int Edit* **2010,** *49* (2), 411-414.

(135)   Conway, B. E., Electrochemical Oxide Film Formation at Noble-Metals as a Surface-Chemical Process. *Prog Surf Sci* **1995,** *49* (4), 331-452.

(136)   Wang, X. P.; Kumar, R.; Myers, D. J., Effect of voltage on platinum dissolution relevance to polymer electrolyte fuel cells. *Electrochem Solid St* **2006,** *9* (5), A225-A227.

(137)   Chen, D.; Tao, Q.; Liao, L. W.; Liu, S. X.; Chen, Y. X.; Ye, S., Determining the Active Surface Area for Various Platinum Electrodes. *Electrocatalysis* **2011,** *2* (3), 207-219.

(138)   Furuya, N.; Koide, S., Hydrogen Adsorption on Platinum Single-crystal Surfaces. *Surface Science* **1989,** *220*, 18-28.

(139)   Markovic, N. M.; Grgur, B. N.; Ross, P. N., Temperature-dependent hydrogen electrochemistry on platinum low-index single-crystal surfaces in acid solutions. *J Phys Chem B* **1997,** *101* (27), 5405-5413.

(140)   Coutanceau, C.; Urchaga, P.; Brimaud, S.; Baranton, S., Colloidal Syntheses of Shape- and Size-Controlled Pt Nanoparticles for Electrocatalysis. *Electrocatalysis* **2012,** *3* (2), 75-87.

(141)   Solla-Gullon, J.; Vidal-Iglesias, F. J.; Herrero, E.; Feliu, J. M.; Aldaz, A., CO monolayer oxidation on semi-spherical and preferentially oriented (100) and (111) platinum nanoparticles. *Electrochem Commun* **2006,** *8* (1), 189-194.

(142)   Clavilier, J.; Armand, D.; Sun, S. G.; Petit, M., Electrochemical Adsorption Behaviour of Platinum Stepped Surfaces in Sulphuric Acid Solutions *J. Electroanal. Chem.* **1986,** *205*, 267-277.

(143)   Triaca, W. E.; Arvia, A. J., The Electrochemical Faceting of Metal-Surfaces - Preferred Crystallographic Orientation and Roughening Effects in Electrocatalysis. *J Appl Electrochem* **1990,** *20* (3), 347-356.

(144)   Lai, S. C. S.; Koper, M. T. M., Ethanol electro-oxidation on platinum in alkaline media. *Phys Chem Chem Phys* **2009,** *11* (44), 10446-10456.

(145)   Xu, C. W.; Shen, P. K.; Liu, Y. L., Ethanol electrooxidation on Pt/C and Pd/C catalysts promoted with oxide. *J Power Sources* **2007,** *164* (2), 527-531.

(146)   Xu, C. W.; Cheng, L. Q.; Shen, P. K.; Liu, Y. L., Methanol and ethanol electrooxidation on Pt and Pd supported on carbon microspheres in alkaline media. *Electrochem Commun* **2007,** *9* (5), 997-1001.

(147)   Xu, J. B.; Zhao, T. S.; Shen, S. Y.; Li, Y. S., Stabilization of the palladium electrocatalyst with alloyed gold for ethanol oxidation. *Int J Hydrogen Energ* **2010,** *35* (13), 6490-6500.

(148)   Shen, S. Y.; Zhao, T. S.; Wu, Q. X., Product analysis of the ethanol oxidation reaction on palladium-based catalysts in an anion-exchange membrane fuel cell environment. *Int J Hydrogen Energ* **2012,** *37* (1), 575-582.

(149)   Hu, G. Z.; Nitze, F.; Barzegar, H. R.; Sharifi, T.; Mikolajczuk, A.; Tai, C. W.; Borodzinski, A.; Wagberg, T., Palladium nanocrystals supported on helical carbon nanofibers for highly efficient electro-oxidation of formic acid, methanol and ethanol in alkaline electrolytes. *J Power Sources* **2012,** *209*, 236-242.

(150)   Verjulio, R. W.; Alcaide, F.; Alvarez, G.; Sabate, N.; Torres-Herrero, N.; Esquivel, J. P.; Santander, J., A micro alkaline direct ethanol fuel cell with platinum-free catalysts. *J Micromech Microeng* **2013,** *23* (11).

(151)   Morozan, A.; Jousselme, B.; Palacin, S., Low-platinum and platinum-free catalysts for the oxygen reduction reaction at fuel cell cathodes. *Energ Environ Sci* **2011,** *4* (4), 1238-1254.

(152)   Chen, Y. X.; Lavacchi, A.; Miller, H. A.; Bevilacqua, M.; Filippi, J.; Innocenti, M.; Marchionni, A.; Oberhauser, W.; Wang, L.; Vizza, F., Nanotechnology makes biomass electrolysis more energy efficient than water electrolysis. *Nat Commun* **2014,** *5*.

(153)   Bambagioni, V.; Bevilacqua, M.; Bianchini, C.; Filippi, J.; Lavacchi, A.; Marchionni, A.; Vizza, F.; Shen, P. K., Self-Sustainable Production of Hydrogen, Chemicals, and Energy from Renewable Alcohols by Electrocatalysis. *Chemsuschem* **2010,** *3* (7), 851-855.

(154)   Albers, P.; Pietsch, J.; Parker, S. F., Poisoning and deactivation of palladium catalysts. *J Mol Catal a-Chem* **2001,** *173* (1-2), 275-286.

(155)   Wang, L.; Bambagioni, V.; Bevilacqua, M.; Bianchini, C.; Filippi, J.; Lavacchi, A.; Marchionni, A.; Vizza, F.; Fang, X.; Shen, P. K., Sodium borohydride as an additive to enhance the performance of direct ethanol fuel cells. *J Power Sources* **2010,** *195* (24), 8036-8043.

(156)   Hu, C. C.; Wen, T. C., Voltammetric Investigation of Palladium Oxides .1. Their Formation Reduction in Naoh. *Electrochim Acta* **1995,** *40* (4), 495-503.

(157)   Kim, K. S.; Gossmann, A. F.; Winograd, N., X-ray photoelectron spectroscopic studies of palladium oxides and the palladium-oxygen electrode. *Anal Chem* **1974,** *46*, 197-200.

(158)   Tang, J.; Petri, M.; Kibler, L. A.; Kolb, D. M., Pd deposition onto Au(111) electrodes from sulphuric acid solution. *Electrochim Acta* **2005,** *51* (1), 125-132.

(159)   Manzanares, M. I.; Pavese, A. G.; Solis, V. M., Comparative Investigation of Formic-Acid and Formaldehyde Electrooxidation on Palladium in Acidic Medium - Effect of Surface Oxides. *J Electroanal Chem* **1991,** *310* (1-2), 159-167.

(160)   Holade, Y.; Morais, C.; Napporn, T. W.; Servat, K.; Kokoh, K. B., Electrochemical Behavior of Organics Oxidation on Palladium-Based Nanocatalysts Synthesized from Bromide Anion Exchange. *ECS Transactions* **2014,** *58* (46), 25-35.

(161)   Grunwaldt, J. D.; Caravati, M.; Ramin, M.; Baiker, A., Probing active sites during palladium-catalyzed alcohol oxidation in "supercritical" carbon dioxide. *Catal Lett* **2003,** *90* (3-4), 221-229.

(162)   Yano, J.; Yachandra, V. K., X-ray absorption spectroscopy. *Photosynth Res* **2009,** *102* (2-3), 241-254.

(163)   Savin, S. L. P.; Berko, A.; Blacklocks, A. N.; Edwards, W.; Chadwick, A. V., The applications of X-ray absorption spectroscopy in the study of nanocrystalline materials and electrochemical systems. *Cr Chim* **2008,** *11* (9), 948-963.

(164)   Minguzzi, A.; Lugaresi, O.; Achilli, E.; Locatelli, C.; Vertova, A.; Ghigna, P.; Rondinini, S., observing the oxidation state turnover in heterogeneous iridium-based water oxidation catalysts. *Chem Sci* **2014,** *5*, 3591-3597.

(165)   Nishihata, Y.; Mizuki, J.; Akao, T.; Tanaka, H.; Uenishi, M.; Kimura, M.; Okamoto, T.; Hamada, N., Self-regeneration of a Pd-perovskite catalyst for automotive emissions control. *Nature* **2002,** *418* (6894), 164-167.

(166)   Chen, C. H.; Hwang, B. J.; Wang, G. R.; Sarma, L. S.; Tang, M. T.; Liu, D. G.; Lee, J. F., Nucleation and growth mechanism of Pd/Pt bimetallic clusters in sodium bis(2-ethylhexyl)sulfosuceinate (AOT) reverse micelles as studied by in situ X-ray absorption spectroscopy. *J Phys Chem B* **2005,** *109* (46), 21566-21575.

(167)   Priolkar, K. R.; Bera, P.; Sarode, P. R.; Hegde, M. S.; Emura, S.; Kumashiro, R.; Lalla, N. P., Formation of Ce1-xPdxO2-delta solid solution in combustion-synthesized Pd/CeO2 catalyst: XRD, XPS, and EXAFS investigation. *Chem Mater* **2002,** *14* (5), 2120-2128.

(168)   Yang, C.; Srinivasan, S.; Arico, A. S.; Creti, P.; Baglio, V.; Antonucci, V., Composition Nafion/zirconium phosphate membranes for direct methanol fuel cell operation at high temperature. *Electrochem Solid St* **2001,** *4* (4), A31-A34.

(169)   Martin, M. H.; Lasia, A., Study of the hydrogen absorption in Pd in alkaline solution. *Electrochim Acta* **2008,** *53* (22), 6317-6322.

(170)   Czerwinski, A.; Marassi, R., The Absorption of Hydrogen and Deuterium in Thin Palladium Electrodes .3. Basic Solutions. *J Electroanal Chem* **1992,** *322* (1-2), 373-381.

(171)   Czerwinski, A.; Marassi, R.; Zamponi, S., The Absorption of Hydrogen and Deuterium in Thin Palladium Electrodes .1. Acidic Solutions. *J Electroanal Chem* **1991,** *316* (1-2), 211-221.

(172)   Czerwinski, A.; Maruszczak, G.; Zelazowska, M.; Lancucka, M.; Marassi, R.; Zamponi, S., The Absorption of Hydrogen and Deuterium in Thin Palladium Electrodes .3. The Influence of Solution Composition. *J Electroanal Chem* **1995,** *386* (1-2), 207-211.

(173)   Weigert, E. C.; Esposito, D. V.; Chen, J. G. G., Cyclic voltammetry and X-ray photoelectron spectroscopy studies of electrochemical stability of clean and Pt-modified tungsten and molybdenum carbide (WC and Mo2C) electrocatalysts. *J Power Sources* **2009,** *193* (2), 501-506.